Title
Transmembrane Transport in Biomimetic Assemblies of One-Dimensional Nanomaterials

Author
Kim, Kyunghoon

Publication Date
2013

Peer reviewed|Thesis/dissertation

Transmembrane Transport in Biomimetic Assemblies of One-Dimensional Nanomaterials

by

Kyunghoon Kim

A dissertation submitted in partial satisfaction of the
requirements for the degree of
Doctor of Philosophy
in
Engineering – Mechanical Engineering
in the
Graduate Division
of the
University of California, Berkeley

Committee in charge:

Professor Costas P. Grigoropoulos, Chair
Professor Liwei Lin
Professor Seung-Wuk Lee
Dr. Aleksandr Noy

Fall 2013

Transmembrane Transport in Biomimetic Assemblies of
One-Dimensional Nanomaterials

By

Kyunghoon Kim

Abstract

Transmembrane Transport in Biomimetic Assemblies of

One-Dimensional Nanomaterials

by

Kyunghoon Kim

Doctor of Philosophy in Engineering - Mechanical Engineering

University of California, Berkeley

Professor Costas P. Grigoropoulos, Chair

The creation of biomimetic structures based on one-dimensional nanomaterials and lipid membranes will provide a unique platform for achieving functionalities of biological machines and mimicking nature at the nanoscale. Silicon nanowires (SiNW) and carbon nanotubes (CNT) are of significant interest due to the novel properties not present in bulk materials as well as characteristic dimensions comparable to the size of biological molecules. My thesis describes the creation of fabricated nanomaterials integrated with biomaterials such lipid membranes and their constitutive proteins to create biomimetic assemblies.

In the first part of my dissertation, I report transmembrane carbon nanotube pores as a biological ion channel analogs. Biological ion channels in nature transport ions across cellular membranes showing two functions of gating and ion selectivity. CNT pores give structural and functional mimic of an ion channel, in part because smooth, narrow and hydrophobic inner pores of the CNT are remarkably similar to natural biological pores. First, CNTs served as a materials platform that can replicate the features of biological channels. I successfully created ultrashort CNTs (ca. ~10nm) using lipid-assisted sonication-cutting method. Lipid molecules self-assemble on the long CNTs to form a template for sonication cutting. These short CNT pores with their length comparable to the lipid membrane thickness provide a much closer match to protein-channel dimensions. Short CNT pores were incorporated into lipid vesicles to mimic membrane ion channels and study transport properties through CNT pores. These short CNTs in a lipid membrane can transport water, protons, and small ions and reject large uncharged species. Ion rejection in CNT channels is determined by charge repulsion at the CNT rim. Electrophoretic ion transport measurements for individual CNT pores revealed an ion conductance value of 0.63ns which is comparable to those of biological channels. CNT pores inserted in the membrane exhibited stochastic gating behavior common for biological ion channels. These fluctuations result from a spontaneous reversible ionic penetration-exclusion transition previously reported in nanofluidic

transport of sub-2-nm pores. Electrophoretically-driven translocation of individual single-stranded DNA molecules through CNT pores produced well-defined ion current blockades. Overall, short CNT mimics transport properties of a biological protein channel. Since the structure and functionality of short CNT pores self-inserted in a lipid membrane resemble the β-barrel structure of a porin, they are termed as "*carbon nanotube porins"*.

In the second part, I describe synthesis of SiNWs grown via vapor-liquid-solid (VLS) mechanism. Silicon nanowires were grown on silicon substrates via chemical vapor deposition (CVD) using silane as a precursor gas and diborane for p-type doing of wires. These nanowires were utilized for a bioelectronics platform for integration of membrane protein functionality based on one-dimensional lipid bilayer. This lipid bilayer provides shielding the nanowires from the solution species and environment for proteins preserving their functionality, integrity, and even vectorality. Here, I report a hybrid lipid bilayer- silicon nanowire bioelectronic device with output controlled via light-induced proton pump protein, bacteriorhodopsin (bR). SiNW field effect transistors (FET) were fabricated via conventional micro/nanofabrication process. bR proteins were incorporated into SiNW transistors covered with a lipid bilayer shell and different ionophore molecules, valinomycin and nigericin were co-assembled to create biologically-tunable bioelectronics devices. In this way, the devices convert photoactivated proton transport by bR protein into an electronic signal. The addition of ionophores tuned the device output by altering membrane ion permeability and the two ionophores were able to modulate different system parameters.

To my lovely parents, sister and brother

ACKNOWLEDGEMENT

I would like to deeply express my sincere gratitude to many people through the five years of my doctoral studies. This doctoral dissertation would not have been completed without the encouragement and great support that I have received from all of them.

Foremost I especially wish to thank my parents Sang Soo Kim and Won Ja Kim for their continued love, support and unwavering belief in me. I owe a lot to my parents, sister and brother who encouraged me at every stage of my academic life. Without you, I would not be where I am today. Thank you for your always being supportive of me.

First of all, I would like to express my deepest gratitude to my advisor, Costas P. Grigoropoulos in the Department of Mechanical Engineering at University of California, Berkeley. I received his consistent guidance, insightful comments and encouragement during the entire period of my graduate study and provided me with an excellent atmosphere for doing research.

I would also like to thank my co-advisor Dr. Aleksandr Noy, a senior research scientist at Lawrence Livermore National Laboratory (LLNL) who has worked closely with me these past couple of years on my research. I would also like to extend my appreciation to Dr. Caroline Ajo-Franklin for her dedication as my supervisor at the Molecular Foundry, Lawrence Berkeley National Laboratory (LBNL). Aleksandr and Caroline let me experience the world of nano- and biomaterials guiding me in my all projects. Their expertise allowed me to stand on a strong foundation.

I would like to express my deepest appreciation to my doctoral committee members, Prof. Van P. Carey, Prof. Liwei Lin and Prof. Samuel S. Mao in the Department of Mechanical Engineering, and Prof. Seung-Wuk Lee in the Department of Bioengineering at UC Berkeley. I would never have been able to finish my dissertation without the guidance and encouragement of my committee members.

I would also like to acknowledge The Molecular Foundry, Materials Sciences Division, LBNL and Biology and Biotechnology Division, Physical and Life Sciences Directorate, Lawrence Livermore National Laboratory for allowing me to use the facilities for my research and for supporting me by sharing skills and expertise on nanoscale materials research. I carried out most of my graduate research there and no research is possible without the access to these two labs.

I would like to give my special thanks to lab directors of The Molecular Foundry, LBNL who provide great opportunities and environments for my research, Dr. Stefano Carbrini in Nanofabrication Facility, Dr. Ron Zuckermann in Biological Nanostructures Facility, Jim Schuck in Imaging&Manipulation of Nanostrucures Facility, and Dr. Jeff Urban in Inorganic Nanostructures Facility.

I take this time to express my sincere appreciation to the staff scientists and engineering associates in LLNL and LBNL, Dr. Morris Wang, Dr. Frances Allen, Dr. Luis R. Comolli, Virginia Altoe, Erin Wood, Alyssa Brand and Dr. Christophe Peroz for their help and guidance.

It is my pleasure to acknowledge my colleagues and friends. Particular thanks to Sang-Gil Ryu, Daeho Lee, Jung Bin In, Eunpa Kim, Andy Cheng Zheng, Jae-Hyuck Yoo, Sangmo Koo, Hyuk-Jun Kwon and Dong-Woo Paeng, who helped me in Laser Thermal Lab at UC Berkeley. Huge thanks to LLNL lab members, Dr. Jia Geng, Dr. Kang Rae

Cho, Dr. Jianfei Zhang, Dr. Mangesh Bangar and Ramya Tunuguntla for their help and support but mostly for their sense of humor in LLNL and LBNL.

Finally, a special thanks to KSME friends who started on and travelled this PhD journey alongside me, Dr. Daeyoung Kong, Dr. Daeho Lee, Dr. Jun Suk Rho, Dr. Young Hwan Chang and Dr. Sanghoon Ahn for their enormous help, practical advice, support and optimism.

TABLE OF CONTENTS

LIST OF FIGURES

LIST OF TABLES

NOMENCLATURE

AFM:	atomic force microscopy
ATP:	adenosine triphosphate
α-HL:	α-haemolysin
bR:	bacteriorhodopsin
BOE:	buffered oxide etchant
C_i:	concentration in the inner compartment,
C_0:	initial concentration
c_i:	concentration of co-ions in the solution
c_i^m:	concentration of co-ions in membrane phase
c_x^m:	membrane charge concentration
ccm:	cubic centimeter per minute
CNT:	carbon nanotube
CVD:	chemical vapor deposition
Cryo-TEM:	cryogenic transmission electron microscopy
D_s:	effective osmolyte diffusion coefficient
DI:	deionized
DLS:	dynamic light scattering
DNA:	deoxyribonucleic acid
DOPC:	1, 2-dioleoyl-sn-Glycero-3-phosphocholine
FEG:	field emission gun
FET:	field-effect transistor
FE-SEM:	field emission scanning electron microscopy
FIB:	focused ion beamfluore
FRAP:	Fluorescence recovery after photobleaching
G:	conductance
GramA:	gramicidin A
HMDS:	hexamethyldisilazane
HPTS:	8-hydroxypyrene-1,3,6-trisulfonic acid trisodium salt
HEPES:	4-(2-hydroxyethyl)-1-piperazineethanesulfonic acid
HRTEM:	high resolution transmission electron microscopy
I-V:	current-voltage
$I_{S\text{-}D}$:	source-drain current
IPA:	isopropyl alcohol
LED:	light emitting diode
LOR:	lift-off resist
k_w:	water permeability
M:	molecular weight (g/mol)
PDMS:	polydimethylsiloxane
PECVD:	plasma enhanced chemical vapor deposition
PLL:	poly-L-lysine
R:	rejection coefficient
RBM:	radial breathing mode
RTA:	rapid thermal annealing
S:	siemens (unit of electric conductance)

S/D:	source/drain
SEC:	size exclusion chromatography
SiNW:	silicon nanowire
SPIP:	scanning probe image processor
ssDNA:	single-stranded DNA
SWNT:	single-walled carbon nanotube
TEM:	transmission electron microscopy
TR-DHPE:	TexasRed-DHPE (N-(Texas Red sulfonyl)-1,2-dihexadecanoyl-snglycero-3-phosphoethanolamine, triethylammonium salt)
TGA:	thermal gravimetric analysis
V_0:	initial volume
V_G:	gate voltage
V_S:	source voltage
VLS:	vapor-liquid-solid
VIS-NIR:	visible-near infrared
z_i:	valence of co-ion
z_j:	valence of counterion
$\Delta\pi_{osm}$:	difference in osmotic pressure
1D:	one-dimensional

Chapter 1 Introduction

1.1 Background

Biological systems control the transport of ions or small molecules across the biological membranes to maintain ionic concentration gradient, electric potential and to transmit chemical signals. To carry out these tasks, living organisms have evolved a sophisticated arsenal of membrane receptors, photo-activated proton pumps and membrane ion channels that form highly-efficient and selective pores in lipid membrane. Discovery of one-dimensional nanomaterials such as carbon nanotubes (CNT) and silicon nanowire (SiNW) that has characteristic dimensions comparable to the size of biological molecules opens up the possibility to integrate these biological components in electronic circuits for achieving and controlling increased functionality. A considerable effort has also been made on creating biomimetic nanopores that replicate some of the transport properties of the biological channels. Biological molecules are in the plasma membrane, which consists of membrane phospholipids arranged in two layers of tightly packed lipid molecules with their polar heads on the outside and hydrophobic tails inside[1]. Supported phospholipid bilayer closely mimics a cellular membrane and is a universal matrix for housing transmembrane proteins[2]. Lipid bilayer could serve as a versatile platform for creating nanoelectronics with functional biological molecules and assembly of synthetic membrane channel to mimic biological protein pore.

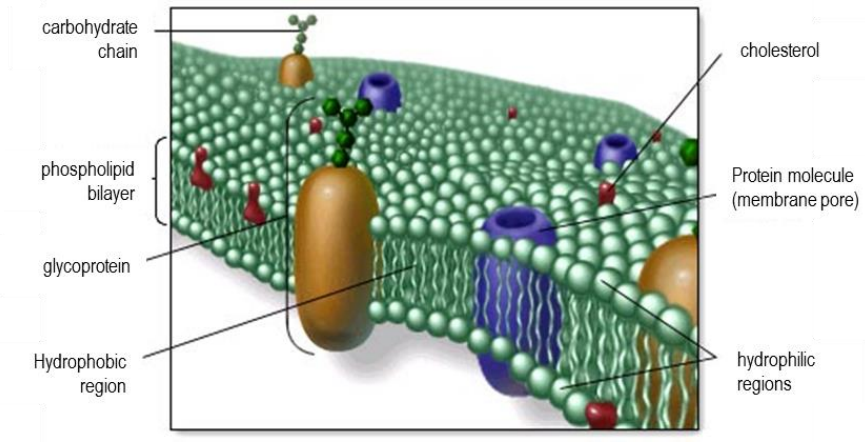

Figure 1.1 Illustration of a cellular membrane. It is composed primarily of phospholipids and transport proteins. The lipid molecules consist of the hydrophilic heads and hydrophobic tails (*credit: © 2007 McGraw-Hill Higher Education)*

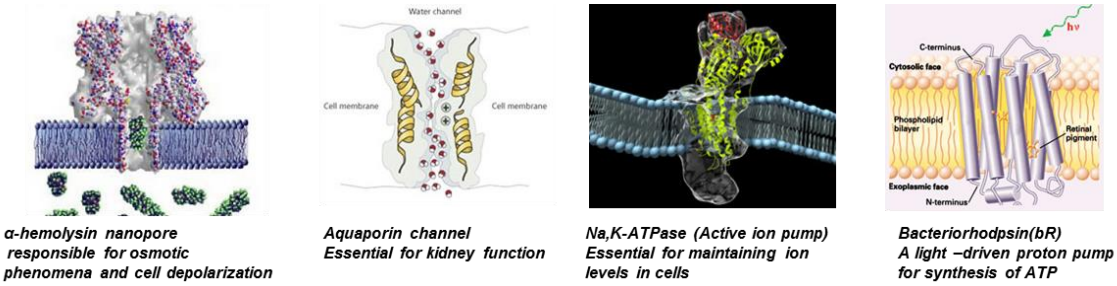

Figure 1.2 Schematic of biological molecules such as membrane channels and pumps

Biomimetic transmembrane carbon nanotube pores: Artificial nanopores have emerged as an exciting field with applications in nanofluidics, membrane technology, pore-based sensing and artificial skin. Biological membrane channels are very important in the activity of living cells. Ion channels in nature allow ions to flow across cellular membranes and shows two aspects of channel functioning with gating and selectivity in the ions[1]. Even though many efforts and progresses, the nature of biological machines are very complicated and their ion transport mechanism still has not been fully understood. Here, more simplified and robust platform is required for understanding of how they transport at the nanoscale. Although bottom-up synthesis using DNA origami technology[3], and top-down fabrication such as focused-ion-beam (FIB) manufacturing[4, 5] and nanofabrication using lithography[6, 7] could produce pores of comparable size, an effective and robust mimic of ion channel have not been made. An unresolved challenge still remains to build nanopore scaffolds that fully replicate affinity and transport properties of membrane channels. Recent experimental and theoretical works presented that CNT is a promising candidate for simplified models of membrane nanochannels. There is a similarity between nanotubes and aquaporins, which are proteins embedded in cell membrane and regulate water flow across cell membrane. Inner pores of CNT is narrow, hydrophobic and very smooth. Surface properties are very similar to those of aquaporin. It is reported that the calculated rate of water transport is comparable to that of aquaporin water transport [8, 9].

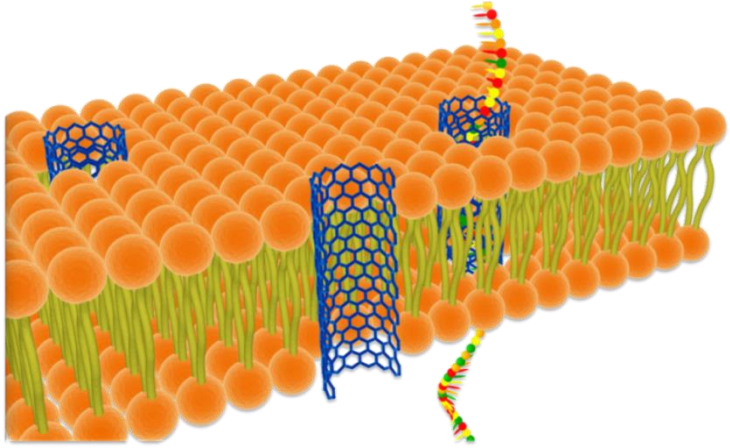

Figure 1.3 Illustration of conceptualized biomimetic transmembrane CNT channels [3]

Recent computer simulation work predicted that a very short nanotube with a length comparable to the lipid bilayer thickness could self-insert into the membrane and form a pore with properties closely matching those of a biological membrane channel[10]. But this possibility had not been demonstrated experimentally yet. Therefore a much shorter carbon nanotube with a length comparable to the lipid bilayer thickness would enable providing a much closer match to a protein-channel structure. To verify that short CNT channels indeed should provide an excellent mimic of a biological channel, they should show similar properties to those of biological channels such as insertion into the lipid membrane and efficient transport of water, ion and small molecules across lipid bilayer and transport properties of gating behavior common in biological channels.

Hybrid bioelectronics with functional biological proteins: Many biological processes involve ion transport across the biological membrane. Previous researchers showed that a one-dimensional silicon nanowire or carbon nanotube can be coated with a continuous lipid bilayer membrane and the lipid bilayer acts as a mimic of cellular membrane, creating an impermeable barrier around shielded 1D nanowires and nanotube and membrane proteins can be incorporated into this barrier[11, 12] (See Fig. 1.5). The hybrid platform of 1D lipid bilayer-inorganic nanostructure enables integrating functionalities of biomolecules such as membrane proteins, channels, and pumps into nanoelectronic devices based on nanowires and nanotubes[13-15]. Bacteriorhodopsin (bR) is a light-driven proton pump and has emerged as an interesting candidate for its functionality integrated into bioelectronic devices due to its photoactivity and unusual stability. To incorporate bR molecules on silicon nanowire device, we need to use template-driven assembly based on one dimensional structure comparable to the size of biological molecules. Incorporation of bR molecule functionality in lipid bilayer allows the bioelectronics device to convert protein photocycle events into a transistor response like a biological gate. Biological regulation mechanisms can be tuned for bioelectronics device performance.

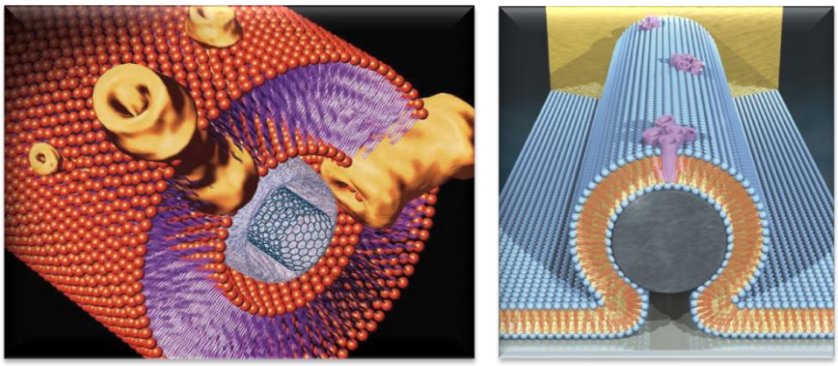

Figure 1.4 Illustration of conceptualized bionanoelectronic platform using nanowire or nanotube as underlying template for self–assembly of lipid molecules [12, 16]

1.2 Scope of the Dissertation

The main objective of this study is to investigate experimentally transmembrane transport properties in biomimetic assemblies based on one-dimensional nanomaterials. This dissertation is organized into the following four chapters.

In Chapter 2, the synthesis and characterization of ultrashort carbon nanotubes (CNT) are presented. Short carbon nanotubes incorporated into a lipid membrane can form pores with transport properties similar to that of biological protein channels. Thus a much shorter carbon nanotubes could give a structural and functional mimic of biological channels.

In Chapter 3, I will introduce carbon nanotube porins. Since the graphitic structure and functionality of these channels resembles the β-barrel structure of porins—water filled channels in biological membranes— we termed them "*carbon nanotube porins"*. I will report on the incorporation of ultrashort CNTs into liposomes and osmotically-driven experiment to understand transport properties of water, ion, proton and small molecules through CNT porins in lipid membrane. The rejection properties of CNT porins can be controlled by the charge at the pore entrance. CNT porins inserted in the lipid membrane also display stochastic gating behavior like biological channels. Electrophoretically-driven translocation of individual sing-stranded DNA molecules though the CNT porins will be discussed. CNT porins represent a robust and versatile biomimetic scaffold for studying biological channels, artificial cell design and stochastic sensing.

In Chapter 4, the bionanoelectronic devices based on functional protein incorporated lipid bilayer-silicon nanowire platform is conceptualized and realized. Silicon nanowire transistors are used for assembly with the output controlled by a photo-activated proton pump, bacteriorhodopsin (bR), reconstituted on lipid membrane covering the nanowire. I will present template-driven assembly to incorporate membrane protein pumps and ionophore molecules in nanowire transistor, and biological regulation mechanisms altering electronic device functionality. This chapter also covers the nanowire growth by chemical vapor deposition (CVD) method, fabrication process of silicon nanowire field effect transistor as a bioelectronics circuit and characterization of SiNW supported lipid bilayers.

Chapter 2 Ultrashort Carbon Nanotubes

2.1 Transmembrane Carbon Nanotube Pores as Biological Ion channel Analogs

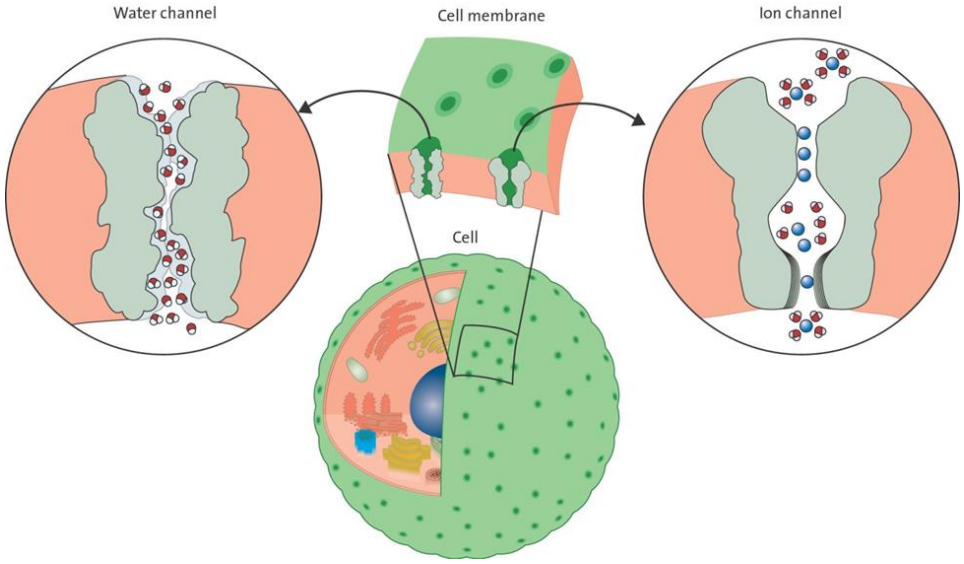

Figure 2.1The dividing wall between the cell and the outside world, perforated by various channels such as a water channel and an ion channel *(credit: nobelprize.org)*

Biological ion channels display a level of sophistication in managing molecular scale transport that is largely unmatched by inorganic analogs. Biological structures do provide some guidance for development of lipid membrane pores. Despite remarkable functional diversity of membrane channels, their structures share a number of common features: crystallographic structures of H_2O, Na^+, K^+, Ca^{2+}, and Cl^- transport proteins [17-21] show hydrophobic inner pores surfaces lined by the hydrophobic residues, and a separate selectivity region of charged residues that provide control over the pore rejection properties.

Carbon nanotubes provide a unique materials platform that can replicate many of these features. Narrow (1-2 nm typical diameter) hydrophobic inner pores of carbon

nanotubes are remarkably similar to protein pores [22]. Not surprisingly, carbon nanotubes have already been a subject of several nanofluidic studies using membrane platforms [23, 24] and individual macroscopically-long nanotubes [25, 26] where researchers showed that transport of water, ions, and gases in the nanotube channels is remarkably fast [23, 27]. Indeed, reported transport rates are comparable to those of biological systems: for example, the water transport rate in carbon nanotube pores (1.4 molecules/ns) and in aquaporins (6 molecules/ns) are within an order of magnitude from each other [23].

All existing experimental systems for measuring transport through CNTs involve formidable fabrication challenges and a biomimetic system based on carbon nanotubes embedded in lipid bilayers would provide a much easier and much more versatile experimental platform.

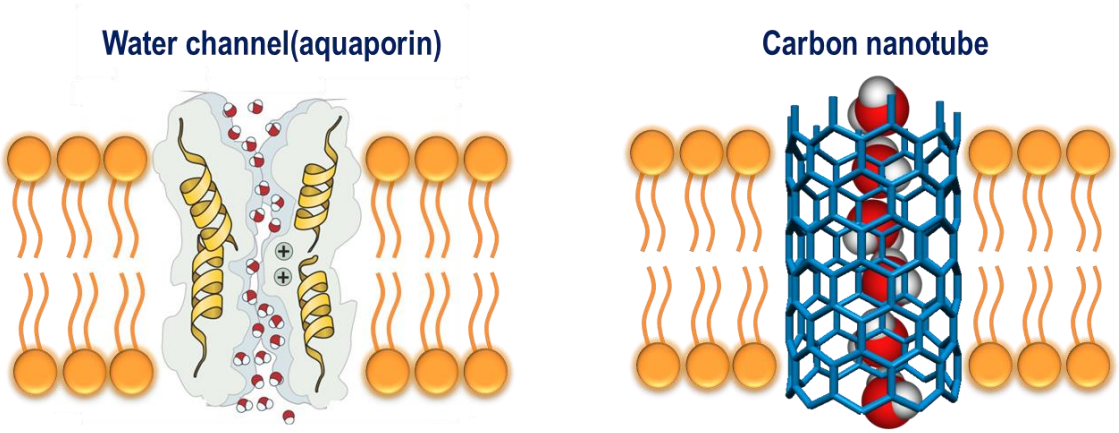

Figure 2.2 Schematic of transmembrane biological protein channel and CNT pore forming a biomimetic ion channel

A much shorter carbon nanotube with a length comparable to the lipid bilayer thickness would provide a much closer match to a protein-channel structure. Computer simulations also predicted that a very short nanotube with a length comparable to the lipid bilayer thickness could self-insert into the membrane[28, 29] and form a pore with properties closely matching those of a biological membrane channel; yet this possibility had thus far not been explored experimentally. Short carbon nanotube pores could provide both a structural and functional mimic of a biological channel.

2.2 Synthesis and Characterization of Ultrashort Carbon Nanotubes

2.2.1 Carbon nanotube preparation, cutting and purification

Carbon nanotubes have been studied extensively since their discovery. However, to facilitate applications in biological systems, it is very important to obtain very short carbon nanotubes with narrow length distributions. Many methods have been studied to cut carbon nanotubes, including strong oxidizing acid treatment,[30, 31] mechanical milling,[32-39] sonication, [40-42] fluorination, [43, 44] nano-lithography,[45] and direct cutting.[46] Most methods can obtain carbon nanotubes down to about 200-300 nm. Recently, Dai et al used sonication method with the help of polymer surfactants method to cut carbon nanotubes(CNTs) and obtained short CNTs of sub-10 nm length,[41] but most cut CNTs are much longer. It is sought to prepare very short CNTs whose length is shorter than 10 nm in higher yield, so that these very short CNTs can be integrated into lipids bilayers to mimic ion channels in biological systems. I have used probe-sonication to cut CNTs and tried many methods to incorporate the short CNTs into DOPC liposomes. In this report, I describe the cutting procedure with DOPC molecules and the measurement of proton transportation. The procedure is based on the results that yield different transportation rate between DOPC vesicles and vesicles with CNT channels

1.5 nm diameter single-walled carbon nanotubes (CNTs) synthesized by chemical vapor deposition (CVD) were purchased from NanoLab Inc. (product purity of > 95%). 1, 2-dioleoyl-sn-glycerol-3-phosphocholine in chloroform (DOPC, 10 mg/L) was purchased from Avanti Polar Lipids, Inc. Prior to use, 1.6 to 2 mg of CNTs was purified in a thermal gravimetric analysis (TGA) system (Q5000IR TGA-MS, TA Instruments) using 25 mL/min stream of air while ramping the temperature at a rate of 5ºC/min up to 450ºC. This procedure removes amorphous carbon and impurities in the sample.

A field-emission Philips CM300 was used to characterize the uncut CNT samples. The uncut long carbon nanotubes were prepared for TEM imaging by first dispersing the CNTS in highly pure ethanol solvent. Ultrasonic agitation in a bath sonicator can make the CNT bundles become loose and uniformly dispersed in solvent. The CNTs dispersed in ethanol using 30minutes of bath sonication solvent were drop-cast onto lacey carbon TEM grids. As indicated in Fig. 2.3 the as-purchased CNTs contain both single-walled and double-walled tubes. The average diameter of uncut CNTs was 1.51±0.21 nm as determined from over a dozen individual tubes. Bundles of CNTs were also observable in the TEM images. Note that some CNT walls appear to be defective, which was likely caused by the high-voltage electron beam damage during the imaging. Although the sample contains a fraction of double-wall CNTs we expect them to be significantly more resistant to sonication-assisted cutting. Since longer and heavier CNT fragments are removed during centrifugation step, our purified short CNT sample should contain mostly single-wall carbon nanotube fragments.

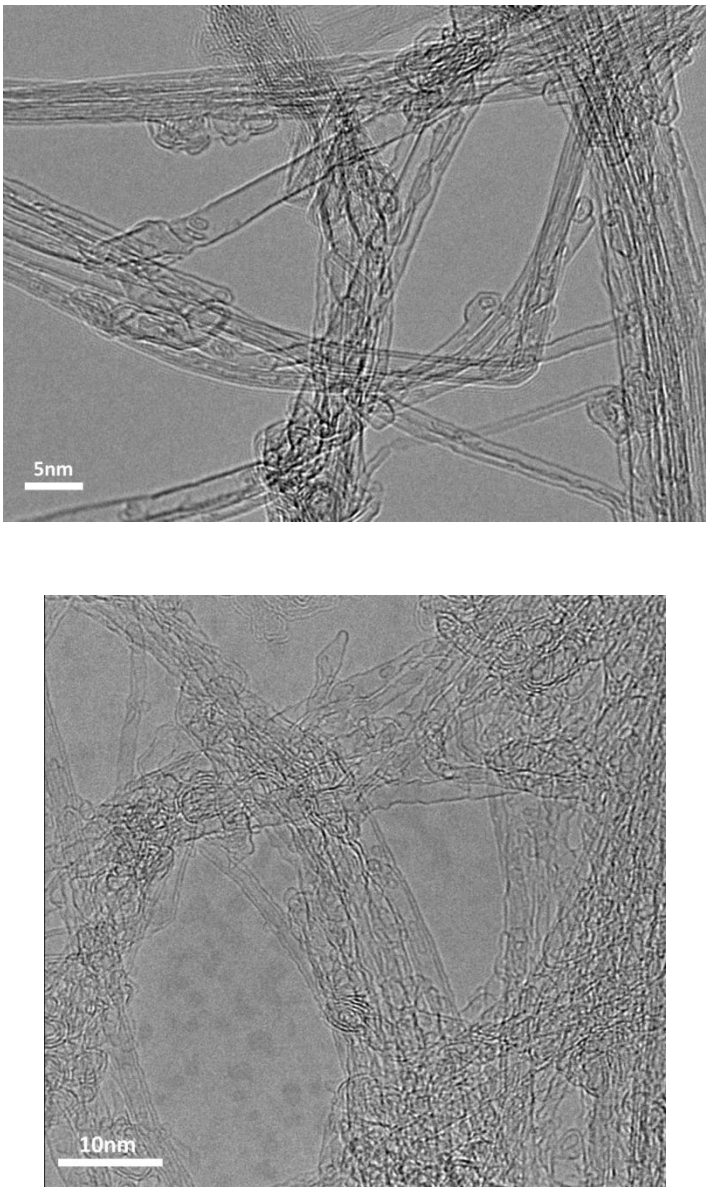

Figure 2.3 TEM images of uncut purified CNTs

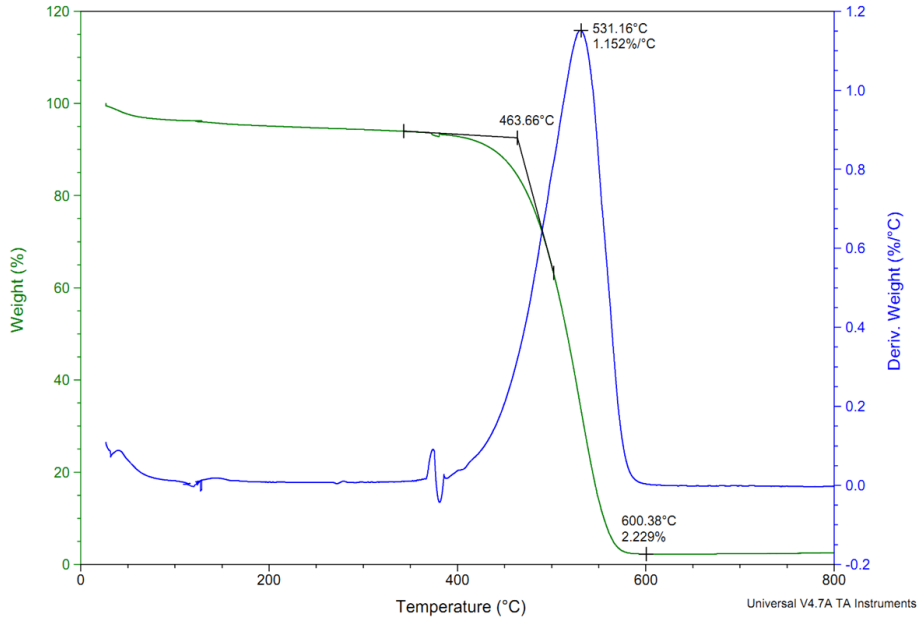

Figure 2.4 Typical TGA profile for single-walled carbon nanotubes

The above Fig. 2.4 shows typical TGA profile for carbon nanotubes. In this profile the onset oxidizing temperature is 463ºC and maximum oxidizing temperature is 531^{o}C. The derivative profile exhibited a sharp peak. At 600ºC most SWNTs were consumed and only ~2% ashes content was left. This suggests the SWNTs sample contains only a small amount of metal impurities. Since there is no significant mass lost below 400ºC, most content should be carbon nanotubes. It was sought to determine the temperature that can cause defects on the walls of SWNT without burning off SWNTs. From this profile, 450ºC is chosen, slightly below the onset temperature. The onset temperature may change between 420 and 460ºC according to the experimental variation. The maximum oxidizing temperature is usually between 480 and 550ºC.

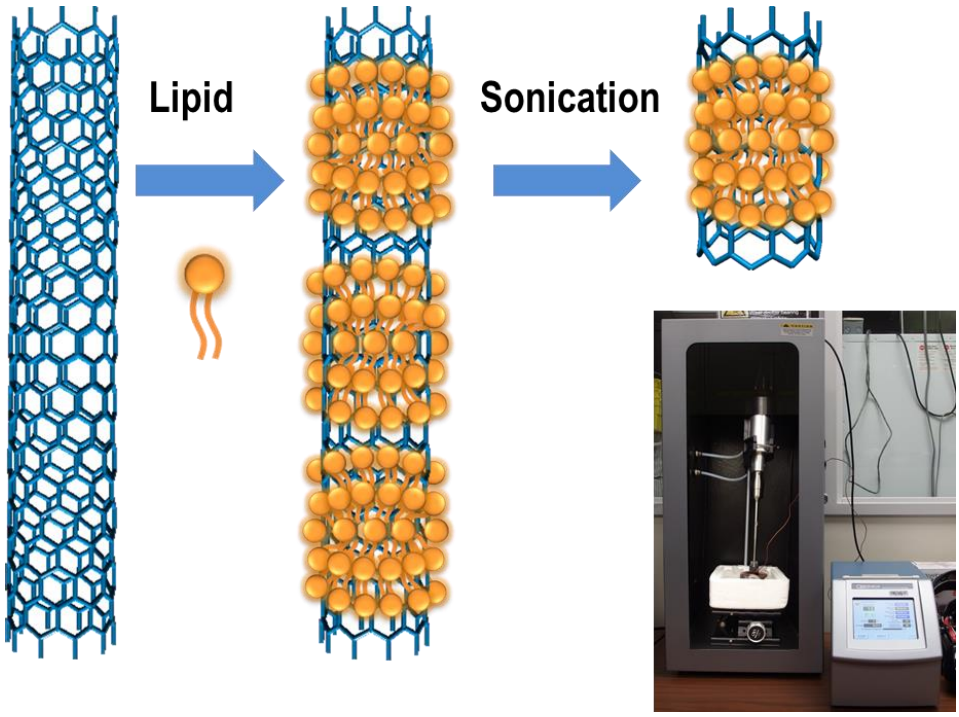

Figure 2.5 Schematic of ultra-short CNT sample preparation and probe-sonicator setup

Most common synthetic techniques produce carbon nanotubes that are much longer than the ~ -5nm length that is necessary to match the thickness of the lipid bilayer. Thus it is needed to cut those longer nanotubes into shorter segments. To create CNT fragments with the length that matches the thickness of the lipid bilayer, we have modified the surfactant-assisted cutting procedure reported by Dai and co-workers[47] to include the critical step of pre-assembly of the lipid molecules on the nanotubes surface (Fig. 2.5). Phospholipid molecules form regular structures on the nanotube surfaces[48], and our cutting procedure exploited the ability of these assemblies to protect segments of the nanotube surface from damage during sonication.

For a typical CNT pore preparation procedure 2 mL of DOPC (10 mg/mL in chloroform) was placed into a 20 mL glass vial and the solvent was evaporated in a Biotage-V10 Evaporator to form a thin lipid film on the walls of the glass vial. 1.6 mg of purified CNTs and 20 mL Milli-Q water was added to the same vial. The mixture was first bath-sonicated for 1 hour (Emerson Electric Co., Model Branson 1510), followed by probe-sonication for 16 hours (Sonics & Materials Inc., Model VC 100) at 100W power. The sonicator was run in 3 second pulses with 1 second pause between pulses. During sonication the vial was continuously cooled in an ice water bath and DI water was added to compensate for any loss in sample volume due to water evaporation. To separate the cut CNTs from the uncut nanotube material, 10mL of suspension processed by sonication cutting was placed into a 15mL centrifuge tube and centrifuged at 4000rpm for 1 hour using a Beckman Coulter Allegra X22 centrifuge. After centrifugation, the supernatant that contained the purified CNT+DOPC complex was extracted by a 150mm length glass Pasteur pipette. The dark solution containing lipid-stabilized cut carbon nanotube was

stable for more than 15days. This solution can be dried and re-suspended in DI water without affecting the short CNT properties.

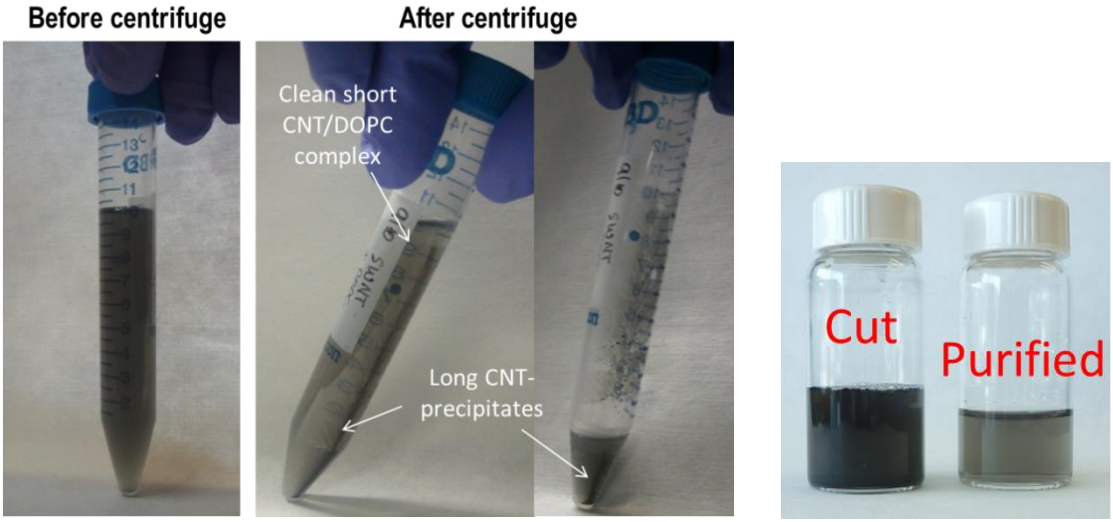

Figure 2.6 Suspension of cut CNTs before and after purification

Sixteen-hour-long sonication-induced cutting of purified 1.5±0.21nm average inner diameter CNTs followed by separation of longer uncut fragments by centrifugation produced a stable dark suspension that contained cut carbon nanotubes stabilized by the lipid coating (see Fig. 2.6). The sample can be dried repeatedly and re-suspended in water, indicating that lipid coating protected the short CNTs from forming large aggregates.

2.2.2 Characterization of ultrashort carbon nanotube pores

Raman spectroscopy characterization of short CNTs indicates cutting procedure did not destroy the basic roll-up grapheme sheet structure of the nanotube. Atomic force microscopy (AFM) images and transmission electron microscopy (TEM) images of the purified short CNT pores indicate that the purified product still contains a fairly wide distribution of the nanotube lengths with a significant population of CNT fragments in the sub-10 nm range. Significantly, the average nanotube length of 4.8±3.7 nm determined from the AFM images, which was obtained after the correction for AFM tip broadening, matched very well the 4.6±0.2 nm thickness of the 1,2-dioleoyl-sn-glycero-3-phophocholine (DOPC) bilayer. The average CNT height observed in the AFM images, 1.54±0.44 nm, matches quite well the 1.51±0.21 nm CNT diameter determined from TEM images of uncut carbon nanotube. Thus it is likely that the AFM probe was able to push away the lipid coating that remained on the cut carbon nanotubes. High-resolution TEM images also confirmed the existence of a large population of short CNT fragments in the purified mixture. The average length of the nanotube fragments determined from those images, 10.1±5.4 nm, was longer than the 4.8nm length determined from the AFM

images and the nanotubes appeared thicker than 1.5 nm. The additional thickness from the lipid coating is likely to responsible for these effects.

Raman spectroscopy displays the basic spectroscopic characteristics of carbon nanotubes. A droplet of short CNT+DOPC complex (or uncut purified CNT) suspension was placed onto a glass cover slip and dried down. Raman spectra of short CNTs were obtained using Renishaw micro-Raman Spectrometer using 488nm laser illumination. Raman spectrum of cut CNTs in Fig. 2.7 below shows a G-band and D-band peaks at ~1600 cm^{-1} and ~1300 cm^{-1} with the G/D ratio of 8 and confirmed that the cutting procedure preserved the inner diameter and rolled-up grapheme sheet structure of the nanotube remarkably well. The diameter of carbon nanotubes can be determined from the radial breathing mode (RBM, peaks in 100~300 cm^{-1}). The CNT diameter calculated from RBM peak is about 1.5 nm. The RBM frequency (ω) is inversely proportional to carbon nanotube diameter (d_{CNT}). The relationship can be described by the equation:

$$\omega_{RBM}(cm^{-1}) = \frac{A}{d_{CNT}(nm)} + B(cm^{-1})$$

, where A = 248 cm^{-1}/nm and B = 0cm^{-1} [49].

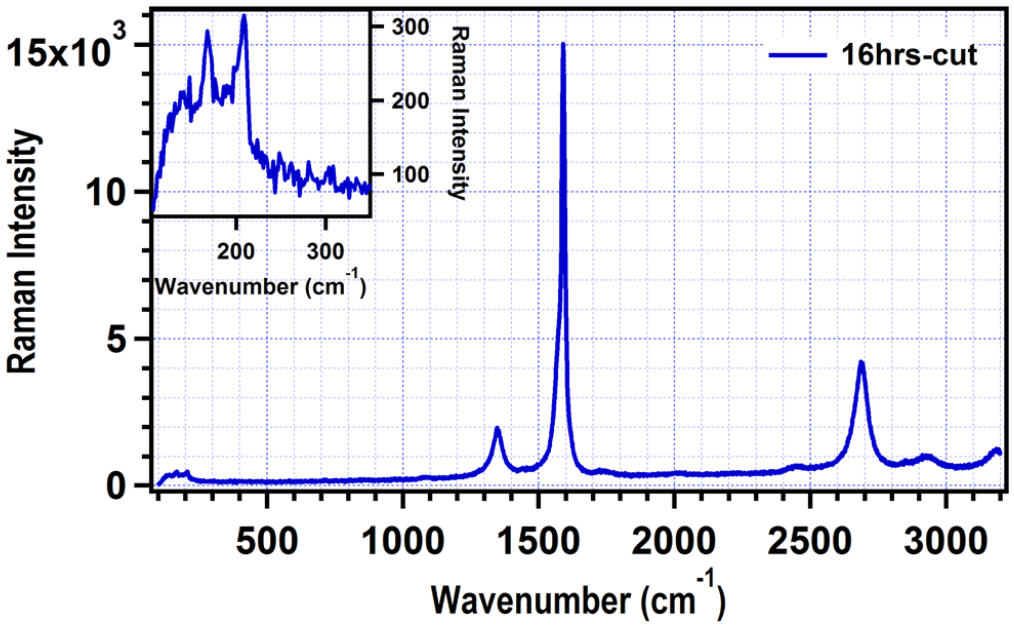

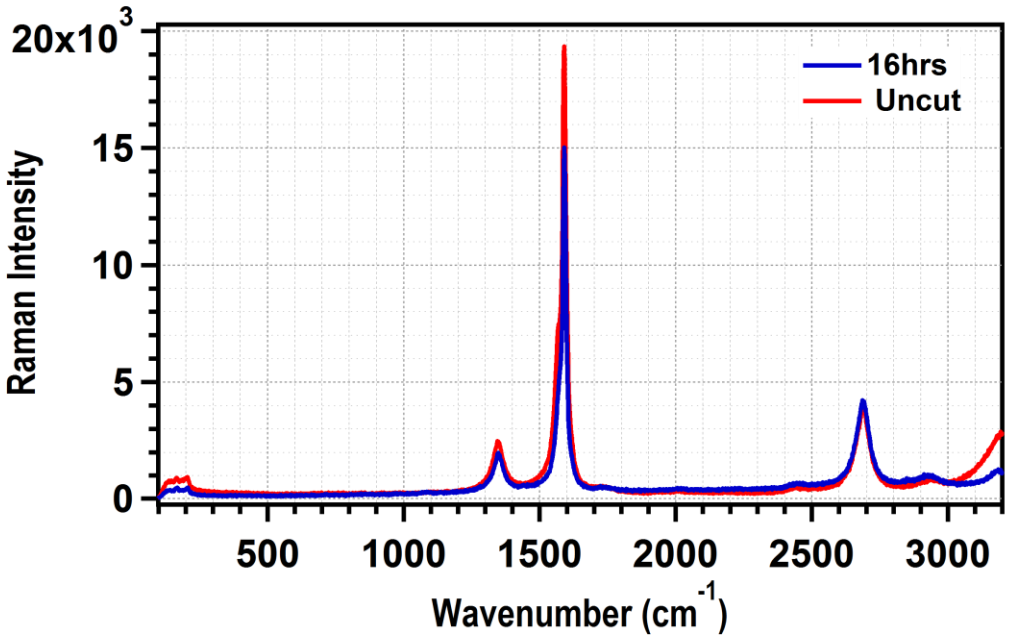

Figure 2.7 Raman spectrum for the short CNT/Lipid complex after 16 hours of sonication-assisted cutting. Inset shows the magnified view of the radial breathing mode region of the CNT spectrum (150-300cm-1).

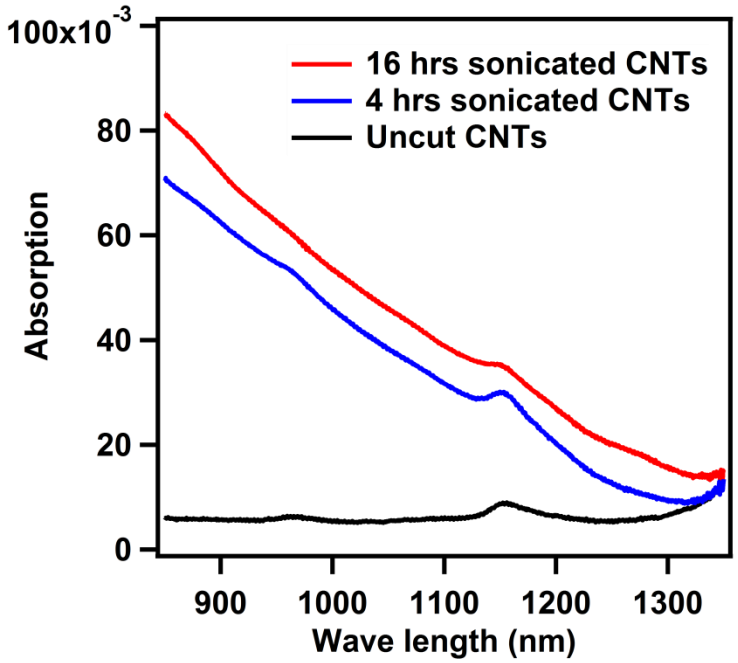

Figure 2.8 VIS-NIR absorption spectra of CNTs before and after cutting

1ml aliquots of uncut CNT suspension in Milli-Q water, four-hours sonicated CNT and 16-hours sonicated CNT samples were placed into quartz cuvettes. The VIS-NIR absorptions spectra in the range from 325 nm to 1350 nm were measured using Agilent Cary 6000 VIS-NIR Spectrophotometer (see Fig. 2.8).

High-resolution TEM images of the purified short CNT fragments (see Fig. 2.9) indicate that the purified product contains a significant population of CNT fragments in the ca. 10 nm range. The average length of the nanotube fragments determined from the TEM images was 10.1±5.4nm. Short CNT/lipid complex was drop-cast onto lacey carbon TEM grids and the CNT fragments were characterized by a field-emission Philips CM300 TEM, operated at 300 kV with the field-emission gun using extraction voltage of 4.2 kV. To characterize the length distribution of short CNTs inside the lipid matrix, the length of identifiable individual CNTs were manually measured from a series of high-resolution TEM images. Due to the effect of lipid layer coating on imaging (Fig. 2.9), shorter CNTs (< 3-4 nm in length) were difficult to resolve and thus were not counted. As such, the statistical average length reported from the TEM images should be considered an upper-bound estimate.

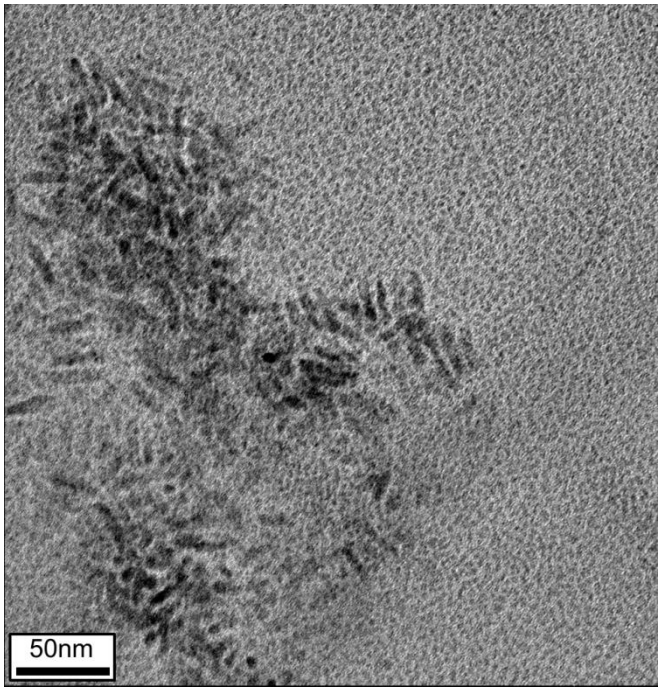

Figure 2.9 HR-TEM image of cut short CNTs stabilized by lipid coating

Atomic force microscopy (AFM) imaging was performed using a Multimode Nanoscope IIIA, Nanoscope VIII AFM (Digital Instruments, Santa Barbara, CA, USA) and Asylum MFP-3D (Asylum Research, Santa Barbara, CA, USA) with both microscopes operating in tapping mode. For imaging in air, silicon tips (PPP-FMR, Nanosensors GMBH, Germany) with a typical tip radius of less than 7 nm, nominal force constant of 2.8 N/m, and nominal resonance frequency of 75 KHz were used. For imaging in solution (*in situ*), silicon nitride tips (TR400PSA, Olympus, Japan) with a tip

radius of ~15 nm, nominal force constant of 0.08 N/m and nominal resonance frequency of 34 KHz were used. For imaging CNTs in air, 10 µL of purified CNT solution was deposited on freshly cleaved mica pre-treated with 10 µL of Poly-L-Lysine solution (Ted Pella) for 2 minutes, gently rinsed with Milli-Q (MQ) water, dried by gentle flow of compressed nitrogen gas, and placed into the microscope. Poly-L-Lysine treatment was necessary to form positive charges on the mica surface to facilitate adsorption on negatively-charged CNTs. For in-situ imaging a 5 µl aliquot the CNT-containing lipid vesicles was deposited on a small piece (3 × 3 mm) of the poly-l-lysine-treated mica, and incubated for 2 minutes. Then the solution on the mica surface was replaced with about 55 µL MQ water without drying the sample and placed into the AFM fluid cell. AFM images showed that the vesicles fused onto the mica surface and formed a layer with a thickness of ca. 4.6 nm.

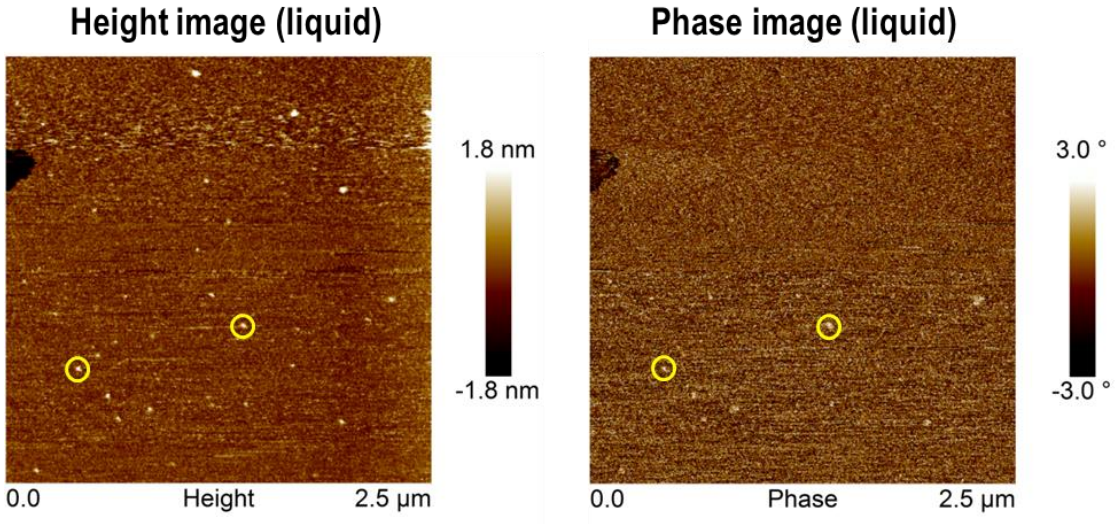

Figure 2.10 AFM images of short CNTs on lipid bilayer formed on a poly-l-lysine treated mica surface

CNT height was determined from the AFM images collected in air. The images were analyzed by the Scanning Probe Image Processor (SPIP 5.1.4) software, standard Nanoscope image analysis software, and Igor Pro 6.0 (Wavemetrics, Inc.). AFM images typically represent a true height value of the CNTs. The average CNT height observed in the AFM images, 1.54±0.44 nm, match the CNT diameter value determined from the Raman spectra and TEM data.

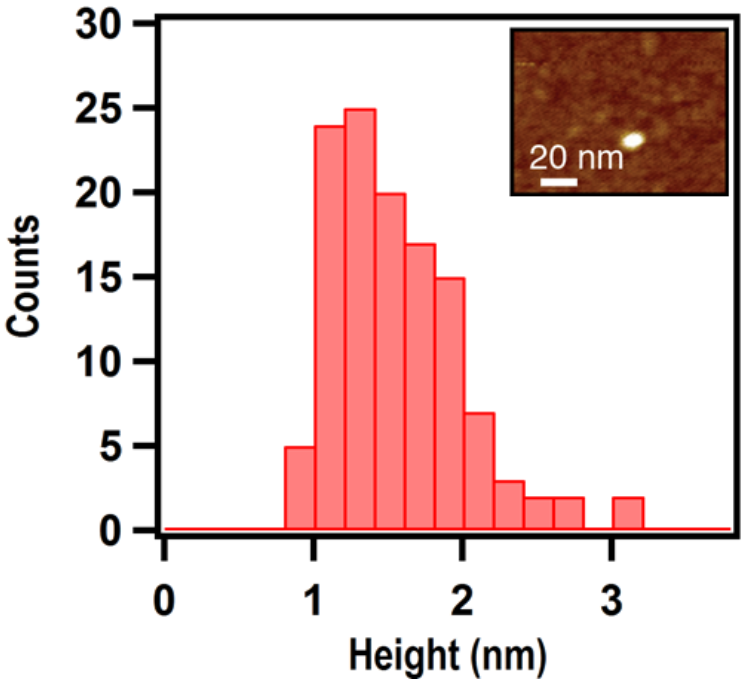

Figure 2.11 Histogram of the height (diameter) of short CNT fragments measured with AFM. Inset shows a high-magnification AFM image of a single CNT on a bare mica surface.

Chapter 3 Molecular and Ion Transport through Carbon Nanotube Porins in Lipid Membranes

3.1 Introduction to Molecular Transport through Biomimetic Transmembrane Nanopores

Living systems rely on controlled transport of ions or small molecules across biological membranes to maintain non-equilibrium concentration gradients and to transmit chemical signals. To carry out these tasks, biological organisms have developed an arsenal of membrane channels [1] that form nanometer-sized highly-selective pores in lipid bilayers. Many of these membrane channels are exemplary in their structural refinement and functional sophistication: aquaporins support exceptionally-fast water transport [50]; potassium channels transport potassium ions exclusively over sodium ions [51], even though the ion radii of these ions differ only by 0.2 Å [52]; and ion pumps shuttle ions upstream against strong concentration gradients [53]. Protein channels also occupy an important role in *ex-vivo* applications; notably, researchers have successfully demonstrated pore-based DNA sequencing using pores derived from α-haemolysin channels [54].

A considerable effort has also been spent to create artificial nanopores that replicate some of the transport properties of the biological channels. Bottom-up organic synthesis approaches produced pore-forming compounds such as tris-macrocycle hydraphiles [55, 56], and top-down nanofabrication provides an alternative route based on drilling small holes in thin films of inorganic materials, such as silicon nitride [57]. Researchers also used DNA origami platform to create 2 nm inner diameter pores in lipid membrane [3]; another work demonstrated a combined approach where an α-haemolysin biological pore partially refilled a pre-drilled solid state nanopore [58]. Even though these systems replicate some of the membrane affinity and transport control properties exhibited by membrane proteins, there remains a need for simpler and more versatile nanopore scaffolds based on a different structural paradigm. In this regard, short carbon nanotube that matches the lipid bilayer thickness can create an artificial membrane pore that closely mimics the transport properties of biological pore proteins.

In this Chapter, I show that short CNT channels indeed provide an excellent mimic of a biological channel, including spontaneous insertion into the lipid membrane and efficient transport of water, ions and small macromolecules, such as DNA, across the

bilayer. I also report on the transport properties of a single CNT channel, including an unexpected spontaneous "gating" behavior. Since the graphitic structure and functionality of these channels resembles the β-barrel structure of porins—water filled channels in biological membranes— we termed them *carbon nanotube porins*.

3.2 Carbon Nanotube Porins in Lipid Membranes

3.2.1 Synthesis and characterization of transmembrane CNT-liposomes

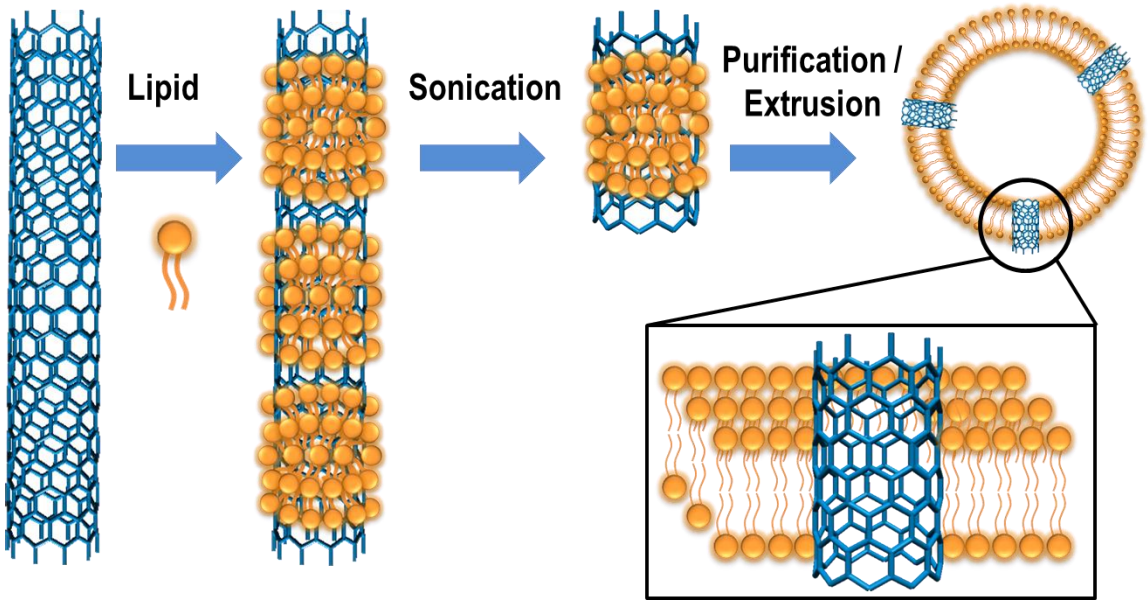

Figure 3.1 Schematic showing synthesis of transmembrane CNT pores - Incorporation of CNT pores into lipid vesicles

Following purification, the cut carbon nanotubes were reconstituted into the lipid vesicles following the common procedures for protein channel insertion into membranes. To incorporate CNTs into DOPC vesicles, a 0.2 mL aliquot of 10mg/mL DOPC in chloroform was placed in a 20 mL glass vial and dried into a film by evaporating the solvent with Biotage-V10 evaporator. 1 mL of purified CNT+DOPC complex solution was added into the vial and the vial content was allowed to hydrate over one hour. The solution was then extruded through a 200 nm-diameter pore polycarbonate membrane using a hand-held extrusion device (mini-extruder, Avanti Polar Lipids) for 10 cycles. The transparent solution that passed through the filters contained the lipid vesicles with incorporated carbon nanotube pores.

The resulting CNT porins incorporated vesicles were characterized by Scanning Electron Microscopy (SEM). 5 μL of CNT-containing liposome solution was drop-cast onto a pre-cleaned silicon chip and dried in clean chamber. To prevent charging artifacts the samples were sputter-coated with gold for 10 sec at the deposition rate of 9 nm/min to produce a nominally 1.5nm-thick coating. Images of CNTs-containing liposomes were obtained using Zeiss Ultra 55 FE SEM. SEM images (Fig. 3.2) of these vesicles drop-cast on the silicon surface and coated with a thin layer of gold showed an array of bright.

We speculate that these dots are indicative of the nanotube porin inclusion in the lipid bilayer. Images of a control sample of the vesicles consisting only of the DOPC lipid consistently did not show any evidence of such pattern. The vesicles showed significant degree of CNT pore loading with an average nanotube density of 0.9±0.2 channels in a $100\times100nm^{-2}$ area on lipid membrane surface (giving the average CNT pore/lipid ratio of 5.4×10^{-6}). In some of the images CNTs inserted into the membrane seemed to oligomerize further into bundles of 2, 3 and 4 pores (see Table 3-1). Similar behavior is not uncommon for biological channels [59], and such short CNT aggregates would be stabilized by additional interactions between hydrophobic barrels of CNT channels.

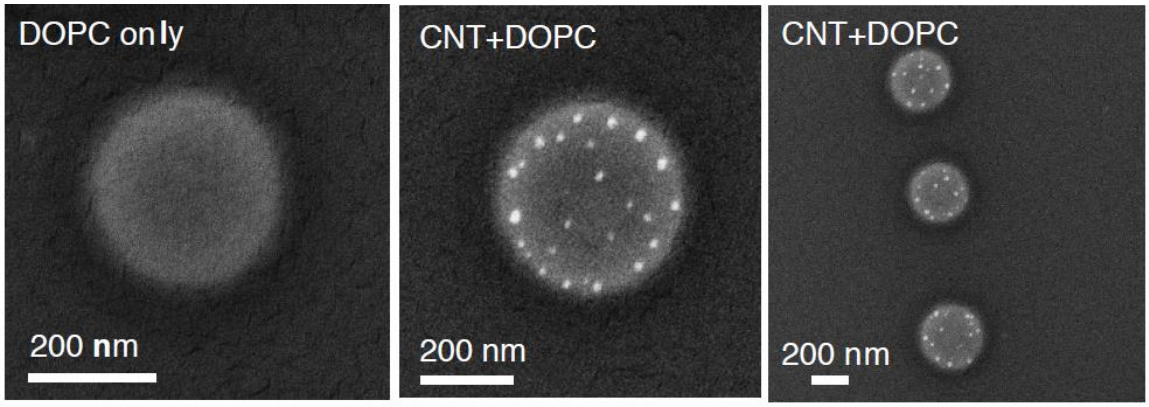

Figure 3.2 SEM images of the vesicles dried on a Si surface

The number of CNT-lipid complex in the vesicles was estimated from the SEM images. The analysis (Table 3-1) included 17 individual vesicles out of which 12 contained CNT pores.

After reconstitution of purified short CNT fragments into 200 nm diameter lipid vesicles, the resulting vesicles were also imaged by using cryogenic transmission electron microscopy (Cryo-TEM). The cryo-TEM images of the CNT/liposome complexes shown in Fig. 3.3 and Fig. 3.4, together with their unprocessed originals, as well as the images of some additional CNT-liposome regions of interest. In Fig. 3.4 two unprocessed images show the original large field of view with a selected CNT-liposome structure shown inset in each.

Table 3-1 Counting of number of CNT/liposome in vesicles

	N = 12
Vesicle diameter (nm)	201.17 ± 34.14
Number of CNT pores per vesicle	23.17 ± 6.9
Number of CNT pores / 100 nm^2	0.91 ± 0.18*

*Out of 17 vesicles, 5 were empty. If we include the empty vesicles in the analysis, then the average number of CNT complex per 100 nm^2 area would be 0.64 ± 0.45.

The images of the vesicles revealed clear evidence of short CNT fragments inserted in the lipid membrane and spanning both of the membrane leaflets (Fig. 3.3). Cryo-TEM images also show that the presence of CNT porins does not affect the integrity of the lipid bilayer. Statistical analysis of cryo-TEM data reveals several interesting features of the CNT porins. First, the average length of the CNTs inserted into the membrane, 9.5±3.0 nm was in excellent agreement with the 10.1 nm average length of the cut CNTs, indicating that the insertion procedure was not selective to any particular length. Second, CNT porins did not insert into the membrane at random angles. The histogram of the measured tilt angles (Fig. 3.5) shows that the nanotubes strongly prefer the perpendicular orientation to the membrane plane with the majority of the nanotube tilting only by 15 degrees or less. This observation is somewhat surprising, since MD simulations had predicted that CNTs longer than the thickness of the bilayer (4.6±0.2 nm for the 1,2-dioleoyl-sn-glycero-3-phosphocholine (DOPC) that was used in these experiments) should tilt to maximize the interactions of the hydrophobic bilayer core with the hydrophobic CNT walls[28]. It is possible that the lipid coating remaining on the walls from the cutting procedure provided additional stabilization to the portion of the CNT that protruded from the bilayer. Higher contrast (Fig. 3.3) on the protruding portion of the CNT porins that we sometimes observed in the cryo-TEM images supports this possibility. Third, CNT porins were always inserted in such a way that at least one end of the channel abutted the hydrophilic head groups of the lipid bilayer. Unlike the situation when both of the CNT porin ends protrude into the solution, this configuration does allow for the energetically favorable interactions of the hydrophilic groups on one of the CNT ends with the hydrophilic head groups of the lipid bilayer.

*Cryo TEM specimen preparation and instrumentation***.** Aliquots of 5 µl were taken directly from the *in-vitro* assembled samples, placed onto 200 mesh lacey carbon Formvar Cu-grids (Ted Pella, INC, #01881), and manually blotted with filter paper and plunged into liquid ethane at liquid nitrogen temperature. TEM grids were previously glow discharged. Images were acquired on a JEOL–3100-FFC electron microscope equipped with a field emission gun (FEG) electron source operating at 300 kV, an Omega energy filter, and a cryo-transfer stage. Images were recorded on a Gatan 795 4Kx4K CCD camera (Gatan Inc., Pleasanton, CA, USA) mounted at the exit of an electron

decelerator operated at 200 kV, resulting in images formed by a 100 kV electron beam at the CCD. The stage was cooled with liquid nitrogen to 80 K during the acquisition of all datasets.

Cryo TEM image acquisition and analysis. Images were recorded at a nominal magnification of 40,000× giving a pixel size of 0.14 nm at the specimen. Images were acquired without binning and with the camera binned by a factor of two. Underfocus values ranged from 2 µm ± 0.25 µm to 3.6 µm ± 0.25 µm, and energy filter widths were typically around 30 eV. The survey of cryo samples and the selection of suitable targets were done in low-dose defocused diffraction mode. Images were acquired under low-dose conditions, typically with doses of ~ 20-40 e^{-} $Å^{-2}$ per image. The package of imaging tools Priism (http://msg.ucsf.edu/IVE/) was used for noise reduction and contrast enhancement. The software ImageJ 1.38x (NIH, http://rsb.info.nih.gov/ij/) was used for analysis and measurements of the 2D image projections. Since the images represent a 2-D projection of a 3D structure the measured CNT length values represent the lower boundary estimate of the true CNT lengths.

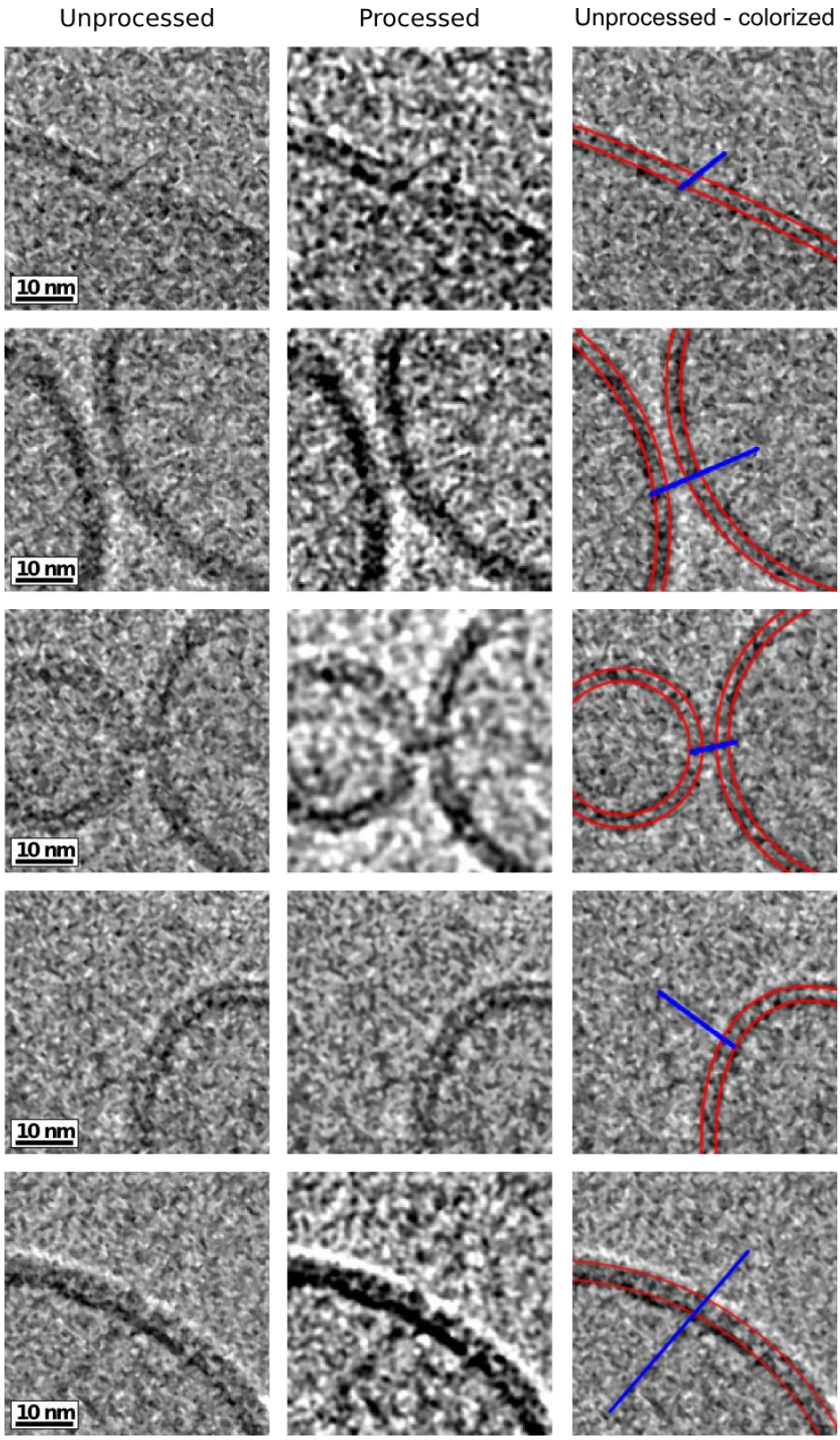

Figure 3.3 Cryo-TEM imaging of CNT-Liposome complexes showing unprocessed, processed, and colorized examples

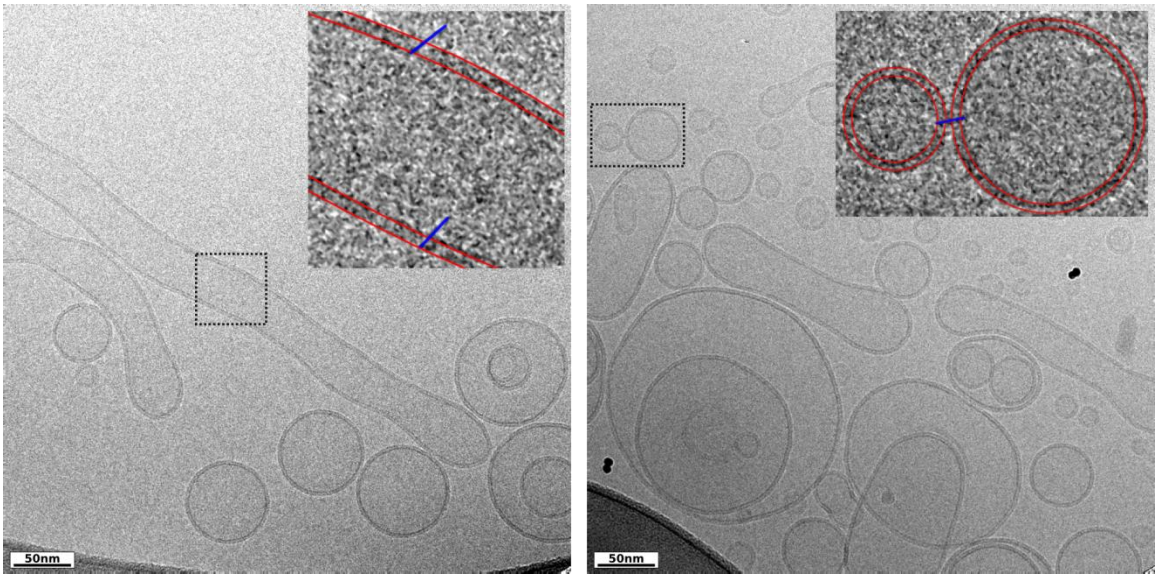

Figure 3.4 Cryo-TEM images of CNT-Liposome complexes showing original images with large-field-of-view and selected structures inset

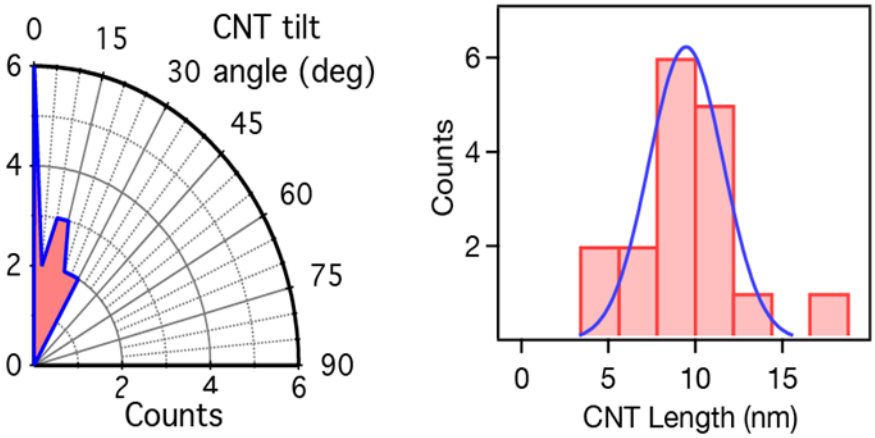

Figure 3.5 Radius plot of the histogram of CNT tilt angles measured relative to the axis normal to the bilayer plane(left) and histogram of CNT tilt angles of the CNT inserted into the lipid membrane (right). CNTs strongly prefer the perpendicular orientation to the membrane plan

3.3 Osmotically-driven Water, Proton and Ion Transport through Biomimetic CNT Porins

3.3.1 Introduction

Natural cells have diverse types of membrane protein channels regulating the flow of ions and molecules. Ion and water transport through biological membranes by osmosis is essential in many biological processes. The complex nature of biological pores and channels important to cellular function is not fully understood. It is desired to create a simplified and robust platform for the understanding of ion transport mechanism. Ion and molecular transport at nanoscale has been studied extensively [8, 60, 61], especially the transport through carbon nanotube due to its extraordinary transport properties. Both simulation and experiment studies have shown that water transport through CNT channel is almost frictionless, and can be comparable to the transport capabilities of aquaporin [8, 23, 62]. Various methods have been used to study the water filling and transport in nanotubes have been studied using TEM [63], current measurement[64, 65], field effect transistor [66] and X-ray [67] et. al. However, the channel length of nanotube in many of those studies were longer than that its biological counterpart, thus a biomimetic channel that is similar with biological channel both in structure and function is greatly desired.

As described in Chapter 2, biomimetic CNT porins were synthesized and characterized[11]. This CNT porin has a diameter of ~1.5 nm and a length of 6-12 nm. A more attractive feature is that the CNT is embedded in the lipid membrane of vesicles, forming a perfect channel with extraordinary properties of transmembrane ionic and molecular transport, and stochastic gating [68]. Since liposome shows similar permeability properties to biological membranes and gives a convenient model system to study osmosis-related phenomena, it would be interesting to investigate the water and ionic transport through this biomimetic channel, and investigate selectivity on the species of ions and molecules being transported.

Biological membrane consisting of phospholipid bilayer is selectively permeable to ions and organic molecules. Small, nonpolar molecules move easily across, while large molecules and charged substances across membrane slowly. Very small and uncharged molecules can cross membrane relatively faster than ions such as chloride. Lipid bilayer is highly permeable to water in comparison with ions and other solutes and sensitively respond to osmotic pressure across the membrane. Liposomes artificially prepared with a phospholipid bilayer exhibit similar permeability properties to natural membrane and provide a convenient model system to study osmotically induced transport.

Osmotic stress study using artificial vesicles is a convenient way to induce transport across the lipid bilayer. Compared to membrane fabrication and single pore measurement, our approach is much simpler and gives much more robust averaging. Osmotic stress is driven by a sudden change in the solute concentration around a cell and it causes a rapid change of water movement across its cell membrane. Higher osmolality into the vesicle solution creates an osmotic difference across membrane. Here, I report on the osmotic gradient-driven experiment and the monitoring of the vesicle size change in response to created osmotic pressure gradient using dynamic light scattering (DLS).

3.3.2 Proton transport through CNT porins

The central finding of our work is that CNT porins enable efficient transport of chemical species across the lipid bilayer. For initial assessment of the porin properties we have investigated proton transport into the vesicle lumen containing an encapsulated pH sensitive dye (8-hydroxypyrene-1,3,6-trisulfonic acid trisodium salt (HPTS)). For these experiments, we prepared the vesicles with the lumen pH of 8.0 and subsequently transferred them into a solution with pH of 3.0 to create the proton gradient across the vesicle membrane. All solutions also contained a high concentration of background KCl electrolyte to ensure the absence of osmotic pressure gradient across the lipid bilayer.

Proton transport assay. To prepare the CNT-containing vesicles loaded with a pH-sensitive fluorescent dye, a 0.1 mL aliquot of 10 mg/mL DOPC in chloroform was added to a 20 mL glass vial (Vial A), and dried into a film by evaporating the solvent. 1 mL of short CNT+DOPC (1mg/mL) complex solution in 1 mM HPTS, 150 mM KCl pH 8, was added to rehydrate the dried lipid film. The contents of the vial were incubated for one hour for hydration and then extruded through a 200 nm diameter pore polycarbonate membrane. For preparation of a control sample that did not contain CNTs, a 0.2 mL aliquot of 10 mg/mL DOPC in chloroform was dried to a film and rehydrated with 1 mL of 1 mM HPTS and 150 mM KCl (pH=8), and extruded in the same way. Un-encapsulated external dye was removed using a size exclusion chromatography (SEC) column packed with Sepharose CL-6B resin (Fig. 3.7). Proton transport kinetics were obtained by monitoring the HPTS dye (ex. 450nm, em. 514nm) using a FluoroMax-4 Spectrofluorometer (Horiba Inc.). For kinetic measurements, 2 mL of 150 mM KCl pH 3 solutions were placed into the fluorometer quartz cuvette. After the start of the measurement, 0.2 mL CNT-containing vesicle sample (or 0.2 mL control vesicle sample) was added to the cuvette and data were taken while stirring the solution continuously with a magnetic stirrer bar.

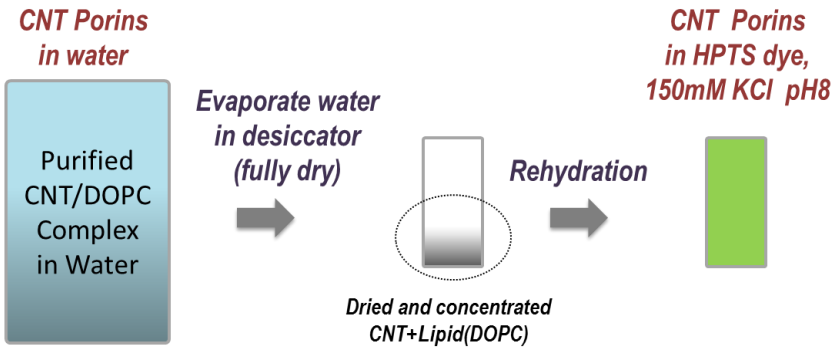

Figure 3.6 Highly concentrated CNT porins (CNT/DOPC complex) and exchange of suspension solution

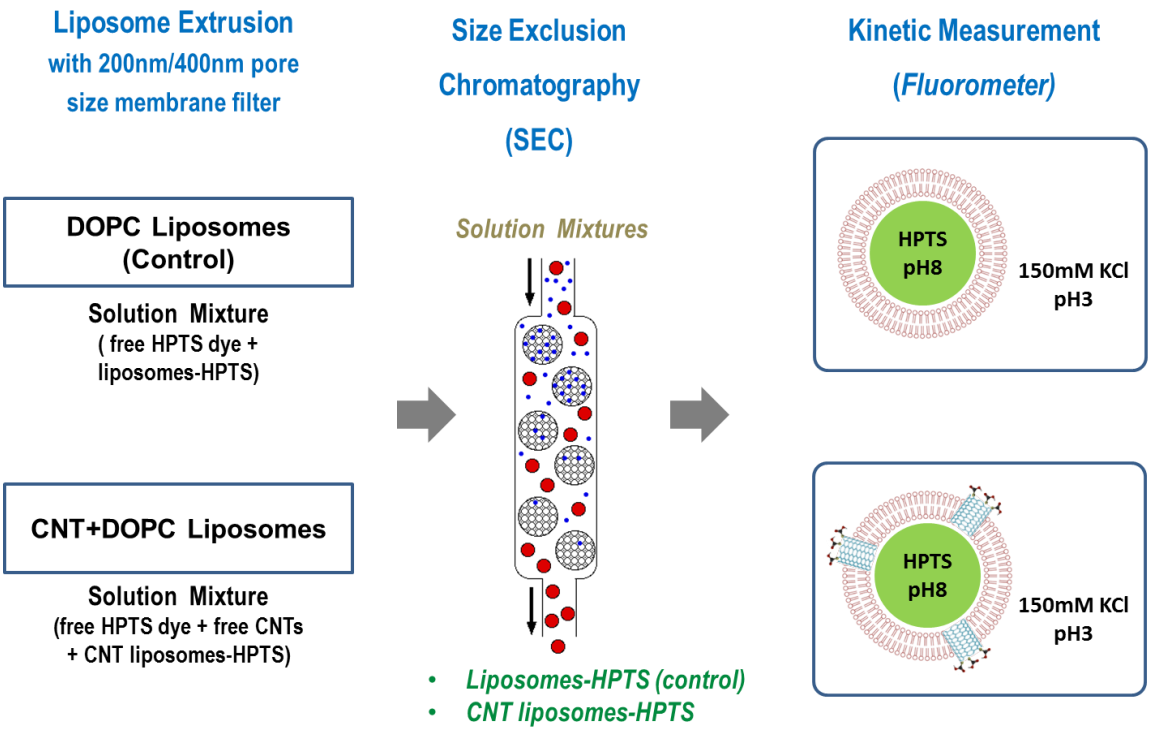

Figure 3.7 Schematic of sample preparation and proton transport measurement

The decay of the HPTS fluorescence (Fig. 3.8) indicated that once we established the proton gradient, the protons were transported into the vesicle lumen space. In the absence of the CNT porins, the fluorescence decay followed single-exponential kinetics with a characteristic time of 187 s, clearly indicating the existence of a single pathway for protons to enter the vesicle lumen by diffusing through the lipid bilayer. After we inserted the CNT porins into the vesicle walls we did not observe any leakage of the HPTS dye from the vesicles, indicating that the CNT porins were impermeable to the HPTS. However, the proton transport experiments with these vesicles produced much faster fluorescence decay (Fig. 3.8). Significantly, the decay kinetics no longer followed a single-exponent form, but instead represented a sum of two exponential terms, with the first term matching the 187 s timescale obtained in a control experiment, and the second term having a much faster characteristic time of 35 s (Fig. 3.8, inset). This result confirms that the addition of CNT pores to the vesicle wall formed a second pathway for protons to enter the vesicle inner space.

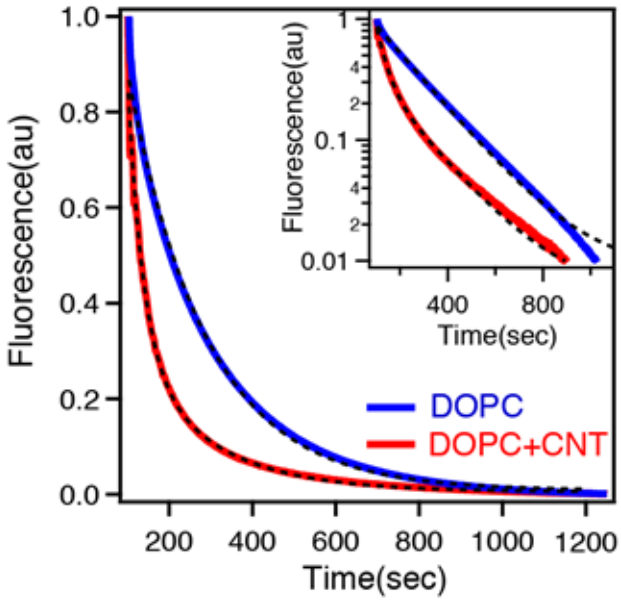

Figure 3.8 Proton transport properties of CNT porins. Time trace of the fluorescence intensity of the 1-hydroxypyrene-3,6,8-trisulfonate (HPTS) dye trapped in the vesicle lumen space at pH=8.0 after the vesicles were added to the solution at pH=3.0.

CNT pores in lipid membrane of CNT liposomes speeds up the proton transport (Fig. 3.8 blue) significantly over the control experiment where no CNT pores were present(red). The fluorescence intensity change over time follows a double exponential decay function.

$$\frac{I}{I_o} = A \cdot e^{(-k_1 t)} + (1 - A)e^{(-k_2 t)}$$

where I_0 is the fluorescence intensity at time zero, A is the pre-exponential factor and $k_1$and k_2 are rate constants. Using the average rate constant $\langle k \rangle = (Ak_1 + (1 - A)k_2)$ or the initial rage constant k_0 and the surface area of liposome, S_v and volume of the liposome, V_i , the apparent proton permeability coefficient P using the following relation, $\mathrm{k} = \mathrm{S} \times P/V_i$. The calculated values of permeability for DOPC vesicles and CNT embedded liposomes were $1.2 \times 10^{-8} cm/s$ and $7.6 \times 10^{-8} cm/s$ respectively. The proton permeability comparison of DOPC liposomes and CNT-containing liposomes exhibits that lipid bilayer packing provides a barrier for ion transport and is the major contributor of low proton permeability

3.3.3 Osmotic transport of water and small molecules through CNT porins

Osmotic stress study using artificial vesicles is a convenient way to induce transport across the lipid bilayer. Our liposome model system is illustrated in Fig. 3.9, which shows experimental concept about the movement of water by osmotic force in DOPC liposome with CNTs and without CNTs. In case of pure DOPC liposome as a control, higher solute concentration outside liposome will create an osmotic difference across lipid bilayer. The osmotic force drives water flow from water inside liposome lumen to the outside solute solution compartment. In the case of CNT-containing liposome, CNT nanopores permit transport water molecules between the two compartments inside and outside the membrane of the liposome. This transport through CNT pores equalizes osmotic gradient and there would not be any significant change in size.

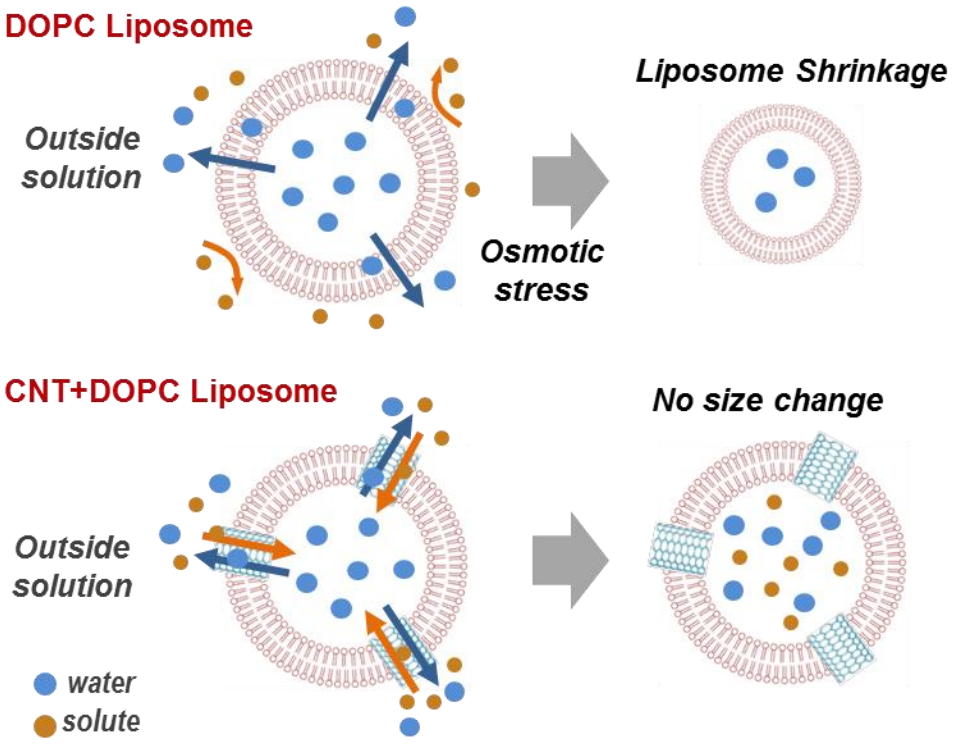

Figure 3.9 Illustration of the response of liposome with and without CNT channels to transmembrane osmotic gradient

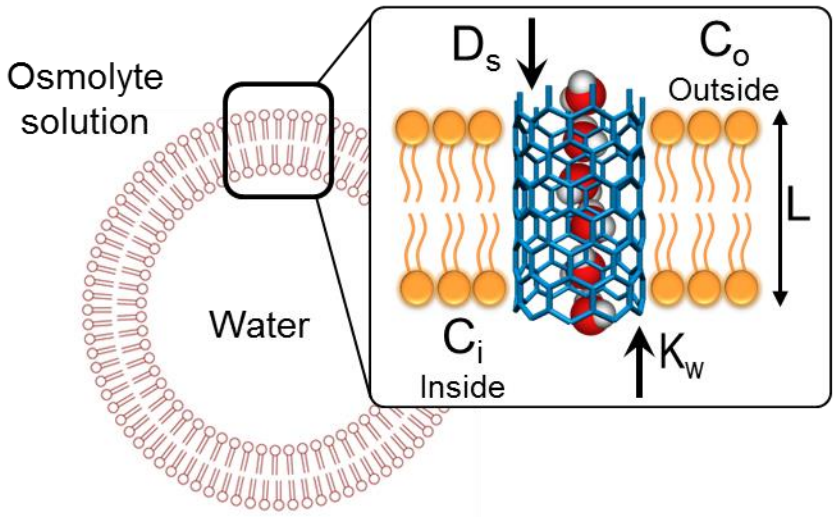

Figure 3.10 Schematic of the parameters used to describe osmotic pressure-driven water transport in vesicles containing CNT pore channels

Figure 3.12 shows schematic of simple analysis model for water transport through CNT channels in lipid vesicles driven by concentration gradient. In our experiment we induced water transport by placing vesicles filled with pure water and containing the CNT pores into a low concentration osmolyte solution. The osmotic pressure difference between the solutions outside and inside the vesicle drives some of the water out of the vesicle, causing the vesicle to shrink. At the same time the osmolyte diffuses into the vesicle through the CNT pores and reduces the driving force. The system reaches a steady state when the osmolyte diffusion equalizes the osmotic pressure between the inner compartment of the vesicle and the outer solution.

Consider a vesicle of initial volume $V_{0,}$ filled with water; the osmolyte concentration in the inner compartment, $C_i(t=0)$, is zero. The vesicle contains N_p pores of radius r and length L. We then place this vesicle into the osmolyte solution of concentration C_0. The volume of the outer solution is much larger than the volume of the vesicles, thus the concentration C_0 always remains constant. The diffusion of the osmolyte through the CNT pores follows Fick's Law:

$$J_s = -N_p D_s \cdot \frac{C_i - C_0}{L} \qquad \text{(Eq.1)}$$

where D_s is the effective osmolyte diffusion coefficient through the CNT pore. D_s generally depends on the size of the molecule and the rejection coefficient of the CNT pore channel. In all our experiments the *maximum* vesicle size change that we observed was relatively small, so we can simplify this model by assuming the following equation for osmolyte diffusion:

$$\frac{dC_i}{dt} = \frac{J_s}{V_0} = -\frac{D_s}{V_0 L} \cdot (C_i - C_0) = -k_s \cdot (C_i - C_0) \qquad \text{(Eq. 2)}$$

This equation, which describes the evolution of osmolyte concentration inside the vesicle, has a solution of the form:

$$C_i(t) = C_0 \cdot (1 - e^{-k_s t}) \qquad \text{(Eq. 3)}$$

The osmotically-driven transport of water can be described using Darcy's Law as:

$$\frac{dV}{dt} = -\frac{k_w N_p \pi r^2}{\mu L} \Delta\pi_{osm} \qquad \text{(Eq. 4)}$$

where k_w is the water permeability of the CNT pores, μ is water viscosity, and $\Delta\pi_{osm}$ is the difference in the osmotic pressure between the outer and inner vesicle space, that is equal to: $\Delta\pi_{osm} = iRT(C_0 - C_i)$, where i is the van't Hoff factor. We then can re-write this equation as:

$$\frac{dV}{dt} = \frac{-k_w N_p \pi r^2 iRt}{\mu L} \cdot (C_0 - C_i) = -K_W \cdot (C_0 - C_i) \qquad \text{(Eq. 5)}$$

Substituting the expression for $C_i(t)$ and integrating this equation gives us the final expression for the vesicle volume evolution with time:

$$V(t) = V_0 - \frac{K_W}{k_s}(1 - e^{-k_s t}) \qquad \text{(Eq. 6)}$$

Then, the steady-state volume change that we measure in the experiment is given by a simple expression:

$$\frac{V_\infty}{V_0} = 1 - \frac{K_W}{k_s} \cdot \frac{C_0}{V_0} = 1 - \frac{iRT\pi r^2}{\mu} \cdot \frac{k_w}{D_s} \cdot C_0 \qquad \text{(Eq. 7)}$$

The CNT/DOPC complex (CNT porins) supernatant was prepared and characterized by the same recipe and method described in Chapter 2. For osmotic pressure-induced vesicle size change measurement, 0.2 mL of 10 mg/mL DOPC solution in chloroform were added to a vial and dried into a film using a Biotage V-10 evaporator. 1mL of CNTs/DOPC complex suspension was then added to the vial and extruded through polycarbonate filter membranes with 200 nm diameter pores using a hand-held extrusion device (mini-extruder, Avanti Polar Lipids) to form CNT-containing vesicles as described in the previous Chapter. A control sample was prepared in a similar way, except that 0.3 mL of the DOPC solution was used to prepare a lipid film and water was added instead of CNT/DOPC mixture. The hydrodynamic radius of the vesicles was measured using a dynamic light scattering (DLS) setup (Zetasizer, Malvern Instruments). In a typical measurement we mixed 10 μL of the vesicle solution and 70 μL of a salt solution such as KCl, KNO_3, K_2SO_4 or a sugar solution such as sucrose and dextran of known concentration, and placed an aliquot into a 70 μL volume-cuvette cell. To reduce measurement uncertainty, each data point represents an average of at least four individual measurements.

Osmotically-driven water and ion transport measurements reveal further information about the nature of the transport through the CNT porins. When lipid vesicles filled with pure water were placed into diluted KCl, KNO_3 and K_2SO_4 solution respectively, the difference in the osmotic pressure between the inner and outer space of the vesicles drove some of the water out of the vesicles and caused them to shrink. It was important to use an electrolyte concentration below the 15 mM range where the osmotic gradients were relatively mild and did not cause catastrophic rupture of the vesicles. When the vesicles did not contain CNT porins, we detected only minimal (<2.3 %) vesicle size change (Fig. 3.11) regardless of the ionic strength of the solution outside the vesicles, indicating that slow diffusion of water and ions across the lipid membrane were slowly dissipating the osmotic gradient. In contrast, vesicles incorporating the CNT porins quickly shrank up to 25%. Moreover, the degree of shrinkage showed a strong dependence on the ionic strength of the solution outside the vesicles (Fig. 3.11). At low ionic strength the vesicles containing CNT porins exhibited the highest shrinkage, and at high ionic strength the shrinkage reduced dramatically and began to approach the values measured for the control samples.

Osmotically-induced transport in this system involves a combination of water being forced out of the vesicles through the CNT porins and reverse salt flux entering into the vesicle lumen. A simple analysis (Fig. 3.10) shows that shrinkage should be proportional to the rate of the water transport through the pores and inversely proportional to the rate of salt leakage back into the vesicles. It is unlikely that ionic strength of the solution influences the water transport rate through the CNT porins; instead, we propose that ionic strength has a significant effect on the ion permeability. Such behavior is easy to rationalize if we consider that for the experimental conditions (pH=7), the carboxylic acid groups at the CNT rim are ionized and the ring of negative charges at the CNT pore entrance creates an electrostatic barrier for the ion passage. Under these conditions, the ion leakage into the vesicle lumen is slow and the osmotic transport of water can cause significant shrinkage of the vesicles. At higher ionic

strength, the charges are screened, and the barrier for ion passage through the CNT pore drops significantly. Then the osmotic pressure gradient equalizes rather quickly, and thus cannot cause significant vesicle shrinkage. Indeed, the transition from high to low ion rejection in our measurements occurs at the same Debye length range (6-7 nm) that we previously observed for bulk CNT membranes[69], confirming that the observed effects are closely related to the ion diffusion through the CNT pores. Similar trend was detected for 2:1 salt solution. The interesting observation is that the change in vesicle size occurs quickly with decreasing Debye screening length for a 2:1 than a 1:1 salt solution in Fig. 3.11. It means that the decay of SO_4^{2-} exclusion is faster than Cl^- and NO_3^-. This ion rejection trend can be explained by the Donnan rejection mechanism. Donna model prediction accounts for the experimentally observed ion rejection in charged pores[15]

$$R = 1 - \frac{c_i^m}{c_i} = 1 - \left(\frac{|z_i|c_i}{|z_i|c_i^m + c_x^m}\right)^{|z_i/z_j|} \qquad (2)$$

When the salt concentration increases, the Debye screening length goes close to CNT pore size and permeation of ions will increase due to reduced electrostatic potential. Our experimentally observed data in figure 4a correspond to the trend calculated by Donna theory

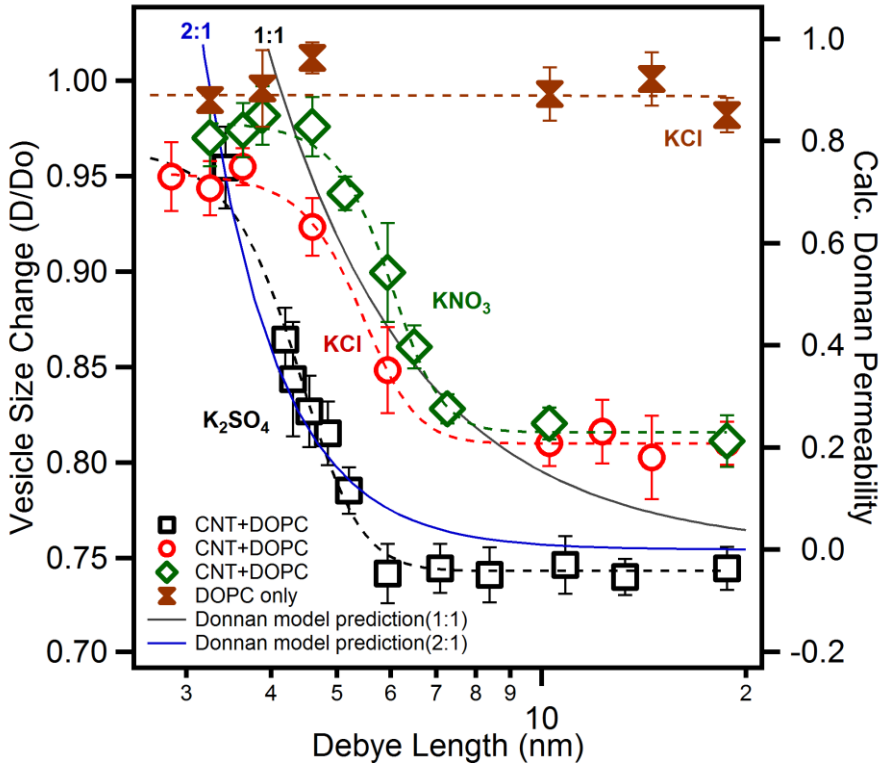

Figure 3.11 Transport of charged species with different anions through CNT channels. (a) Dependence of vesicle size change of charged molecules on solution concentration, and Donna rejection model

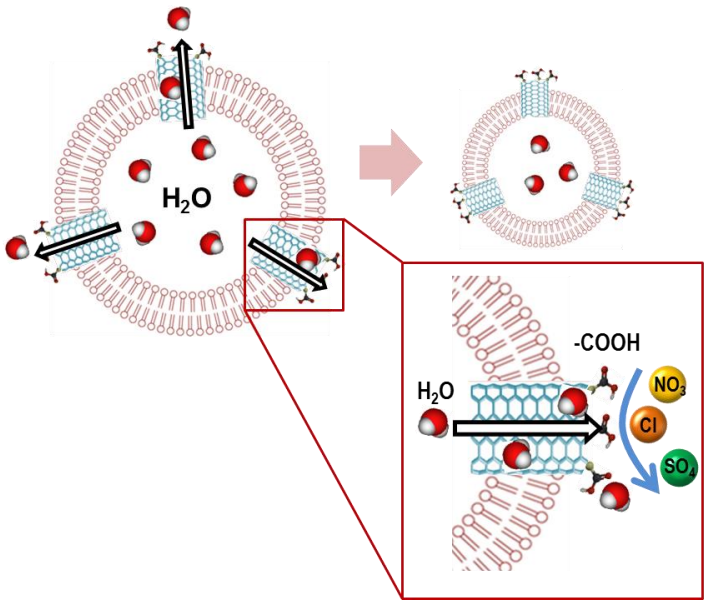

Figure 3.12 Cross sectional schematic of ion rejection in CNT-containing liposome and CNT tips with carboxylic groups

Transport properties of uncharged molecules through CNT porins were investigated. Previous theoretical and experimental studies report the results on fast water transport across CNT membranes. Lipid bilayer is impermeable to uncharged molecules, sucrose and dextran. Osmotic gradient-driven water transport experiment using those membrane-impermeant solutes reveals information about the molecular movement through CNT porins. As can be seen in Fig. 3.13, both sucrose and dextran are too large to pass through the lipid membrane and the only passage of molecular transport is through transmembrane CNT porins. Our observation would suggest that based on the approximate hydrodynamic radius of dextran (Sigma-Aldrich, molecular weight 342.30) with 2.4 nm[70] and that of sucrose (Sigma-Aldrich, molecular weight 12,000) with 0.46 nm[71] as shown in Fig. 3.13, only sucrose molecules pass through CNT pore with about 1.5nm diameter.

Sucrose molecules move water from the inside compartment of the vesicle to the outside solute medium through nanopores so that the gradient across the membrane releases. But in case of placing CNT liposomes into dextran solution, since the hydrodynamic radius of dextran is much larger than CNT pore radius we rationalize that impermeant dextran solute would not establish equilibrium between water compartment and solute medium causing the vesicle size to shrink. Our rationale is experimentally demonstrated by putting lipid vesicles into hypertonic solution (sucrose and dextran). Figure 3a shows the experiment results with vesicle size change measured by dynamic light scattering (DLS). Green empty markers show that CNT-containing liposomes in sucrose solution do not change in vesicle size. This indicates sucrose molecule pass through CNT porins and osmotic gradient is equalized. Bright orange empty markers show that the size of vesicles changes to decrease with increasing concentration of

dextran. This means that the solutes cannot pass through CNT porins so that it makes solution hypertonic relative to the inside of vesicle. As a result, water inside of the vesicle moves out of the vesicle via osmotic differential between interior water and external solution of vesicles so that the vesicle shrinks in size. For the liposomes without CNT porins, the size of those decreases with increasing concentration since lipid bilayer is not permeable to both uncharged sucrose and dextran molecules.

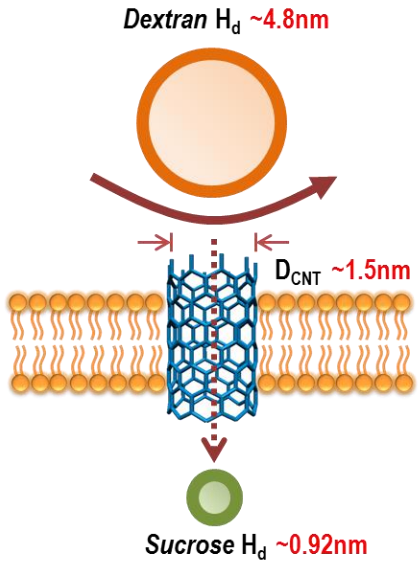

Figure 3.13 Schematic of CNT pore in lipid bilayer and hydrodynamic radius of dextran and sucrose

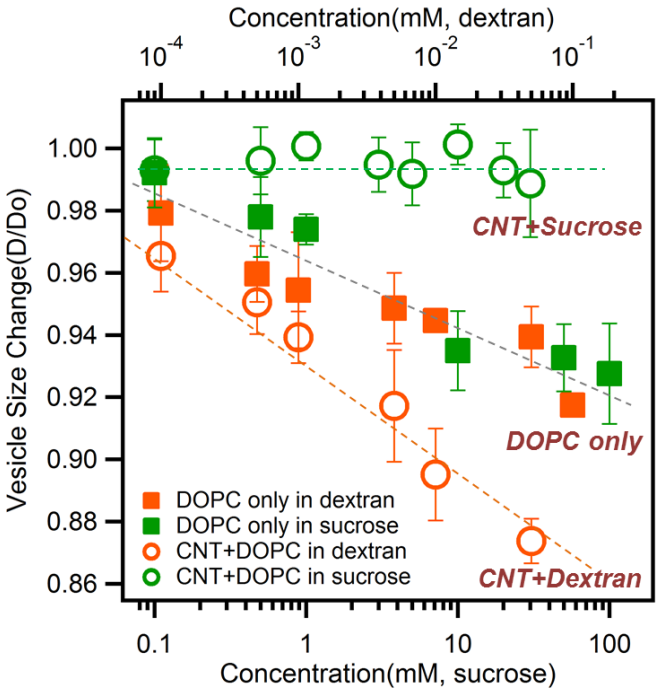

Figure 3.14 Transport of uncharged species through CNT channels. (a) Plot of vesicle size change in different solutions. All the vesicle lumen contains pure water only

The transport properties of cations in negatively charged CNT pores were tested. It is likely that the negatively CNT porins are selective toward cations with different hydrated radius. In Fig. 3.15, highest shrinkage in vesicle size at electrolyte solutions with same chloride anion shows the trend proportional to hydrated ion radius size. Interestingly, contrasting with Na^+, K^+ and Li^+, Cs^+ exhibits very small shrinkage in vesicle size at lower ionic strength. This indicates that cesium salt exclusion is very low relatively compared to those of sodium, potassium and lithium. Li^+, Na^+ and K^+ with larger hydrated radius can be excluded by the ring of negative charge at the CNT mouth, but Cs^+ with smaller radius enter the CNT pore more quickly than other cations. This trend can be explained by that aqueous cesium ion has low hydration energy and does not hold a bound hydration layer[72].

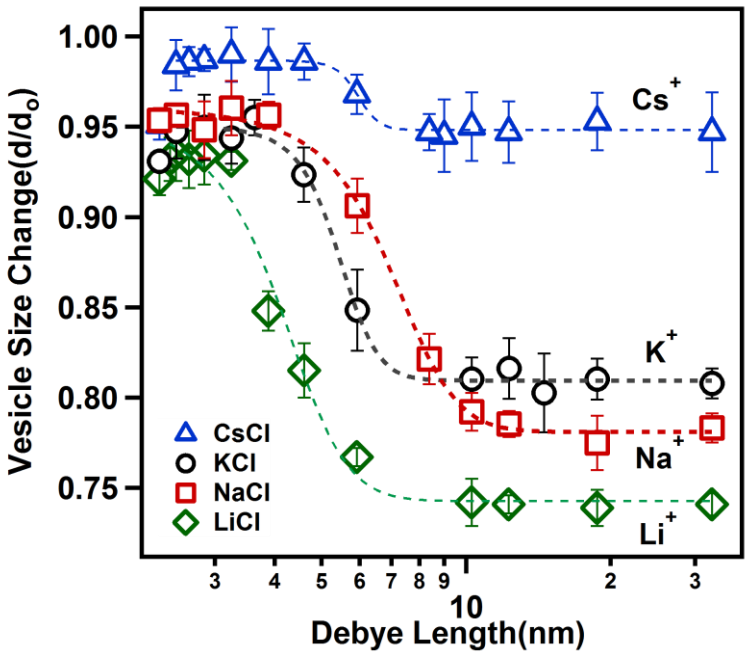

Figure 3.15 Transport of charged species with different cations through CNT channels. Effect of variations in hydrated radius of cations on osmotic-driven water and ion transport through CNT pores

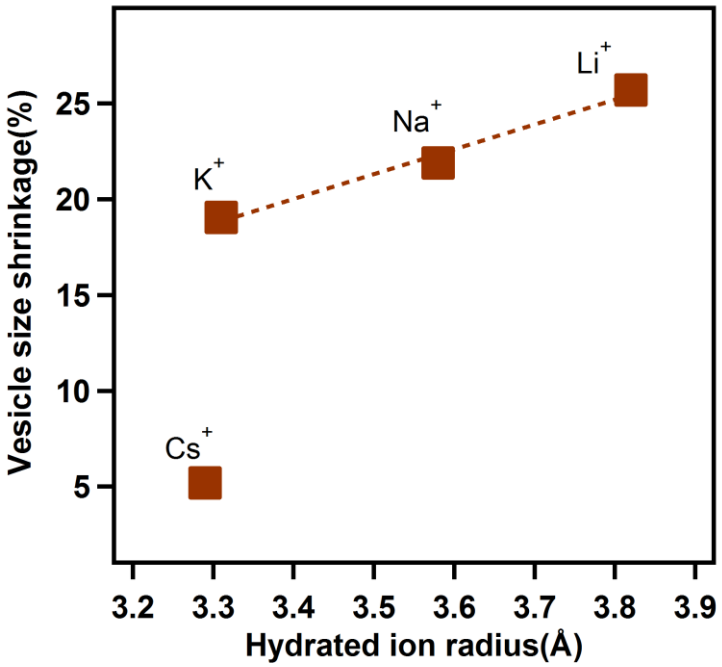

Figure 3.16 Vesicle shrinkage of CNT liposome in the solution *vs.* hydrated ion radii of different cations.

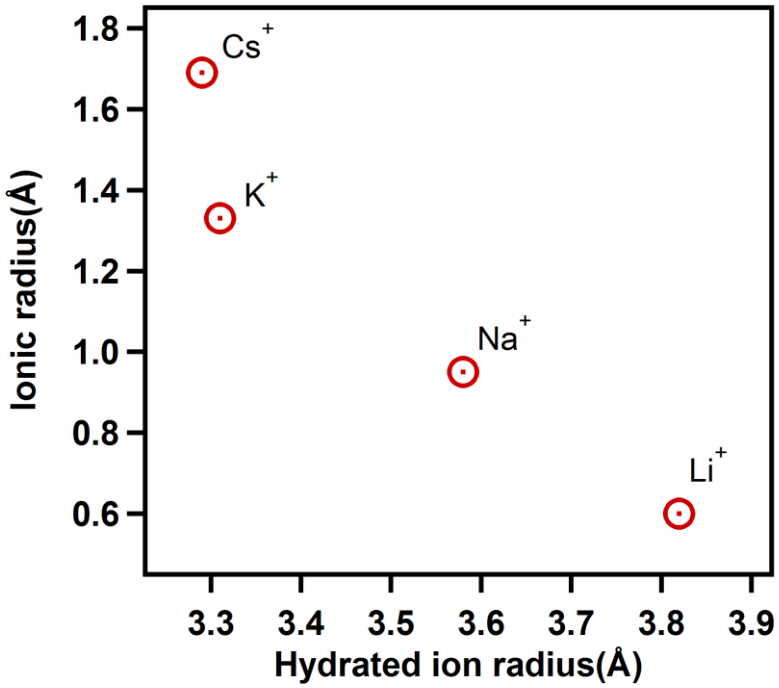

Figure 3.17 Variations of hydrated radius of ions

3.4 Stochastic Transport and Gating in CNT Porins in Lipid Membranes

3.4.1 Stochastic transport and gating in CNT porins

Previous chapters described the preparation of carbon nanotube porins, their incorporation into lipid membranes, and their proton transport and ion rejection properties from bulk measurement studies. In this chapter, additional information is given about the CNT porin geometry and transport characteristics from single pore channel conductance measurement of the ion transport through individual CNT porins.

Electrophoretic transport measurements for individual CNT porins also revealed important and unexpected characteristics of these objects. For these measurements a planar lipid bilayer setup was used, in which a small patch of the lipid bilayer separated two solution chambers.

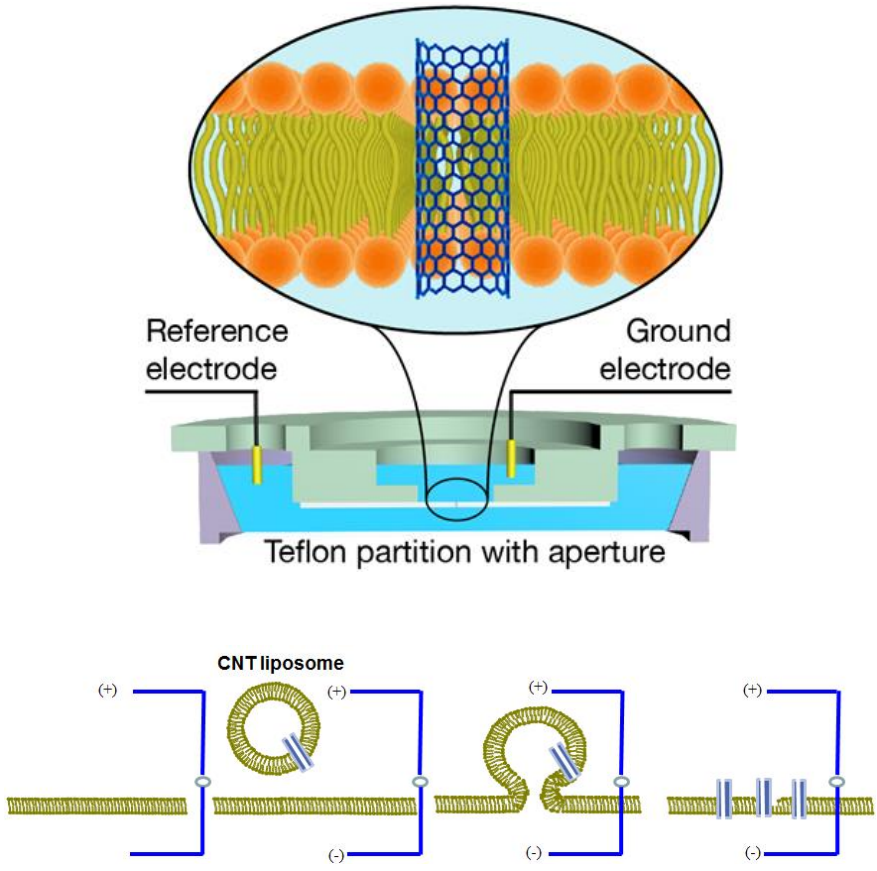

Figure 3.18 Schematic of the setup for single-channel recording of CNT porin conductance and CNT porin incorporation. Two chambers are separated by a Teflon partition that contains a ca. 200 µm aperture with a painted-over lipid bilayer membrane

The above schematic shows the setup for single pore channel conductance measurement. A supported lipid bilayer was formed over a 200 µm diameter aperture in a Teflon film partition (Eastern Scientific LLC) using a painting technique. Briefly, two small solution chambers (Eastern Scientific LLC) were cleaned by subsequently washing with detergent, ethanol, and water. A partition with an aperture was attached to the bottom of the *cis*-chamber using vacuum grease. A 100 µL Hamilton glass syringe was used to place 50 µL of hexane containing 20 mg/mL DOPC onto both sides of the aperture, and allowed to dry for 10 min. The *cis*-chamber was then placed onto the top of the *trans*-chamber to form two separate compartments. The *trans*- and *cis*-chambers were filled with 2 mL and 0.2 mL conducting buffer (KCl or NaCl with 5 mM HEPES, pH 7.4), respectively. A ground Ag/AgCl electrode was placed into the *trans*-compartment, and a reference electrode Ag/AgCl was placed into the *cis*- compartment. During the measurement a 2 µL solution of DOPC vesicles containing CNT pores was added to the *cis*-chamber.

For transport measurements, a holding potential of 50 mV to 200 mV was applied to the reference electrode, and trans-membrane current signal was recorded by a low-current measurement setup, which consisted of an Axopatch 200B patch clamp amplifier and an Axon DigiData 1322A analog-digital converter (Axon Instruments) connected to a computer system running Clampex 10.3 software (Axon Instruments). Traces were acquired at a sampling frequency of 10 KHz – 100 KHz and were low band-pass filtered at a frequency of 5 kHz or 1 KHz to increase signal-to-noise ratio. The data was analyzed and exported using PClamp 10.3 software (Axon Instrument), and further analyzed using Origin Pro 8.0 and Igor Pro 6.31. As a positive control the conductance of Gramicidin channels was measured in the following procedure. 0.1 mg Gramicidin A was incubated with 200 µL of the DOPC liposome solution (150 mM KCL, 4mg/mL lipid concentration, pH 7.4). After a lipid bilayer was formed over the testing setup aperture (in the presence of 1 M KCl solution in both chambers), 2 µL of gramicidin A/vesicle solution was added into the *cis*-chamber and the conductance traces were recorded using a transmembrane potential of 75 mV. The conductance measured for gramicidin was 0.058 ± 0.008 nS, which is close to the reported values 0.0459 ± 0.005 pS.

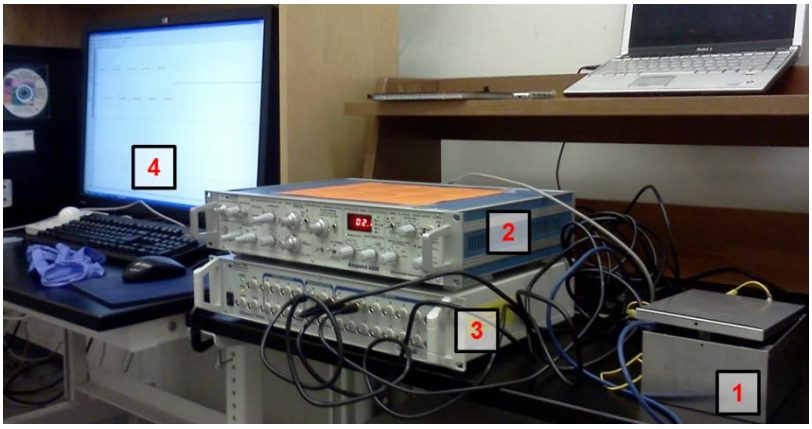

Figure 3.19 Photograph of assembled patch-clamp system. 1. Headstage and recording chamber. 2. Amplifier (Axon Axopatch 200B) 3. Digitizer (Axon Digidata 1440a). 4.Software (PClamp 10.3)

In the absence of the CNT porins, the DOPC lipid bilayer formed a well-insulated seal and the current recording produced flat featureless traces (Fig. 3.20, control trace). When we placed liposomes containing CNT porins to the *cis*- chamber, the bilayer conductance increased following a series of characteristic amplitude jumps (Fig. 3.20). Each of these jumps corresponded to an incorporation of a CNT porin into the membrane and opening of the ion conductance pathway across the lipid bilayer. The frequency of these incorporation events varied, with traces sometimes showing well-separated events, and sometimes showing multiple steps corresponding to a relatively quick succession of incorporation events (Fig. 3.20). The conductance value histogram of 236 individual CNT incorporation events (Fig. 3.21) displays several interesting features. Solid blue line corresponds to the fit of the data to a distribution expected for multiple channel incorporation where the position and width of the second peak are determined form the position, μ, and width, σ, of the first peak as 2μ and $\sqrt{2}\,\sigma$. First, the conductance values show clear evidence of quantization with the first peak corresponding to the 0.63±0.12 nS value and subsequent peaks at exactly double that value. Remarkably, both peaks can be fit with a single pair of values for the first peak position and width (Fig. 3.21).

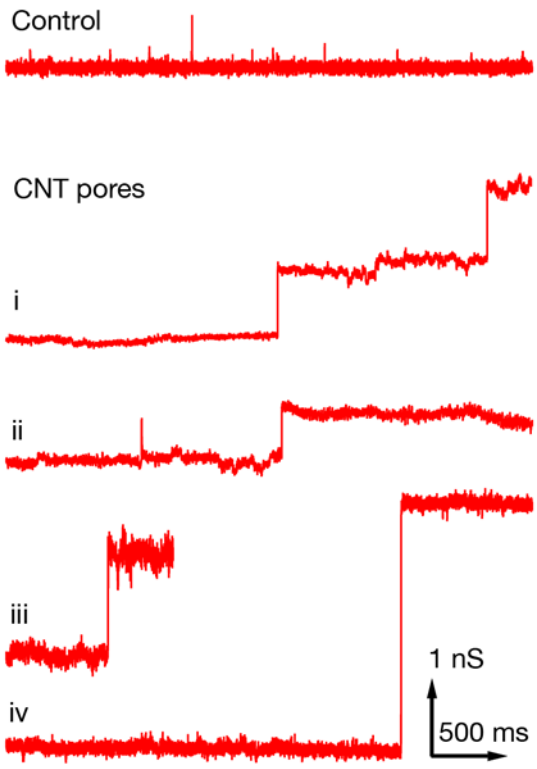

Figure 3.20 Conductance traces showing individual CNT channels incorporation into lipid bialyer. For the control experiment no CNTs were added to the chambers

The data argue strongly that the initial peak corresponds to the incorporation of a single CNT porin, and that the second peak corresponds to the incorporation of two CNT porins. Occasionally, we recorded conductance jumps at higher multiples of the single pore conductance value, but the frequency of those events was low. An interesting conclusion from these data is that despite the presence of a relatively wide distribution of nanotube sizes in the purified short CNT mixture, the conductance value for a single CNT channel is extremely well defined. Cryo-TEM images argue strongly against the possibility that only a narrow subset of short nanotubes is capable of stable incorporation into the lipid membrane. Thus we have to conclude that the conductance of a short CNT is a relatively weak function of the CNT length and instead is determined mainly by the interfacial resistances of the CNT ends[73]. Interestingly, the 0.63 nS conductance of a single CNT porin is close to a 0.68 nS conductance of a α-haemolysin channel[74], which has a 10 nm pore with width that varies from 1.4 nm in the neck region to 4.6 nm in the vestibule region[75].

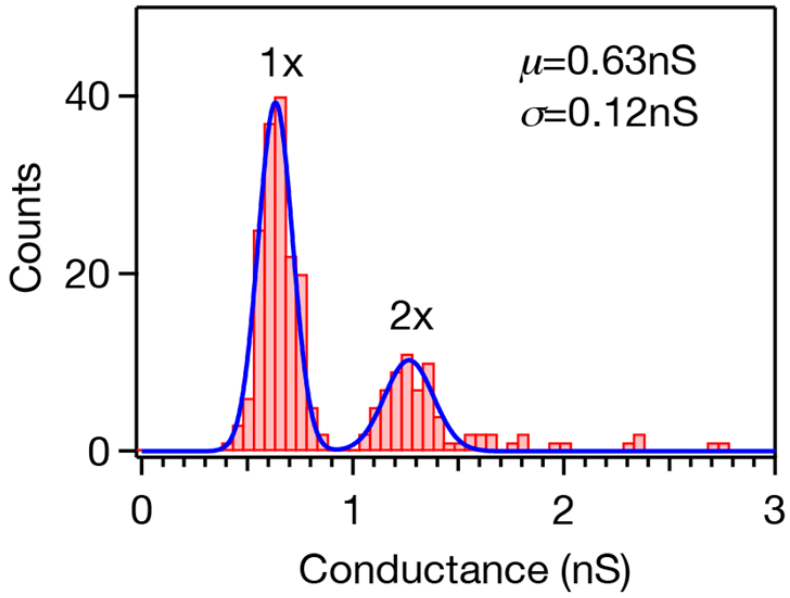

Figure 3.21 Histogram of conductance values measured for CNT channel incorporation events showing distinct clustering at the single and double values of individual CNT channel conductance

In our measurements, pore conductance scaled linearly with the salt concentration in the 0.5M - 2M range at neutral pH, strongly suggesting that the dominant conductance mechanism through the CNT porin is ionic. Moreover, when we measured the conductance of the CNT porin at pH=2 we have obtained a similar pattern in the distribution of conductance values (Fig. 3.21), although the conductance of a single CNT porin was reduced almost by a factor of 2 from 0.63 nS to 0.33 nS. This observation rules out proton conductivity as the dominant current carrying mechanism in these pores.

About 30% of the CNT porin conductance traces exhibited more complicated dynamics after insertion. These traces resembled stochastic opening and closing where the conductance signal oscillated between two distinct states (Fig. 3.22, traces i, ii). On rare occasions we have also observed that the current fluctuated between three distinct states (Fig. 3.22, trace iii), indicating that the lipid bilayer contained two independent pores undergoing stochastic opening and closing. The conductance values of the "on" and "off" states were very reproducible for any given trace, as evidenced by the presence of clear peaks in the histograms of the trace amplitude signal (Fig. 3.22); thus it was unlikely that they originate from simultaneous insertion and removal of multiple channels. The average time the channel spent in the "on" and "off" states was approximately equal (τ_{ON}/τ_{OFF}=1.1±0.8 at 100mV bias and 2M KCl), indicating that the free energy difference between these two states was small.

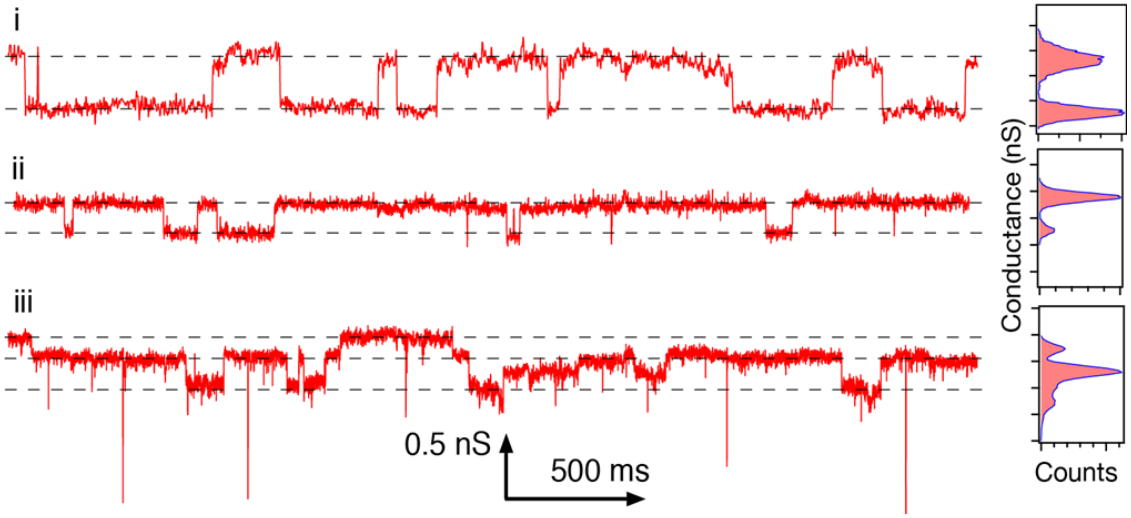

Figure 3.22 Conductance traces showing stochastic "gating" transitions in the CNT channels. Traces *i* and *ii* show transitions produced by a single channel, trace *iii* results from transitions in tow independent channels. The insets show normalized histograms of the conductance values for the traces. Total range of the vertical axis on each histogram plot is 1nS

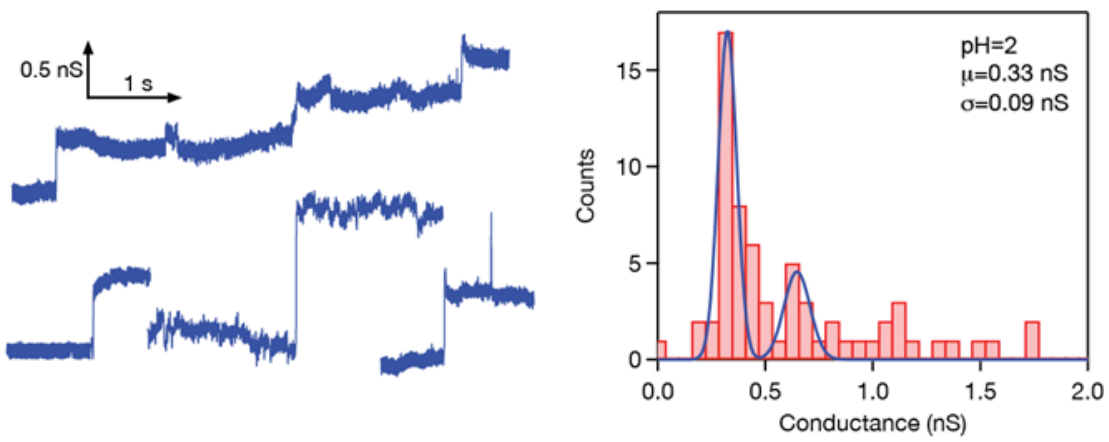

Figure 3.23 Single CNT channel conductance at pH=2. Representative conductance trace showing individual CNT channel incorporation at pH=2 (left) and histogram of conductance values measured for 66 individual CNT channel incorporation events (right).

MD simulations of pore insertion into lipid bilayers indicate that rapid removal and re-insertion of the CNT porin from the bilayer cannot cause these oscillations[28]. The ionic nature of the conductance in CNT porins argues against the possibility that the oscillations originate from the ion blocking of the proton-based current as reported by Strano and co-workers for macroscopically-long CNT channels[26]. Since our test solutions contained only monovalent ions (K^+, and Cl^-) we can also rule out transient blocking by nanoprecipitation[76]. The blockades caused by nanoprecipitation also have a characteristic triangular shape that is different from the rectangular shape blockades that we observed. Another possible cause could be spontaneous wetting/dewetting transitions in hydrophobic nanopores[77]. However, such transitions should produce a very clear zero-conductance "off" state; in contrast in our system the conductance in the "off" state was typically reduced by a value of 0.2-0.4 nS, which was considerably smaller than the ca. 0.63 nS conductance of a single CNT porin at the experimental conditions. These observations suggest that CNT porins remain filled with water all the time, also in agreement with MD simulations that show complete filling of CNTs with water[78].

Instead, conductance oscillations in our pores are remarkably similar to the stochastic "gating" behavior that is well-known for biological ion channels[1]. These oscillations are typically attributed to reversible transitions between several conformation states on the ion channel[79]. Unlike biological channels, CNT porins contain no movable peptide chains and the whole pore structure is extremely rigid, which excludes a mechanism based on conformational transitions. Instead, these oscillations could represent a spontaneous transition between ionic penetration and ionic exclusion states. Palmeri and co-workers recently used a variational field theory model to predict such transition for ionic solutions in very narrow nanopores[80]. Their model predicts that weakly charged or neutral nanopores embedded in a low dielectric permittivity membrane can exist in two states: a low conductivity ionic exclusion state where the dielectric repulsion discourages the ion from entering the nanopore, and an ionic penetration state where this dielectric repulsion is screened by an increased concentration of the ions. The calculation showed that while this effect is robust, it only exists in the

nanopores with diameters less than 2 nm and only in neutral or very weakly charged nanopores. While some evidence for the existence of a similar transitions has been reported for nanogaps formed by patching a glass pipette to a structured elastomer surface[81], an uncharged inner surface of the 1.5 nm diameter CNT porin embedded in a low dielectric permittivity hydrocarbon interior of the lipid bilayer does represent an ideal experimental system for observing this transition. Moreover, since we observed this transition in a pore embedded in a free-standing lipid membrane our results argue that this ionic penetration-exclusion transition could represents one of the mechanisms of stochastic gating in biological ion channels.

3.4.2 DNA translocation through CNT ion channels

The ability of the CNT pores to translocate longer molecules, such as DNA was tested. Branton and co-workers first reported that electrophoretic translocation of single-stranded DNA through an α-haemolysin channel produces transient blockades of electrophoretic current through the pore[82]. Because the width of the α-haemolysin channel neck is similar to the width of the CNT porin we expected to see similar behavior in our system. For the measurement of individual single-stranded DNA translocation through CNT porins, a similar setup and sample preparation technique to that described in the preceding chapter. ssDNA oligonucleotide (5'-/5Phos/GCG GCC GCT ACT AGT CTT ACC GCC ACC CAG AGG GCC ATA ACG GGT ACG GTA TTG GCT TAC ACG GTT ACG CAG ACG CTG TAC -3', 81 nt length) was pre-mixed into the solution (1 M KCl, pH 7.4) in the *cis*-chamber to a final concentration of 100 pM. After a planar lipid bilayer was formed in the aperture, 2 µL of CNT-containing vesicles (prepared as described in the previous sections) was gently added into the solution in the *cis*-chamber by pipette, without rupturing the bilayer membrane. A holding or ramping potential of 50 mV maximum amplitude was applied across the bilayer. The data were collected as described in the previous section. For a control experiment we collected data using the same conditions and protocol, except that no ssDNA was added to the chambers. The raw data current traces were analyzed using PClamp 10.3. Overall, over 800 translocation events from current traces of a total of 338 s duration were counted either manually or using custom-written software in Igor Pro (Wavemetrics, Inc.).

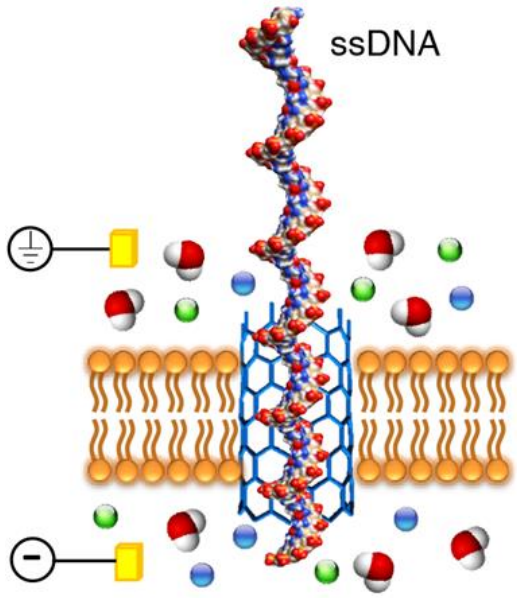

Figure 3.24 Schematic of the translocation of single-stranded DNA through a CNT pore in the lipid bilayer

When we added a short 81-nt long single-stranded DNA (ssDNA) oligomer to the trans-compartment of our system (Fig. 3.24) we saw repeated rapid current blockade events that corresponded to the translocations of individual ssDNA strands through the nanotube pore (Fig. 3.25). Statistical analysis of a large number of such events indicated that current blockade values followed a normal distribution centered at 0.48±0.08 nS (Fig. 3.26). This value is between the 0.8 nS blockades reported for pure α-haemolysin pores[82] and the 0.3 nS blockades reported by Dekker and co-workers for a hybrid pore structure in which an α-haemolysin pore was inserted into a larger solid state pore[58]. DNA translocation times followed a log-normal distribution (Fig. 3.26), which is also consistent with ssDNA transport through other nanopores. These data provide further confirmation that CNT porins form small-diameter transmembrane channels in the lipid bilayers. Note also that in these experiments we observed multiple DNA translocation events at the relatively low transmembrane bias of 50 mV. As a result, the translocation time distribution for the 81-mer ssDNA centers around a value of 53 ms, which is significantly longer than the *ca.* 0.3 ms time that was recorded for the translocation of 100-mer ssDNA through the α-haemolysin pore at 300 mV bias[58]. The ability to translocate macromolecules at low driving voltages could represent a potential advantage for stochastic sensing applications.

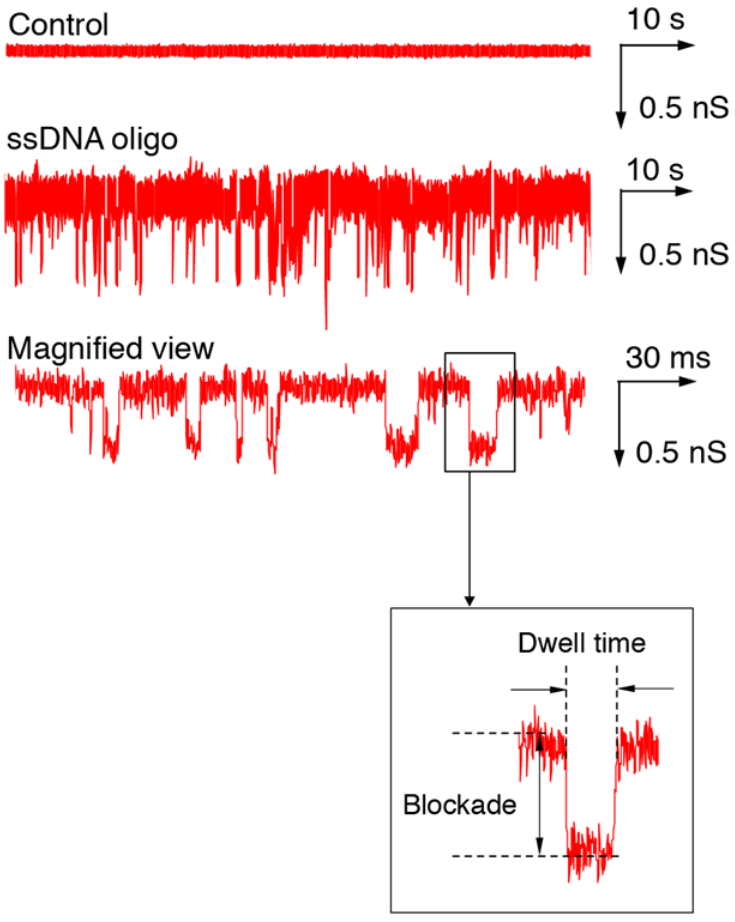

Figure 3.25 Current trace showing multiple transient blockades caused by DNA translocation through the CNT channel

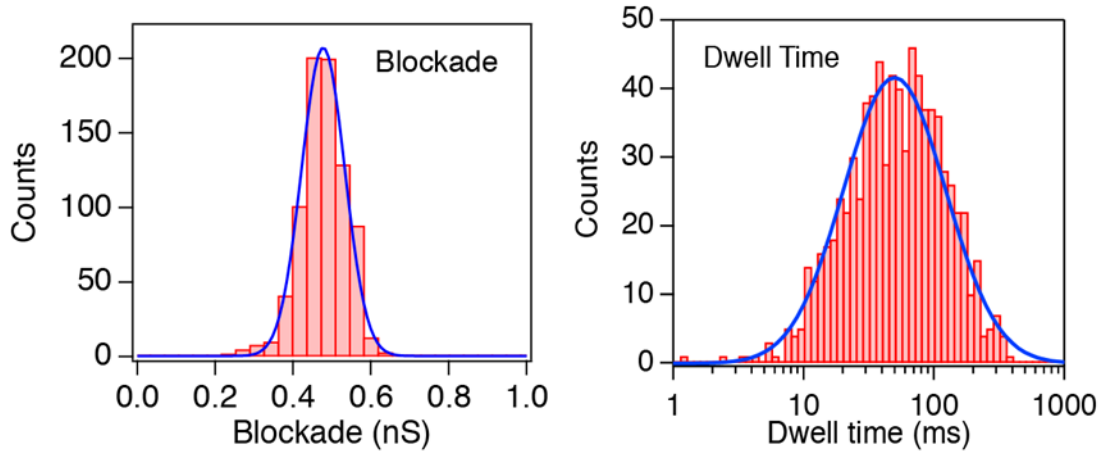

Figure 3.26 Histograms of the translocation blockade levels and duration obtained from more than 800 individual DNA translocation events

3.5 Conclusion

In this work, CNT porins can transport water, protons, small ions and reject large uncharged species. Ion rejection in CNT porins is determined by charge repulsion at the CNT rim. Charges in electrostatic screening can modulate ion rejection. From measurement of ion conductance of individual CNT porins, it is found that they can be incorporated into the membrane in a well-defined configuration with ion mobility values inside the pores closely resembling those of the biological ion channels. Also, electrophoretically driven translocation of individual single-stranded DNA molecules through the CNT porins produces well-defined ion current blockades even at low bias voltages. CNT porins open up important avenues for the development of biomimetic membrane transport and nanofluidics. Modification of CNT porins with synthetic "gates" could dramatically alter the channel selectivity and produce a diverse family of true artificial membrane channels. The inherent robustness of CNT porins against biological and chemical challenges could be a distinct advantage that would enable the use of these structures in synthetic cells, artificial kidneys, or in nanopore-based sequencing applications.

Chapter 4 Hybrid Bioelectronics with Membrane Proteins in Lipid Bilayer

4.1 Introduction

Biological systems interact with their environments by creating ion gradients, membrane electric potentials, or proton motive force to accomplish strikingly complex tasks on the nanometer length scale, such as energy harvesting, and whole organism replication. Most of this activity involves a vast arsenal of active and passive ion channels, membrane receptors and ion pumps that mediate complex and precise transport across biological membranes[83]. Despite the remarkable rate of progress exhibited by modern microelectronic devices, they still cannot compete with efficiency, precision, and flexibility of biological systems on the component level. On the flipside, the sophistication of these molecular machines provides an excellent opportunity to use them in hybrid bioelectronic devices where such a combination could deliver enhanced electronic functionality and seamless bi-directional interfaces between man-made and biological structures[84].

One-dimensional inorganic nanostructures, which have critical dimensions comparable to the sizes of biological molecules, form an excellent materials platform for building such integrated assemblies. Researchers already use silicon nanowire (SiNW) field effect transistors functionalized with molecular recognition sites in biosensing[85-87], nucleic acid detection[86], and drug development[88] applications. Recent works achieved an even higher level of integration by interfacing these transistor devices to neuronal activity[89], and cyborg tissue scaffolds[90]. Recently research in bionanoelectronics has been developing a platform for integration of membrane protein functionality into electronic devices based on a one-dimensional lipid bilayer device architecture. In these devices, the membrane proteins reside within the lipid bilayer that covers a nanowire channel of a SiNW field-effect transistor. This lipid bilayer performs several functions: it shields the nanowire from the solution species and serves as a native-like environment for membrane proteins that preserves their functionality, integrity, and even vectorality. Previous works showed that this architecture allows us to couple passive ion transport[91] and active ATP-driven ion transport to the electronic signaling[92].

In this work, I present a 1D bilayer device incorporating a bR proton pump that couples light-driven proton transport to a bioelectronic circuit output. Significantly, these devices also use a distinct biological mechanism for regulating their performance where co-assembly of protein channels and ionophores in the 1D bilayer results in the modified device output levels and response times.

4.2 Synthesis and Characterization of Silicon Nanowires (SiNW)

Discovery of one-dimensional inorganic materials such as carbon nanotubes and silicon nanowirs had provided researchers with an opportunity to construct electronic interfaces. Nanomaterials have characteristic dimensions comparable to the size of biological molecules, potentially leading to a much more efficient interface. Nanometer sized cross-section gives them enhances surface sensitivity, and allows them to utilize benefits of size effects, such as single-molecule sensitivity, for example silicon nanowires as gene delivery vehicles for mammalian cells, nanowire field effect transistor-neuron device array for detection of neuronal signal propagation, nanowire-arrays for detection of cancer marker proteins.

To synthesize silicon nanowires, vapor-liquid-solid (VLS) mechanism was used. The schematic shows metal-catalyzed SiNW growth process. The growth process begins when the catalyst becomes supersaturated with reactant. The source material carrier gas, SiH4 is introduced into a chamber maintained above eutectic temperature (363ºC for a liquid alloy droplet of AuSi). The carrier gas reacts in the chamber to form liquid eutectic particles and then the silicon diffuses through the catalyst droplets. When the eutectic alloy becomes saturated, silicon precipitates at the liquid-solid interface and nanowires grow.

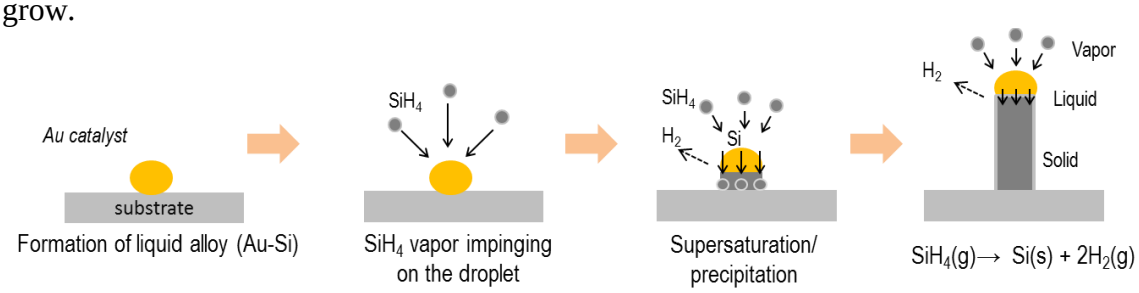

Figure 4.1 Schematic of metal catalyzed SiNW growth by vapor-liquid-solid (VLS) method

Heavily p-type doped (<0.005 Ω.cm) 4’ silicon (100) wafers with 300 nm thermal oxide wafers from Silicon Quest International were used as the substrate for various synthesis and fabrication steps. Silicon wafers were diced into smaller pieces, cleaned with IPA, dried under N_2 stream. These Si pieces were then treated with 0.1% (weight/volume) aqueous solution of poly-L-lysine (PLL) for 5 min, rinsed with DI water, and dried under N_2 stream. A drop of 30 nm gold colloid catalyst solution (Ted Pella) was dispersed onto the chip, incubated for 60s and rinsed with DI water. Excess PLL was removed from the chip using O_2 plasma treatment at 50W for 5 min. The growth substrate with 2nm-thick thin gold film as a catalyst layer can also be used. That thin catalyst layer is deposited onto substrate by e-beam evaporator.

The growth substrate was then placed in a 1-inch quartz tube furnace (Fig. 4.3). Nanowire growth was carried out at a chamber pressure of ~100 Torr and a temperature of ~480 ºC using 36 sccm of SiH4 gas (10% silane in Helium) as a Si precursor and 4

sccm of B2H6 (100ppm diborane in Helium) as dopant. 30-minute long growth produces a large amount of nanowires in the 40 to 80 nm diameter range. To harvest the nanowires for subsequent device fabrication use, the chip with grown nanowires was placed in 1mL of ethanol and sonicated in a water bath sonicator for 1-3 seconds. The resulting silicon nanowires were suspended in ethanol.

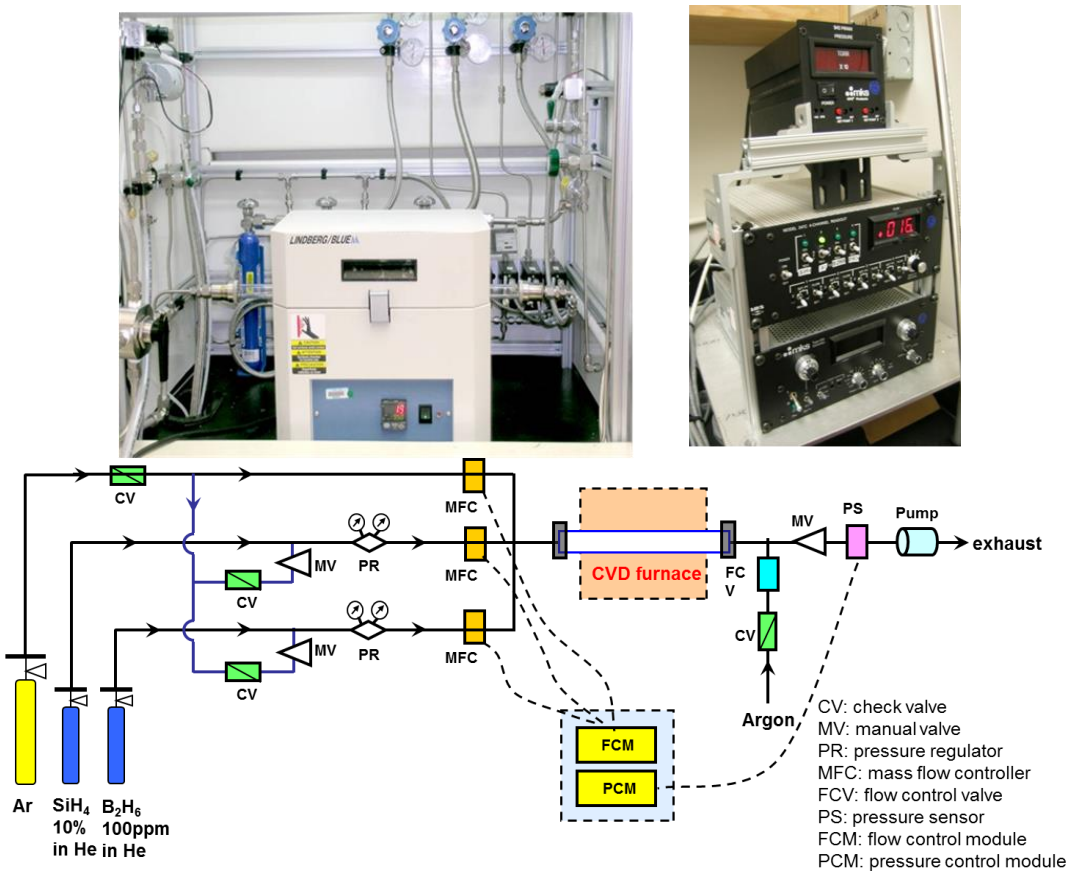

Figure 4.2 CVD setup for synthesis of SiNW. Photograph of furnace and controller (top) and schematic of gas line, furnace, pumping subsystems (bottom)

CVD system for SiNW growth is composed of a tube (TF55030(P)A, Lidberg/Blue with a UP 150 Temperature Controller), mass flow controllers (1179A51CS1B, MKS) for gas delivery. 10% silane in helium (or or hydrogen) as precursor gas and 100ppm diborane in helium (or hydrogen) for p-type doping were purchased from Voltaix, Inc. Argon with ultrahigh-purity level serves as the carrier and purge gas. Stainless-steel tubing and Swagelok fittings were used to connect all components (see Fig. 4.2 bottom). The quartz tube was connected to the gas lines via 25 mm o-ring sealed stainless steel fittings enabling easy opening and sealing of the reaction chamber. A Emechanical pump (Edwards) was used for vacuum and two pressure sensors (Baraton Capacitance Monometer, MKS Series 945 pirani gage vacuum sensor, MKS Instruments) were used to monitor the pressure.

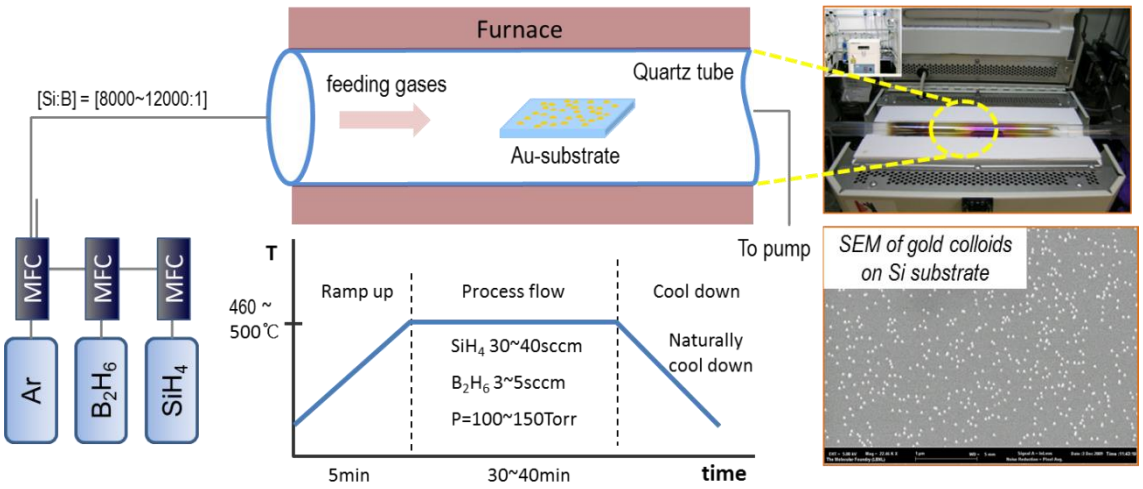

Figure 4.3 SiNW CVD growth setup and a SEM image of catalyst on growth chip

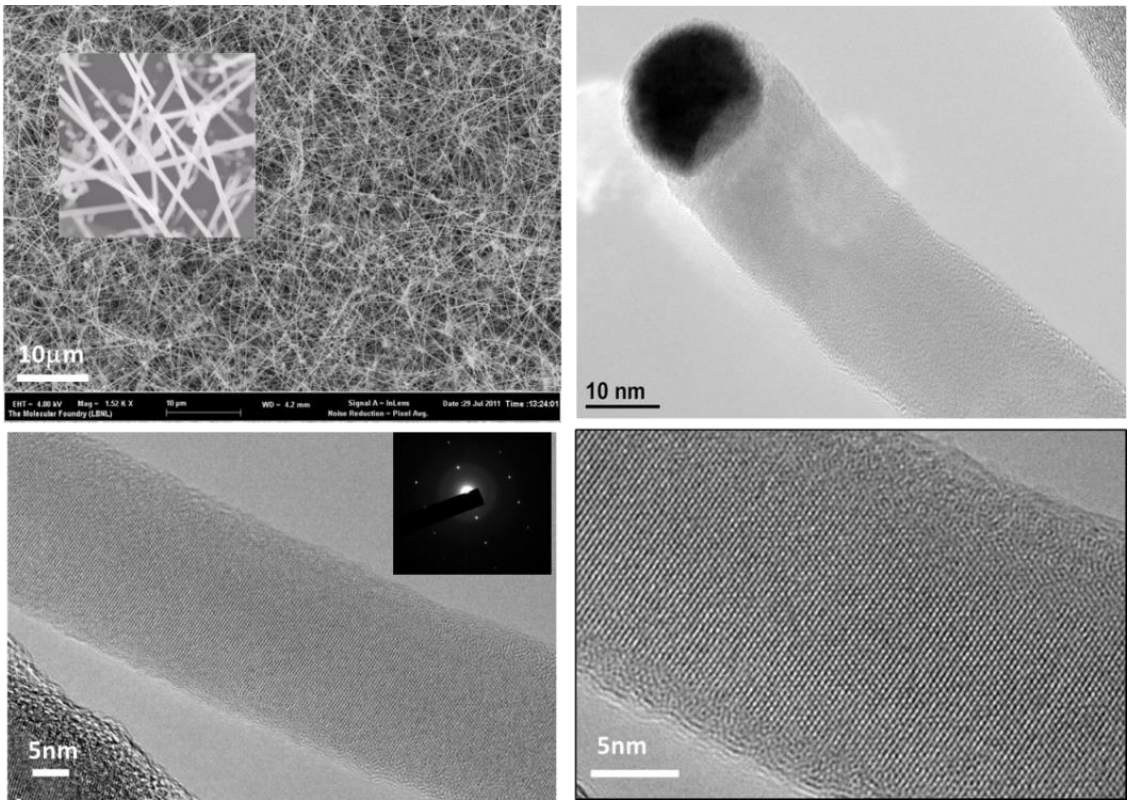

Figure 4.4 SEM and TEM images of silicon nanowires grown by CVD method

The above Fig. 4.4 shows SEM images of SiNW forest on the growth substrate and magnified view of SiNWs with diameter in the range of 40-80 nm. TEM images of SiNW showing crystalline core with amorphous shell. Inset shows electron diffraction of the crystalline core indicating single crystal of silicon.

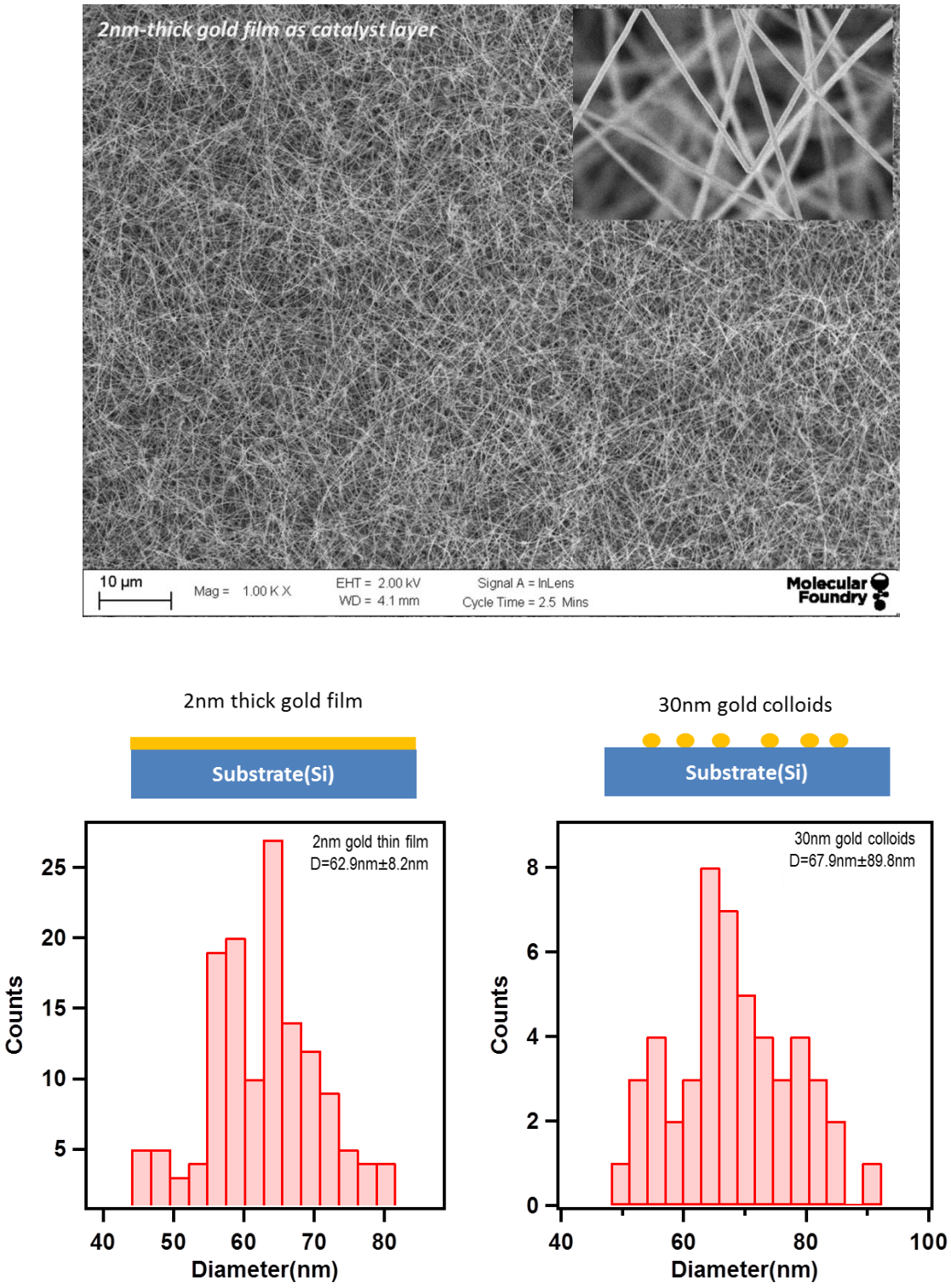

Figure 4.5 Top-view SEM image of p-type SiNWs CVD-grown on Si substrate with 2nm-thick gold thin film and histograms of typical diameter distribution obtained from SEM images. Average values of both samples are 63nm and 68 nm in diameter for each

4.3 Fabrication of Silicon Nanowire Field Effect Transistors (SiNW FET)

4.3.1 Fabrication process of SiNW FET

4.3.1.1 Nanowire alignment

Silicon wafers were dehydrated in a 180 ºC convection oven for about 30 min and allowed to cool to room temperature. Subsequently, the wafer was treated with 0.1% (weight/volume) aqueous solution of PLL for 3min rinsed with DI water and dried under N2 stream. A polydimethylsiloxane (PDMS) micro-channel stamp was placed on the device silicon and the nanowire suspension was introduced through the channel at a 0.1 ml/min flow rate to deposit and align the nanowires in the direction of the flow. Alternatively, the nanowires were deposited onto the wafer directly using the dry transfer method. In one variation a small chip with as-grown nanowires was translated across the wafer. In another, the nanowires were first deposited onto a PDMS stamp surface by touching the stamp to the nanowire chip and then touching the stamp to the wafer surface. PLL was subsequently removed using oxygen plasma etching as described in the previous sections. At the last step the wafer was annealed at 180 ºC for 10min in inert gas. PDMS Micro-channel was fabricated by following way. PDMS pre-polymer solution and the curing agent at a ratio of 10:1 (weight/weight) were thoroughly mixed and degassed using vacuum. PDMS was cast on a microchannel pattern [500 μm × 50 μm × 1 cm (w × h × l)] pre-patterned with SU8 photoresist on a silicon wafer and was cured at ~80 ºC on a hotplate for 1hr. Micro-channels 'stamps' were cut from the master-mold and sonicated in ethanol for 5 min to clean them before use.

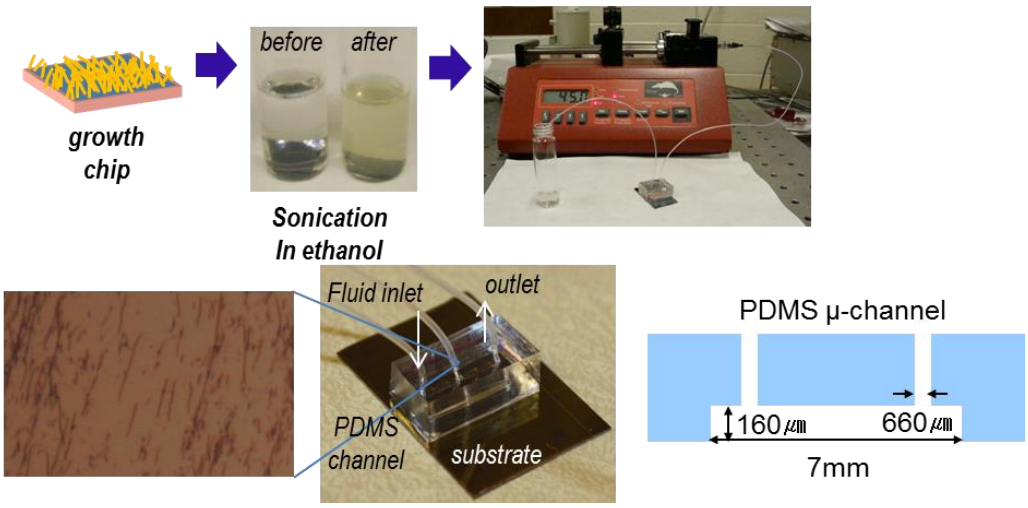

Figure 4.6 Solvent flow-induced nanowire alignment

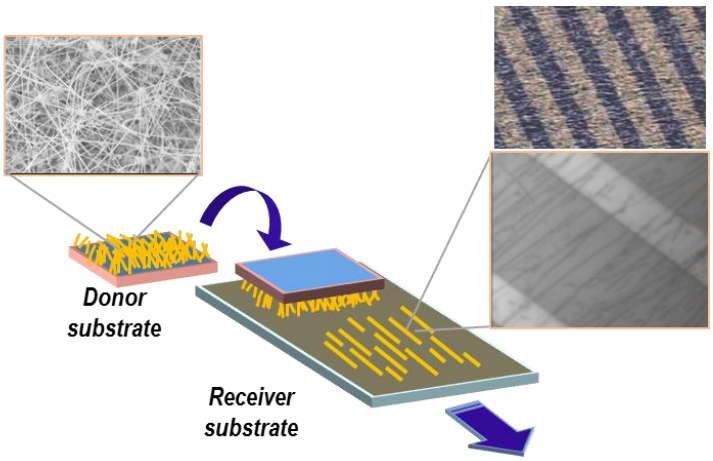

Figure 4.7 Nanowire transfer by contact printing method

4.3.1.2 SiNW FET device fabrication

Source-drain electrode patterning: The device wafer with aligned nanowires was again dehydrated in 180 °C convection oven for about 30 min and allowed to cool to room temperature. LOR-3A photoresist was spun on the wafer at 4000 rpm for 40 s to obtain ~350 nm thick film. The wafer was baked at 180 °C for 5 min in a convection oven. After cooling the wafer to room temperature, S1805 photoresist was spun onto the wafer at 4000 rpm for 40 s to obtain film thickness of ~400 nm. This wafer was subsequently baked for 90 s at 110 ºC on a hotplate. The wafer chip was exposed through a photomask using an aligner tool (ABM Inc.) operated in a vacuum contact mode for ~3 s at 17 mW/cm^2. The exposed wafer was developed in AZ-300 MIF developer for 20-40 s using gentle agitation. Wafer was immediately washed with DI water, dried in N_2, and cleaned with O_2 plasma at 30 W to remove any residual photoresist from the developed regions. Native oxide on the silicon nanowires in the open contact regions was etched away using buffered oxide etchant (BOE) for 7-8 s followed by rinsing with DI water and drying with N_2. 100 nm Ni was subsequently deposited, at a pressure below ~1×10^{-7} Torr, onto the patterned chip to define source and drain electrode contacts to the nanowire with 5 μm spacing. Lift-off was carried out in Remover-PG at 70 °C to define the final device structure.

Device Annealing: After lift-off, the device wafer was annealed at 380~395°C in a forming gas 10% H_2/90% N_2 for 2 min using a rapid thermal annealing apparatus to form ohmic contacts between the nanowire and the nickel contact electrodes. A pre-soak at 200°C for 2 min was used to eliminate any moisture prior to carrying out the higher-temperature anneal.

Electrode passivation: Contact Ni electrodes were further passivated by spin coating the wafer with HMDS adhesion promoter at 1000 rpm for 40 s followed by spin-coating of photoresist S1805 at 4000 rpm for 40 s. Photoresist layer was further baked at 115 ºC for 90 sec and patterned using a photomask on an optical aligner similar to earlier steps. The mask was aligned to the metal contact electrode layer such that a 2 □m channel is exposed in the gap between metal contact electrodes. The pattern was developed in AZ 300-MIF developer to form the channel that exposes SiNWs in the

region between metal electrodes. For measurements, the device chip was mounted in a home-built holder with a PDMS channel (similar to the one used for nanowire alignment) bearing inlet/outlet openings for liquid flow and a third opening for inserting a leak-free Ag/AgCl reference electrode (Warner Instruments, LLC), which was used as a gate electrode.

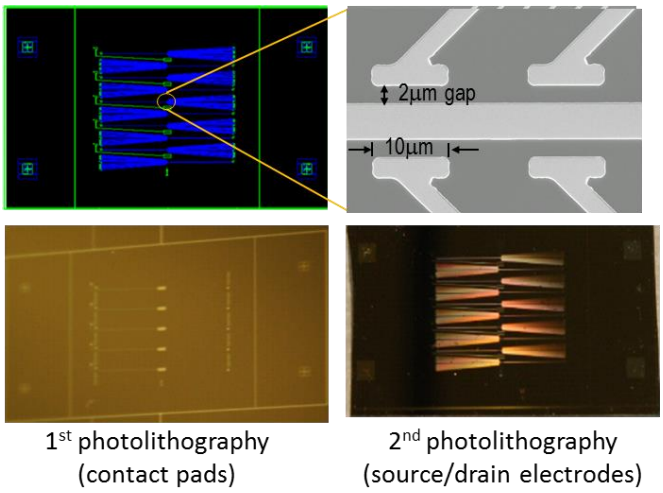

Figure 4.8 Images of Si_3N_4-passivated SiNW FET device (A: schematic of device pattern, B: SEM image of device pattern, C&D: optical images of fabricated SiNW-FET

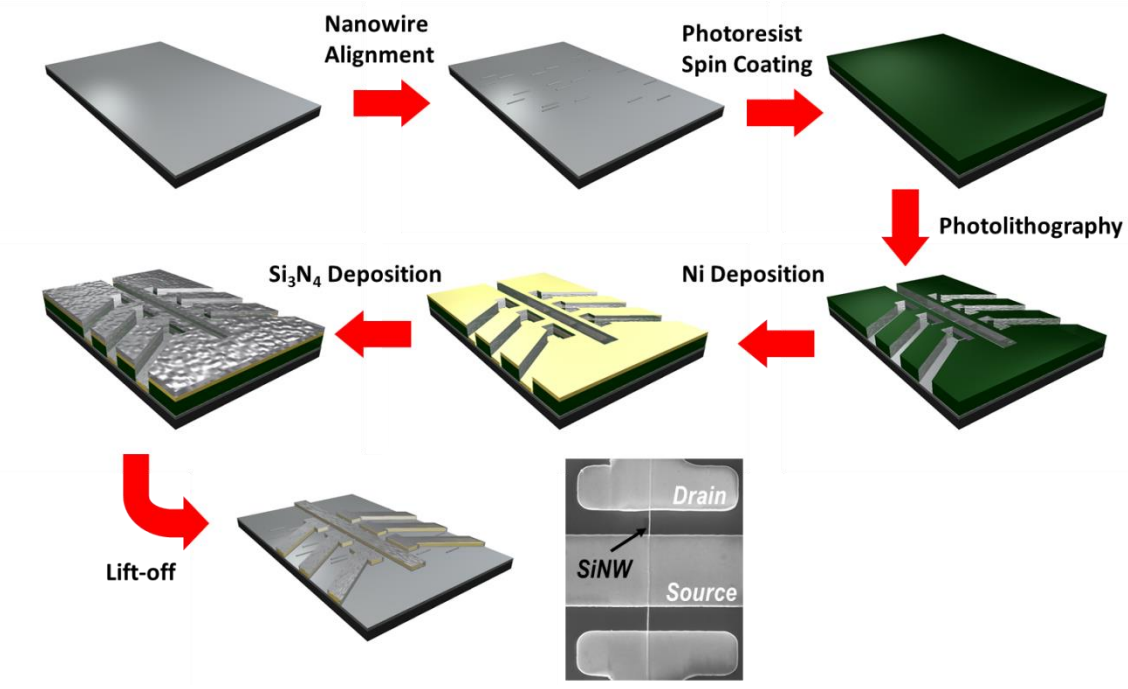

Figure 4.9 Schematic of fabrication process of SiNW field effect transistor with silicon nitride passivation of metal electrodes. An 100nm conformal layer of stoichiometric silicon nitride was deposited onto metal contacts by PECVD

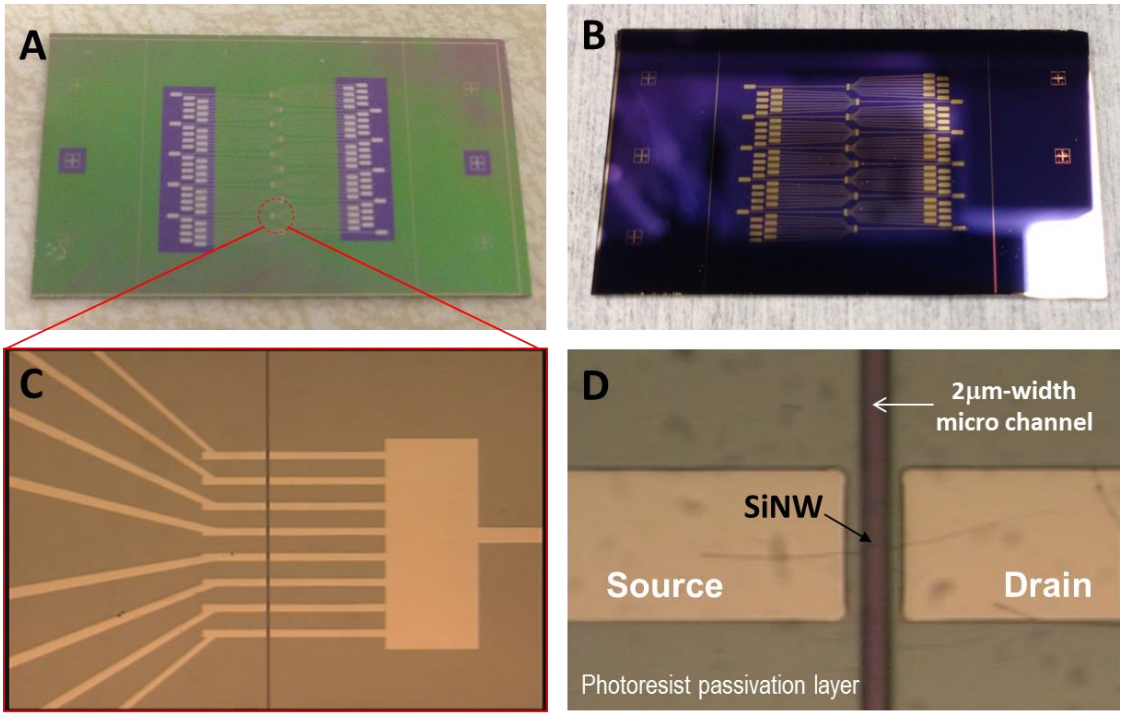

Figure 4.10 Optical images of photoresist-passivated SiNW FET device (A: device chip before photoresist-passivation, B: after photoresist-passivation, C: optical image of photoresist-passivated SiNW FET, D: magnified view of single SiNW transistor with 2μm-width micro trench

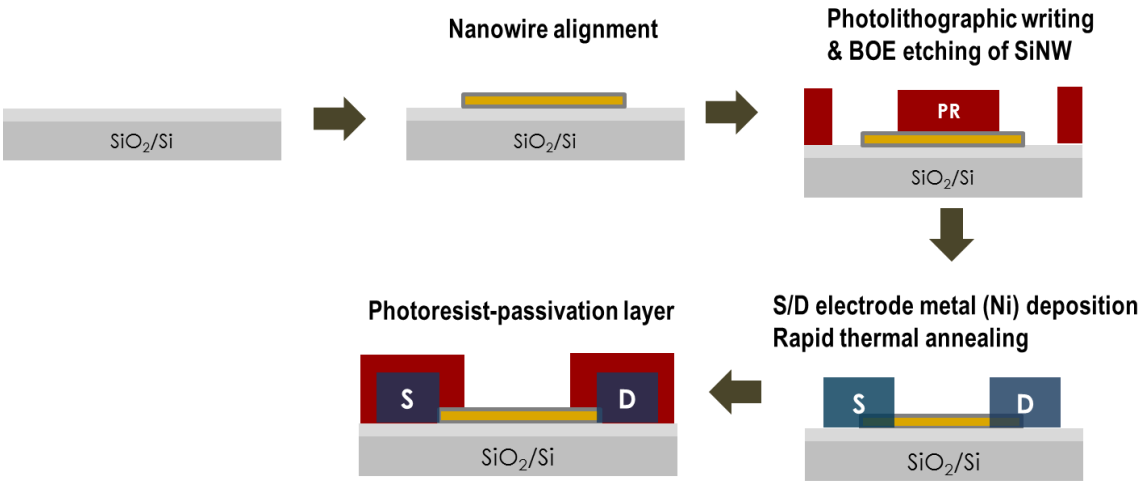

Figure 4.11 Steps for photoresist passivated SiNW FET devices

4.3.2 SiNW FET Device Characterization

Fully assembled devices were mounted onto a probe station shielded with a Faraday cage. Transfer characteristic ($I_{S\text{-}D}$ vs V_G or *I-V*) and real time ($I_{S\text{-}D}$ vs t) measurements were done using a home-built measurement system that used a set of NI-DAQ cards (National Instruments) for AC source-voltage (V_S) application. Lock-in detection was performed using Keithley 428-PROG preamplifier along with National Instrument's lock-in kit for Labview. I-V curve acquisition and time-trace measurements were carried out using AC source-drain bias of 200 mV (amplitude) at 5 Hz and 100 Hz frequencies.

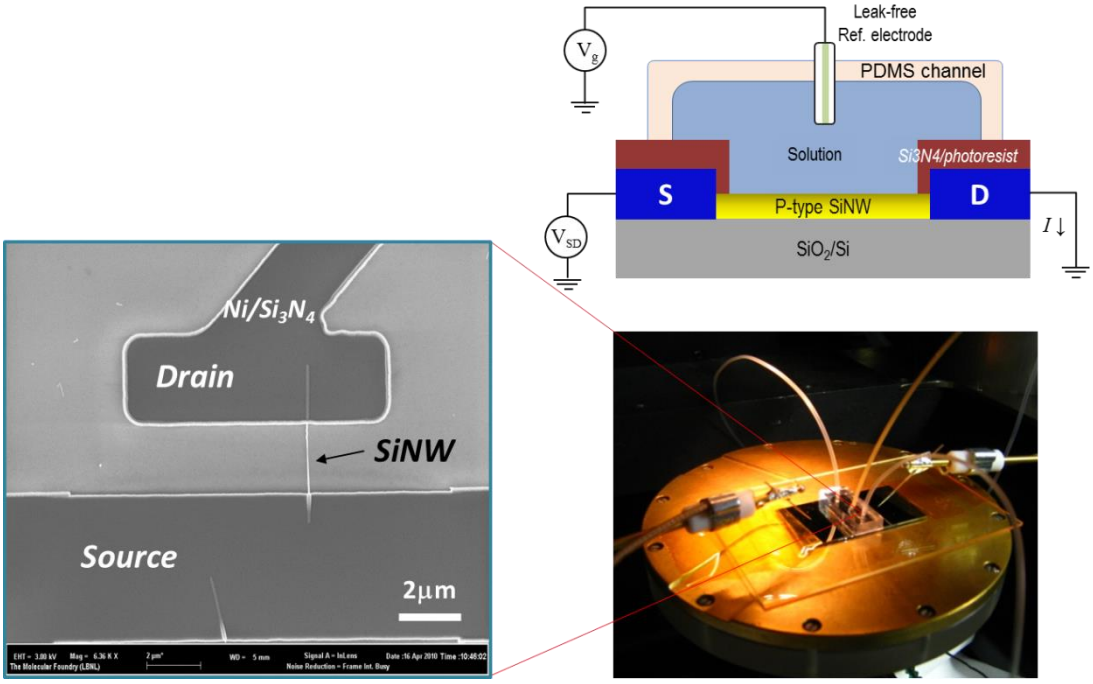

Figure 4.12 Schematic of experimental setup used for current-voltage measurement of silicon nanowire devices and SEM images of single-SiNW FET device.

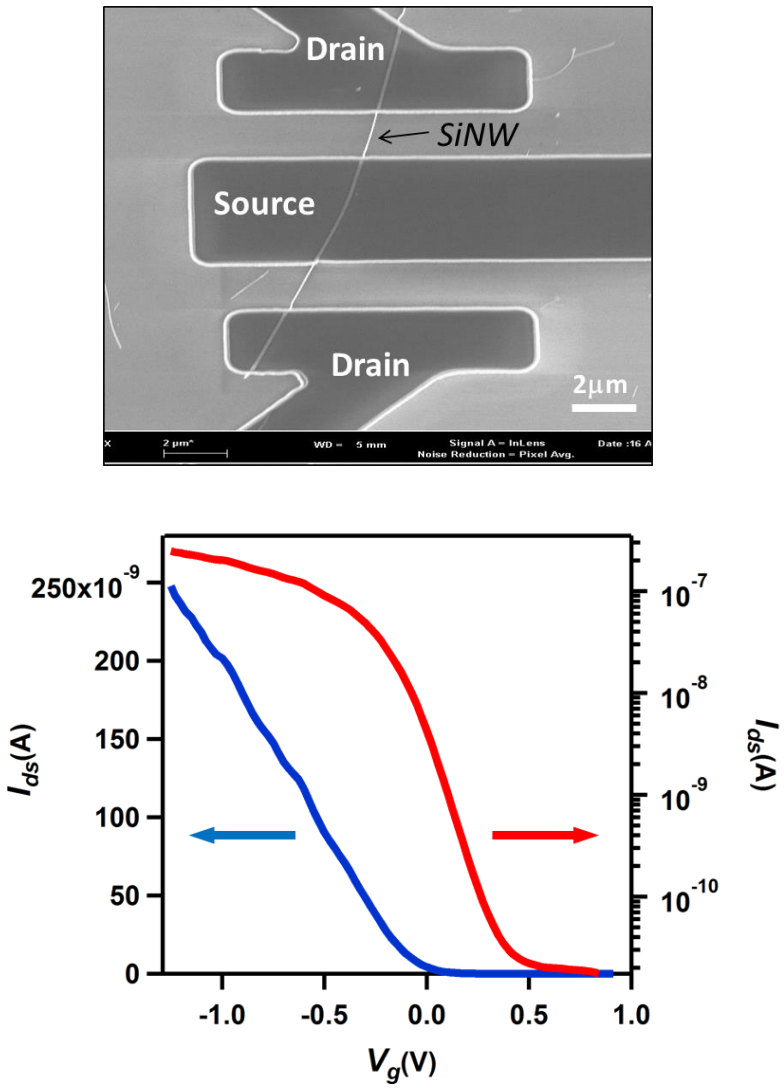

Figure 4.13 Transfer characteristic for the bare p-type SiNW FET device fabricated (blue: linear scale, red: log scale) shows excellent device performance with on/off ratio of ~10^4 and top-view SEM image of SiNW FET

pH response of the bare SiNW devices by flowing buffer solution of different pH was also obtained and the steady-state conductance of the device was recorded (Fig. 4.14). Actually, a highly ubiquitous application of SiNW-based FET sensing is pH detection. Since pH changes are a common feature of many biological processes, this sensing modality is especially important for bionanoelectronics. As the solution pH changes, charging of silanol groups at the silicon oxide layer on the surface of p-type SiNWs leads to changes of the depletion region in the SiNW channel that then affects the source-drain current at a given gate voltage[93]. To show that the devices can respond to the proton concentration, it was tested with phosphate buffer solution with pH range 3-8. The sensitivity of NW electrical response to the proton concentration is 43.6mV/pH. Bare p-type SiNW FETs showed a pronounced increase in conductance when the pH of the

fluidic environment around the NWs was changed from 3 to 8, which corresponded to the average pH sensitivity of 50–100 nS/pH in the pH range of 3 to 8.

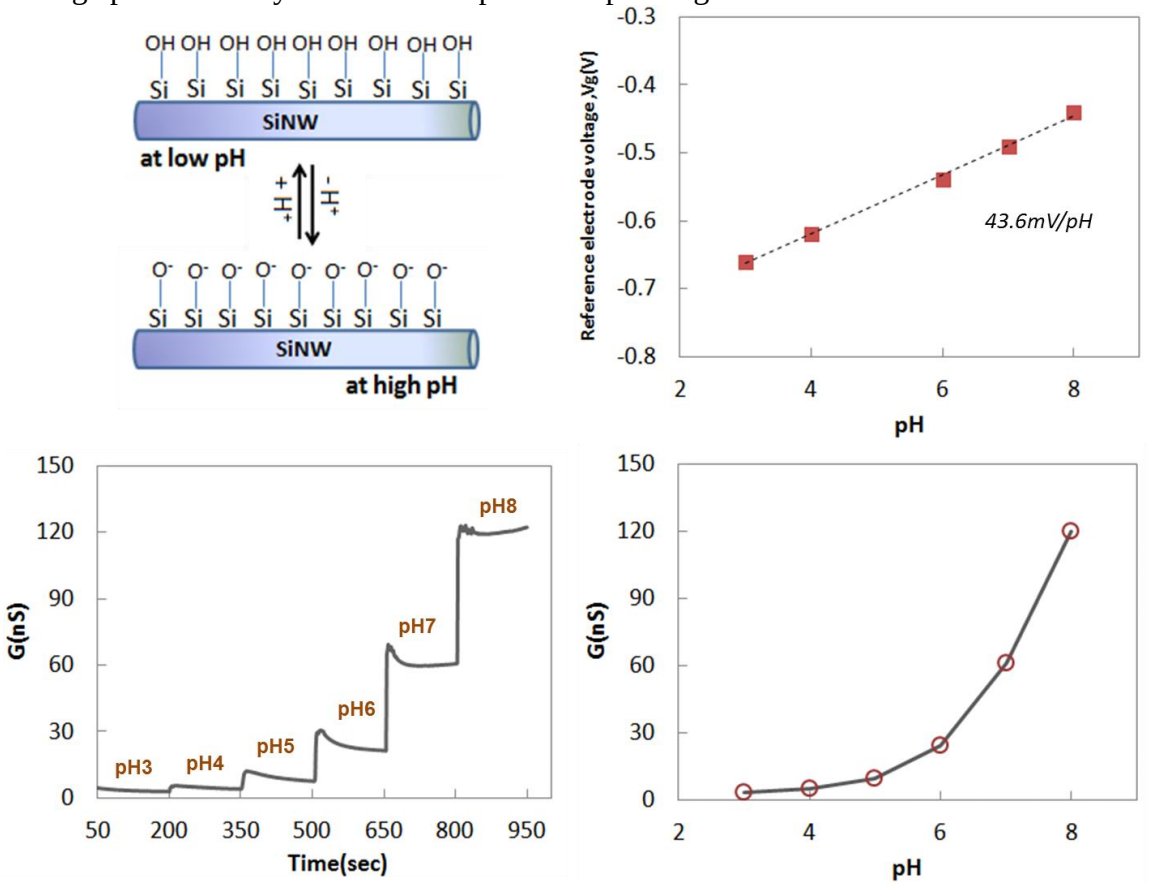

Figure 4.14 pH response of bare silicon nanowire devices

4.3.3 Lipid bilayer assembly on SiNW FET devices

An important step toward building bionanoelectronic interface would involve functional integration of nanomaterials with membrane proteins. Actually, if biological material is deposited directly on silicon, the organic will die. With the lipids as an interface, the two disparate materials can be combined. Biocompatible one-dimensional lipid bilayer with membrane protein channels on silicon nanowires can be proposed for functional integration. Silicon nanowires present two-distinct length scales that are advantageous for assembling and building bionanoelectronic architectures. Nanoscale cross-section gives enhanced surface sensitivity and long axial dimensions can simplify manipulation and assembly into functional devices and enables macroscopic connections, control and readouts. Silicon oxide surface is very biologically friendly. Silicon nanowire field effect transistor can operate in ionic solutions, provide a natural and effective

connection between micrometer-size active area of device and macroscopic measurement equipment, a single device chip can house hundreds of individual devices, and most importantly transistor gain provides an effective means of amplifying very weak signals generated by biological events. Lipid membrane is a universal matrix that can house a number of protein machines. Lipid bilayers are virtually impermeable to ions and large molecules, which makes them also suitable as a natural barrier that prevents non-specific adsorption.

Functional proteins can be incorporated into silicon nanowire transistors by covering nanowire with a lipid bilayer shell that forms a barrier layer between nanowire surface and solution species. This shielded wire configuration allows us to use membrane functional proteins as the only pathway for the ions to reach the nanowire. This also could be how to use the nanowire device to monitor specific transport and also to control the membrane protein.

4.3.3.1 Liposome formation and Lipid bilayer fusion on SiNW devices

The key procedure for building my bionanoelectronic device was the formation of lipid bilayer on the surface of the SiNW. The hydrophilic negatively charged native oxide present on the NW surface in solution makes NWs particularly attractive as a template for supporting lipid bilayer formation.

300 μl of DOPC (10 mg/ml) in chloroform (Avanti Polar Lipids) were added to a glass vial with a Teflon-lined lid. For fluorescence imaging 11 μl of TexasRed-DHPE lipid (10 mg/ml) in chloroform was added to the lipid composition. Chloroform was subsequently evaporated in a Biotage V-10 evaporator to form a lipid film on the vial walls. This vial was further stored in a vacuum desiccator overnight to ensure complete removal of chloroform before use. Dried lipid film was then hydrated with 1 ml of 150 mM KCl, 1 mM KH_2PO_4, pH 6.8 buffer to a final lipid concentration of 3 mg/ml and extruded through a 200nm pore size filter using a hand-extruder (Avanti Polar Lipids).

Liposome solutions were flown over the SiNW FET devices through the PDMS microfluidic channel and allowed to fuse over the nanowire surface for a minimum of 30 min, followed by washing with copious amounts of 150 mM KCl, 1 mM KH_2PO_4, pH 6.8 buffer, to remove un-ruptured vesicles. Bilayer formation, uniformity and mobility were evaluated by incorporating 0.5% Texas-Red-DHPE lipid (Invitrogen) into the lipid composition. To estimate the mobility of lipid molecules in the bilayer we performed fluorescence recovery after photobleaching (FRAP) experiments using a confocal microscope (Zeiss LSM 710).

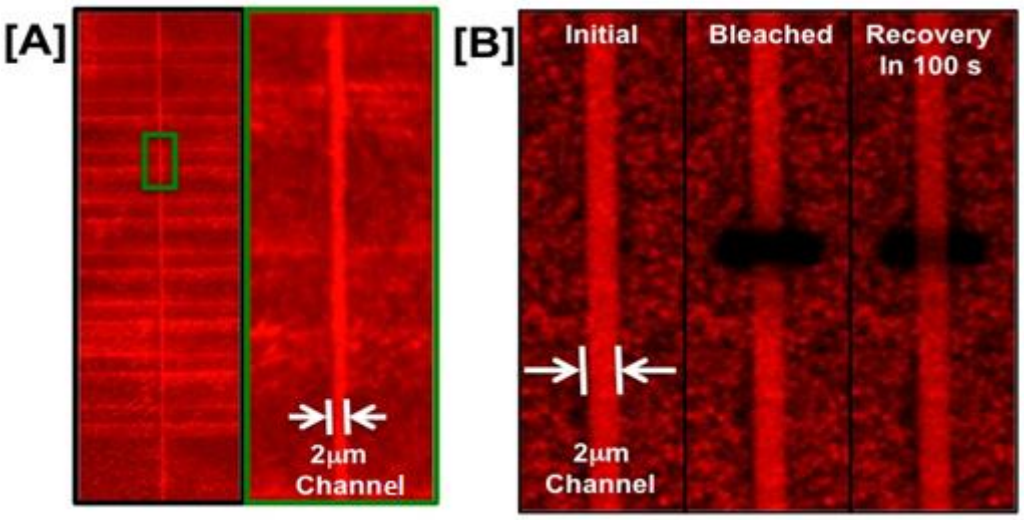

Figure 4.15 Image of lipid bilayer coverage on SiNW

Fig. 4.15 shows Texas red fluorescence images showing uniform bilayer coverage in the 2 μm active photoresist channel between metal contact electrode region on the device chip [A] and FRAP images show TR-DHPE fluorescence initially, after bleaching, and recovery after 100 s in the channel region. These images show uniform bilayer in the channel region. Bilayer mobility in the channel region was calculated to be ~1 $\mu m^2/s$ [B].

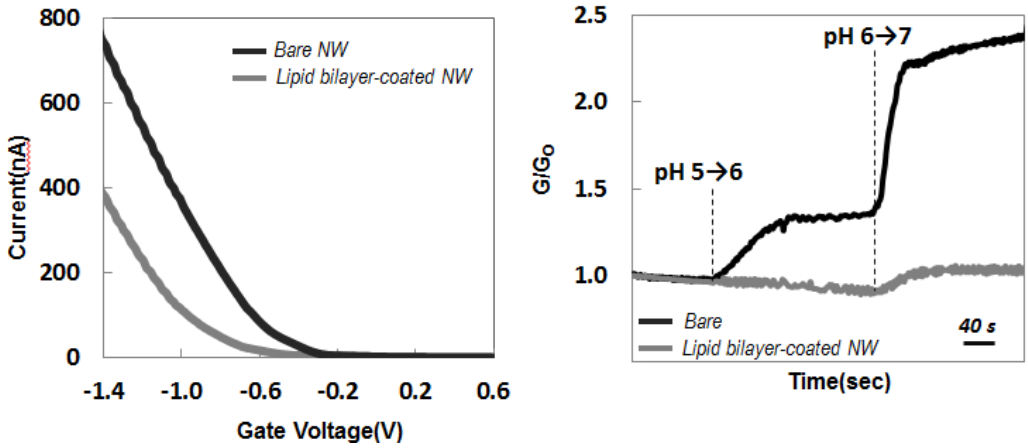

Figure 4.16 pH response of lipid bilayer-coated SiNW surface

These data indicate that the DOPC bilayer membrane blocks proton transport between the fluid environment outside the lipid bilayer and the hydration layer situated between the inner leaflet of the bilayer and SiNW surface. Time traces of normalized conductance of uncoated SiNW transistor and lipid-bilayer coated SiNW transistors as pH solution changed from 5 to 7. Bare NW FETs shoed a pronounced increase in conductance when pH of fluidic environment around NWs was changed from pH 5-7. lipid bilayers on SiNW surface provide good shielding of the nanowires to protons.

4.4 Light-Powered Bioelectronic Devices with Biologically-Tunable Performance

Many key biological processes ranging from cell signaling to energy production involve active and passive ion translocation across cell membranes and often other proteins and small molecule mediators provide critical regulation of such transport. Here these biological regulation mechanisms were adapted to control bioelectronic devices based on silicon nanowire transistors that incorporate a functional light-activated proton pump, bacteriorhodopsin (bR). Bacteriorhodopsin (bR)-lipid bilayer integrated onto SiNW bioelectronic devices

4.4.1.1 Materials and methods

SiNW growth and FET device fabrication: As previously described in Chapter 4.3, P-type silicon nanowires with diameters in the range of 40-80 nm were grown using catalytic chemical vapor deposition (CVD). SiNWs were aligned onto a SiO_2 surface using flow alignment technique[94]. The source-drain electrode contacts, with a typical spacing of 5 μm, were patterned on the wafer using photolithography, and the chip was subsequently passivated with an additional photoresist layer, creating a 2 μm channel exposing the SiNWs. These devices were then placed into a PDMS fluid cell with inlet/outlet ports for solution delivery, and an opening for a leak-free gate electrode.

Proteoliposome preparation and characterization: For bacteriorhodopsin incorporation into the liposomes, pre-formed vesicles were de-stabilized with n-dodecyl-β-D-maltoside (βDDM, Sigma-Aldrich). Purified bacteriorhodopsin (Sigma-Aldrich, some bR protein was also provided by M. Coleman (LLNL)) was added to the de-stabilized vesicle solution to a final bR: lipid molar ratio of 1:500 and final βDDM concentration of 0.008%. This solution was incubated at room temperature for 45 minutes and then the surfactant was slowly removed by using bio-bead SM-2 adsorbent (Bio-Rad). Stepwise addition and removal of 40 mg/mL bio-beads to the proteoliposome solution was done 5 times over 5 hours of incubation. This solution was further purified to remove unincorporated bR and any remaining surfactant micelles by size exclusion column chromatography using 10 mL column (Pierce) packed with Sepharose CL-6B (Singma-Aldrich). Fractions were collected and analyzed with Nanodrop 2000 UV-Vis (Thermo-Scientific) to identify the fraction containing bR proteoliposomes. Successful incorporation of bR into liposomes was verified using UV-Vis spectroscopy and dynamic light scattering (DLS) measurements before and after reconstitution. Proteoliposome solution was pushed into a PDMS channel covering the device chip and allowed to fuse for 30 minutes. For measurements the PDMS channel was filled with 150 mM KCl, 1 mM KH2PO4, pH 6.8 buffer solution. Confocal laser scanning microscopy was used for characterization of formation of lipid bilayer coverage and mobility on the SiNW. These properties were verified by adding a small amount of TexasRed-DHPE to the lipid mixture and imaging the bilayer with a scanning confocal microscope (Zeiss LSM710 with Zen software).

Gramicidin A (gramA) incorporation in the bR reconstituted vesicles: GramA was dissolved in ethanol to obtain a final concentration of 5mg/ml. 300 μl of DOPC was

added to a glass vial with a Teflon-lined lid. An aliquot of the gramA solution was added to the same glass vial to obtain a mixture containing gramA: lipid at molar ratio of 1:200. Subsequently, the solution mixture was dried to form a film. Starting with this lipid/gramA film, proteoliposomes were prepared as described in the previous section.

Ionophore Incorporation: Ionophores, valinomycin and nigericin, were added to the solution in the PDMS microfluidic channel at a final concentration of 2 μM and incubated in the fluid cell for approximately 30 min to allow sufficient time for incorporation into the bR containing bilayer. Afterwards, the chamber was washed with buffer. GramA was co-reconstituted with bR during proteoliposome preparation, at a ratio of 1:200 gramA: lipid.

Device Measurements: Assembled devices were mounted in a shielded probe station. Transfer characteristics (I_{S-D} vs V_G) and real time (I_{S-D} vs t) measurements were recorded with a home-built measurement system that used a NI-DAQ card and a Keithley 428-PROG pre-amplifier. To improve the signal to noise ratio we have applied an AC bias between the source and drain electrodes and used lock-in detection to measure the source-drain current. For device photoactivation we used an external LED light source (SCHOTT KL 2500) fitted with a green (560 nm) bandpass filter (Newport Corp.). The light source output had a power density of 136 mW/cm^2 at 100% illumination and a spot size of 1 cm in diameter.

4.4.1.2 Device design and operation

The basic device platform (Fig. 4.17) was based on a microfabricated SiNW field-effect transistor in which the nanowire ends were clamped between a pair of source and drain electrodes insulated from the solution by a protective photoresist layer. A microfluidic channel filled with a buffer solution covered the active area of the chip. This configuration allowed us to fuse proteoliposomes to create a continuous lipid bilayer onto the SiNW surface while keeping the bilayer and proteins in their native hydrated state during subsequent device measurement. The lipid bilayer covering the nanowire surface contained bR, a protein from the purple membrane of *Halobacterium salinarum*. bR absorbs green light (λ_{max} = 560nm) and undergoes a multi-state photo-cycle that translocates a proton across the membrane[95]. In bacteria, this process builds up the proton motive force[96] that subsequently powers ATP synthesis. Bacteriorhodopsin is also exceptionally stable *ex-vivo* under diverse environmental stresses and over a broad range of pH and temperature [97, 98].

After we reconstituted bR into preformed 1,2-dioleoyl-sn-glycero-3-phosphocholine (DOPC) liposomes and fused the resulting proteoliposomes onto the device surface, fluorescence microscopy imaging (Fig.4.16) indicated that the lipid bilayer covered the nanowire device completely. To visualize the bilayer a small portion of the lipid was labeled with a TexasRed™ fluorescent dye. Inset of Fig.4.16 shows a scanning confocal microscope image of a single device region of the chip showing a SiNW covered with lipid bilayer. Moreover, fluorescence recovery after photobleaching (FRAP) measurements indicated that the lipid bilayer covering the nanowire was continuous and mobile (Fig. 4.15), both of which are important properties for providing good shielding of the SiNW surface and accommodating the membrane proteins.

Time trace of the SiNW transistor source-drain current was recorded under 3 cycles of green light (560nm) illumination for the uncoated SiNW device (black trace) and the device coated with a lipid bilayer containing bR protein (red trace).

Upon exposure to 560 nm green light, the SiNW devices that did not contain membrane proteins registered small amounts of photocurrent (Fig.4.17, black trace)[99]. This signal was quite small (the maximum conductance change was less than 0.1%) and exhibited almost instantaneous turn-on and turn-off kinetics: upon illumination the signal immediately increased to a steady-state level, which then decayed back to baseline level as soon as the light was turned off. When the lipid membrane covering the SiNW contained bR protein, the device showed a markedly different response to the green light exposure (Fig. 4.19, red trace). The source-drain current started to decrease with the magnitude of this decrease exceeding that of the photocurrent by at least an order of magnitude. Unlike the photocurrent signal, this signal change was not instantaneous, but instead showed a fast initial rate of change followed by gradual slow-down. After the illumination was switched off, the current slowly returned to its original level. This cycle was repeatable (Fig.4.19) without any significant losses of signal strength or fidelity. These observations indicate that the observed electronic response is caused by the photoinduced activity of bR protein.

The following mechanism is proposed for the observed device response. It is unlikely that the proton gradient build-up and the associated electrical potential across the membrane are responsible for the slow-down, since this hypothesis cannot explain why the devices return to their initial state after the light is switched off. Instead, a much more likely mechanism involves the interplay of the two processes that occur in the illuminated device. Upon exposure to green light, the bR proteins in the lipid membrane start pumping protons across the lipid bilayer, building up a proton gradient across the bilayer. The resulting change in the SiNW surface charge due to the protonation of $SiOH^-$ groups causes a decrease in the current output[100]. A competing process involves passive diffusion of protons across the lipid bilayer that tries to equilibrate the proton concentration on both sides of the membrane. The rate of diffusion increases with the increasing proton gradient magnitude, and the proton pumping rate does not. As these processes begin to offset each other, the device rate of response slows down and eventually should reach a steady state. When the light is switched off and the protein stops pumping protons, the leakage through the bilayer continues to deplete the transmembrane proton gradient. Eventually the device returns to its baseline state and becomes ready to repeat this sequence of events during the next illumination cycle.

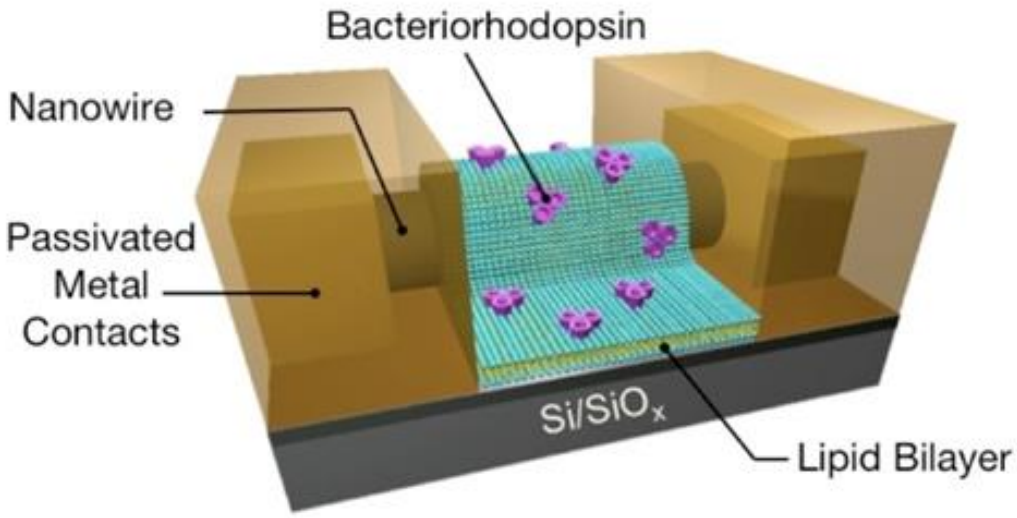

Figure 4.17 Device schematics showing a SiNW transistor with the nanowire covered with a lipid bilayer containing bacteriorhodopsin protein

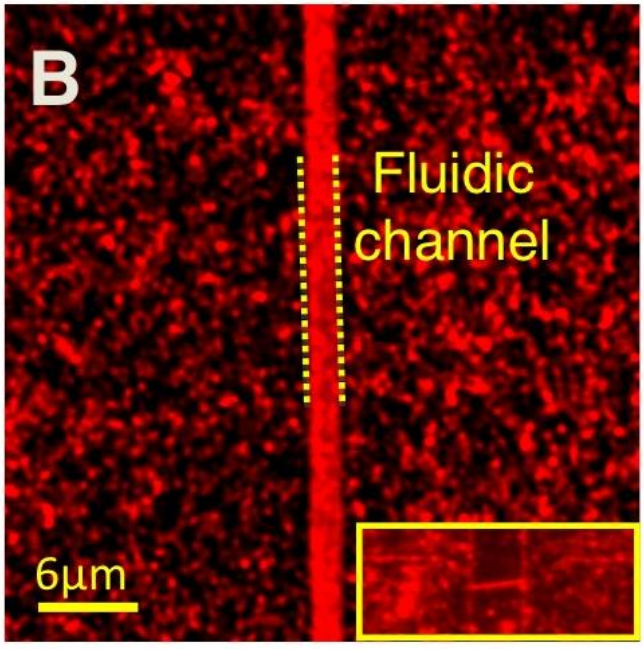

Figure 4.18 Scanning confocal microscopy image of the chip coated with lipid bilayer.

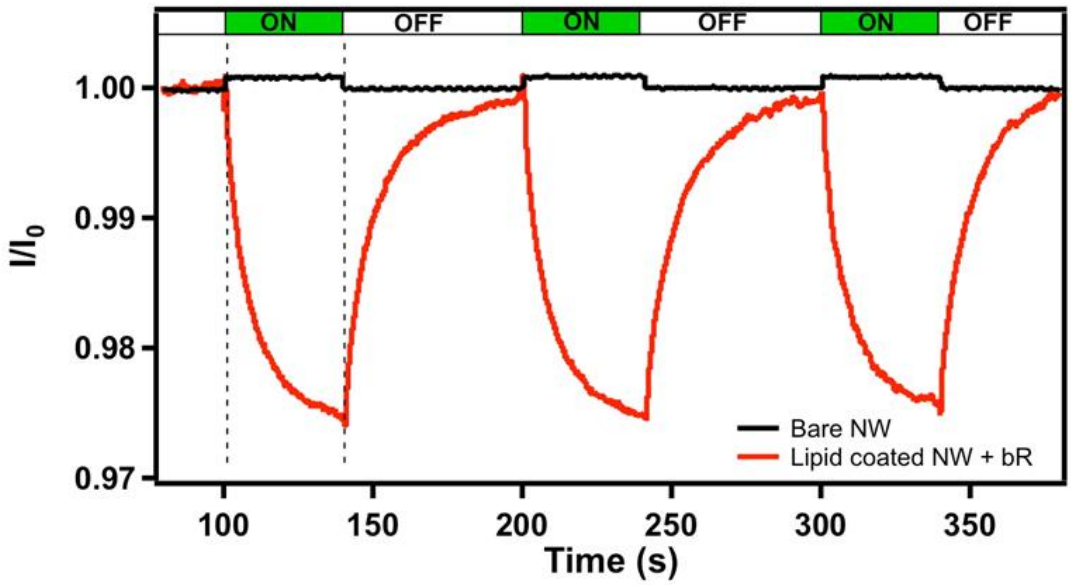

Figure 4.19 Normalized time trace of the SiNW transistor source-drain current

4.4.1.3 Quantitative analysis of the device performance

The quantitative model describing such kinetics is similar to the model of the operation of the Na,K-ATPase driven bioelectronic transistor[92]. The proton pumping and proton leakage rates define the two main model parameters. As long as the incident light intensity is not causing the protein response to saturate, the proton gradient build-up could be described as the zero-order process governed by the light-intensity-dependent rate of proton pumping, I_0. Proton leakage through the lipid bilayer obeys Fick's law where the leakage rate, governed by the time, τ, is proportional to the magnitude of the transmembrane proton gradient. If we assume that the conductance shift of the device is proportional to the change in the proton concentration, C, (i.e. that the device operates within the linear part of the pH response curve of the SiNW transistor, Fig. 4.20), then the kinetics of the device response can be described by a master equation:

$$\frac{dC}{dt} = I_0 - \frac{1}{\tau}\Delta C \qquad (1)$$

where $1/\tau$ represents a first-order kinetic constant for the leakage process. When the device is illuminated, then the proton concentration gradient should rise as:

$$C(t) = C_0 + I_0\tau(1 - e^{-\frac{t}{\tau}}) \qquad (2)$$

and when the light is switched off, the decay of the proton gradient can be described by:

$$\Delta C(t) = \Delta C_0 \cdot e^{-\frac{t}{\tau}} \qquad (3)$$

where ΔC_0 is the proton gradient value reached at the moment when the light was shut off. Indeed, the device response kinetics follow the relationships predicted by the Eq. 2,3 (Fig. 4.21a).

This model also points to several key features of the device kinetics. First, as the proton leakage process plays a role both during the light-ON and light-OFF cycles, the leakage time estimated from the rise and fall regions of the response curve should be identical, which is indeed what we observed in the experiments (Fig. 4.21a, inset). Second, the initial pumping rate should show the linear dependence on the intensity of the incident light, at least until bR activity reaches saturation. Again, the values of the initial pumping rates that we measured at 5 different light intensities follow this dependence (Fig. 4.21b).

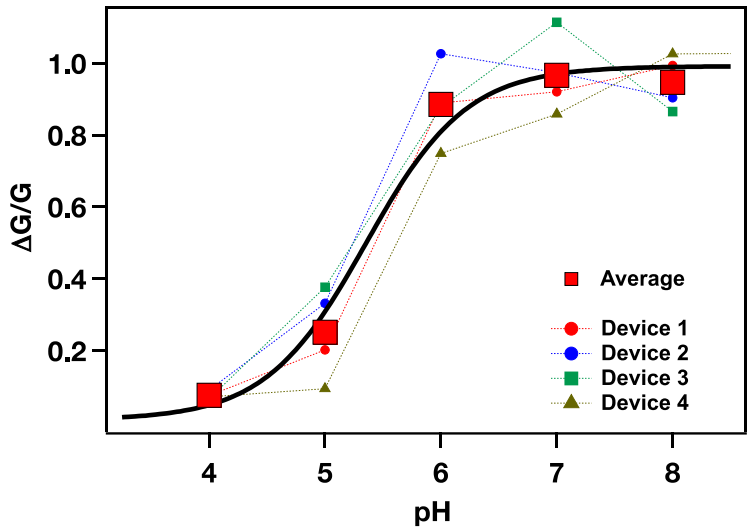

Figure 4.20 Average pH response curve (red filled squares) and individual pH response curves (dotted lines) for four SiNW FET devices

The pH response of the bare SiNW devices by flowing buffer solution of different pH through the fluid cell and recording the steady-state conductance of the device was obtained. The pH response shows a well-defined transition centered around pH=5.4. Black solid line shows the fit of the averaged data to the Henderson-Hasselbalch equation with the fitted pKa value of 5.3558±0.196.

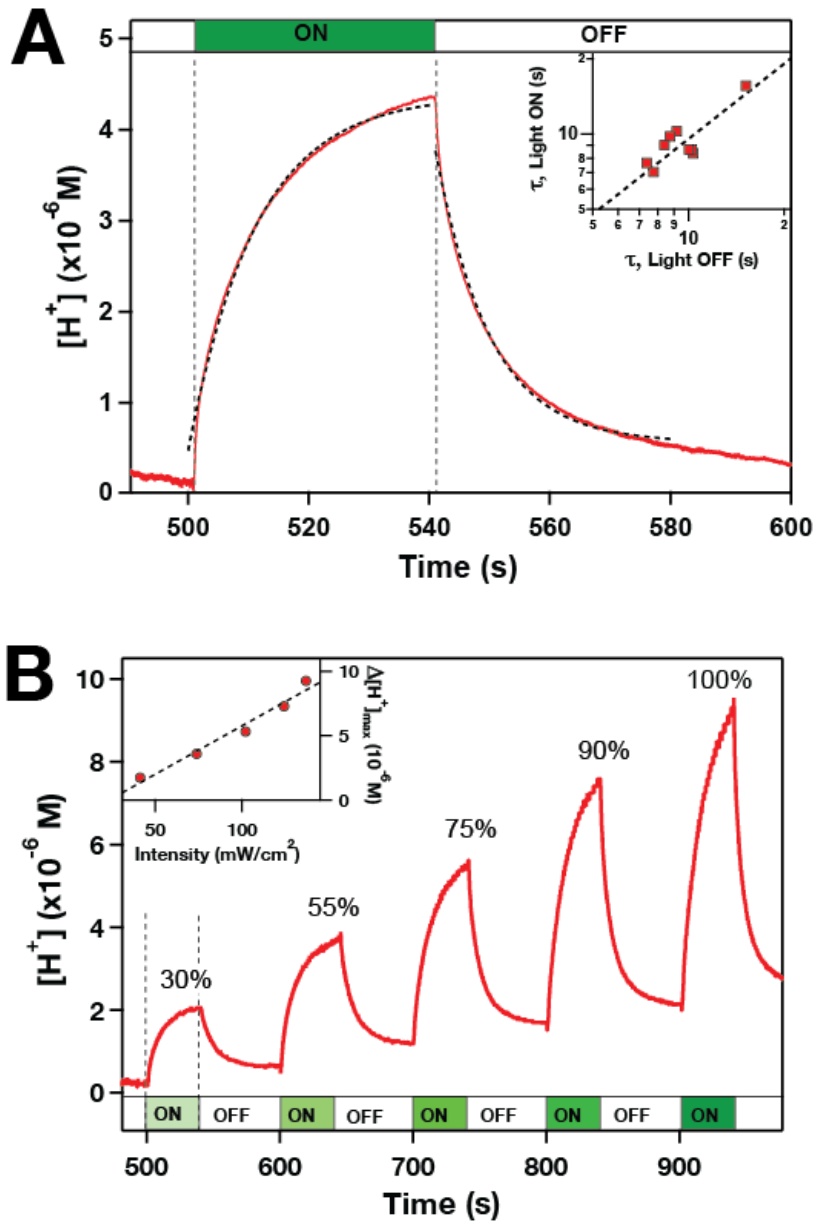

Figure 4.21 Kinetics of the device response

A. Time trace of the proton concentration under the lipid bilayer in the vincinity of the SiNW over one light ON/light OFF cycle for the device incorporating bR proteins (each cycle consisted of 40s light exposure followed by 60s of dark time). Dashed lines represent the best fit to Eq. 2 and 3. Inset: A log-log plot of the proton leakage time values obtained from the fits.

B. Time trace of the proton concentration next to the SiNW surface in another device under illumination cycles of different intensity. Inset: A plot of the maximum proton accumulation as a function of incident light intensity.

4.4.1.4 Biological modulation of the device operational characteristics

The dynamic equilibrium between the pumping and leakage processes that defines the device performance also gives us an opportunity to vary the two key operational parameters—the protein pumping and the proton leakage rates. Previous studies of bR in cellular environments[101-103] found that proton-electrochemical gradient, $\Delta\mu_H^+$, across the membrane can influence bR's pumping efficiency[101]. Thus we can modify the device performance using different ionophore molecules that allow specific ions to cross the lipid membrane. Three different ionophores that self-insert into the bilayer allowed us to vary different components of the proton-electrochemical gradient independently. Valinomycin, a hydrophobic carrier molecule that shuttles K^+ ions across the membrane in the direction of the electrochemical gradient [104, 105], relieves the electric field gradient across the membrane, but leaves the proton gradient intact. Nigericin, a transmembrane carrier that catalyzes an electro-neutral K^+/H^+ exchange across the lipid bilayer [106, 107], relieves the proton gradient, but preserves the electric field gradient. Finally, gramicidin A (gramA), a peptide that forms a passive channel in the membrane allowing fast ion leakage[108], neutralizes both of these gradients.

Valinomycin, which allows only K^+ ions to cross the membrane, provides an effective compensatory pathway to relieve the electrical potential across the bilayer while keeping the proton gradient intact. Since this activity relieves the back-pressure caused by the electrochemical gradient, on the proton pump, we expect that bR protein should be able to develop a larger pH gradient under the bilayer in presence of valinomycin. Indeed, addition of 2 μM of valinomycin to the 1D bilayer device increased the peak proton accumulation under the bilayer surface by ~50% (decreasing the pH by additional 0.3 units) compared to devices containing only bR (Fig. 4.22a). This effect was also repeatable over multiple light on/off cycles. The initial pumping rate also increased almost 2-fold compared to devices containing bR only (Fig. 4.23a). The origin of this effect is best understood by considering that the maximum proton gradient that can be generated in the device is given by the value of the proton concentration when the proton flux generated by the pump is equal to the proton flux leaking through the bilayer:

$$\Delta C_{max} = I_0 \tau \qquad (4)$$

According to Eq. 4, increased protein pumping rate should lead to the enhanced device response. Another confirmation of this mechanism comes from the values for the proton leakage rate time constant: as we expected, valinomycin addition did not significantly change the proton leakage rate (Fig. 4.23c).

Incorporation of nigericin, an electro-neutral antiporter ionophore, exploits a different aspect of our device functionality. Nigericin facilitates the back-flux of the protons pumped under the bilayer by bR, thus providing some relief for the proton gradient. Since this action is accompanied by the coupled flux of potassium ions in the opposite direction, this ionophore preserves the electrical field gradient developed by bacteriorhodopsin. By providing an extra leakage pathway for the protons, nigericin effectively reduces the efficiency of the proton pumping; therefore, according to Eq. 4, the maximum signal achieved by the device should also be reduced relative to the signal obtained before introduction of the ionophore. Indeed, the experiment shows (Fig. 4.22b) that after addition of 2 μM nigericin the maximum proton accumulation decreased by ca.

35% (a ΔpH difference of 0.2 units) compared to the devices with only the bR protein. In this instance, we see that the initial pumping rate decreased approximately 2-fold at the maximum light intensity (Fig. 4.23b). Additionally, since nigericin provides another leakage pathway for protons, we saw faster leakage time, τ, during the light-ON state (Fig. 4.23c). Curiously the average leakage time during the light-OFF state remained largely unchanged; further investigations should help to clarify the origins of this effect.

Finally, we explored a way to drastically increase the proton leakage rate though the lipid bilayer by introducing gramA to our devices. GramA is a passive pore that exhibits high permeability for protons and monovalent ions. The presence of GramA pores in the bilayer-coated device effectively shorts the lipid membrane and provides a major pathway to relieve all ion and proton gradients in the system [109, 110]. Indeed, when we introduced GramA to our devices, most of the proton pump activity was suppressed and we observed only very small SiNW conductance change in response to the green light illumination (Fig. 4.22c). In this work, we used hierarchical assembly of membrane protein pumps and ionophore molecules to create biologically-tunable bioelectronic devices that converted light-induced proton transport by bacteriorhodopsin protein into an electronic signal. The results show that addition of ionophores to the system can tune the device output by altering the two dominant kinetic processes in the system: proton pumping by the bR protein, and passive proton leakage through the lipid bilayer. Furthermore, different ionophores were able to modulate different system parameters. Valinomycin enhanced the initial device response rate, and increased the overall level of device response. Nigericin, in contrast, reduced the overall device response and the initial device response rate. Co-reconstitution of gramA into the lipid membrane abolished the device response and effectively neutralized the pH gradient buildup by perforating the lipid bilayer.

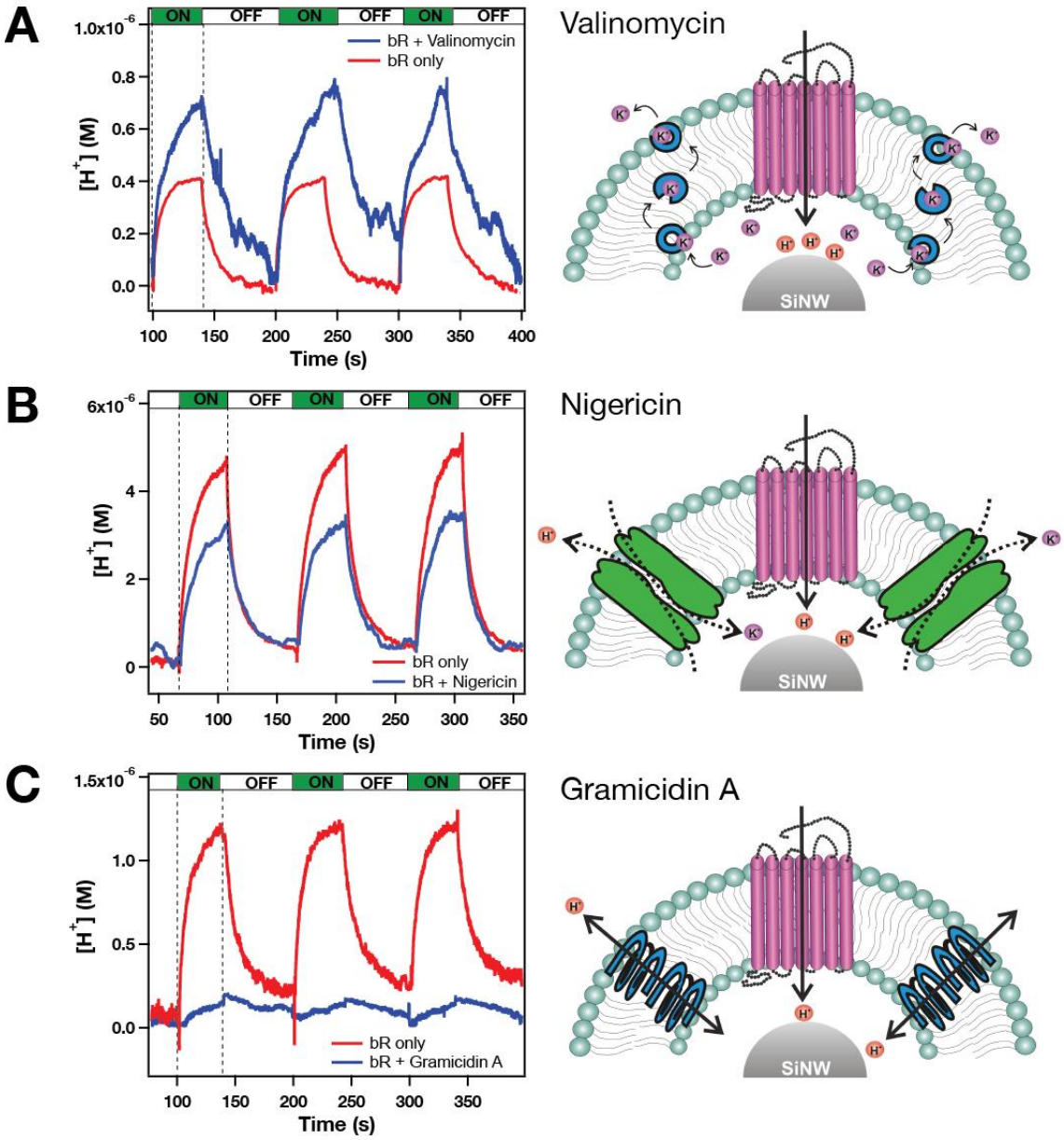

Figure 4.22 Device response in presence of ionophores

Time traces of the proton concentration under lipid bilayer in the vincinity of the SiNW for the devices incorporating bR proteins and (**A**) valinomycin, (**B**) nigericin, and (**C**) gramicidin A. Schematics on the right side illustrate the action mechanism for each ionophore.

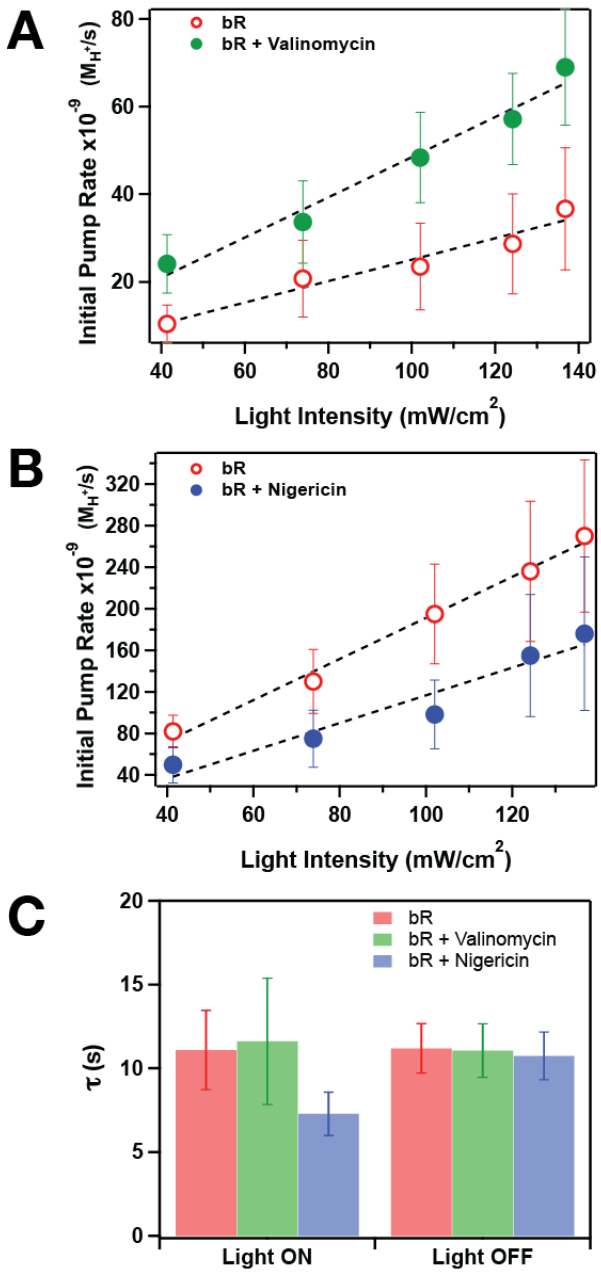

Figure 4.23 Bioelectronic device performance in presence of ionophores

(**A**). A plot comparing the initial bR pumping rate measured in the device incorporating bR protein before (empty red circles), and after (filled green circles) addition of 2 µM valinomycin. (**B**), A plot comparing the initial bR pump rates for bR containing devices before (empty red circles) and after (blue filled circles) exposure to 2 µM nigericin. (**C**). Bar graph showing the values for the average proton leakage time through the lipid bilayer measured with the light ON and light OFF for devices containing bR only (red), bR and valinomycin (green), and bR and nigericin (blue).

4.5 Conclusion

P-doped silicon nanowires were synthesized by catalytic CVD method and this SiNW based field effect transistors (FET) for bioelectronics were fabricated using conventional photolithography to pattern metal electrodes passivated with silicon nitride or photoresist layer. Template-directed assembly of 1D lipid bilayers on the nanowire templates showed these lipid bilayers covering nanowires were continuous and mobile.

bR acts as a biological gate that allows the device to convert protein photocycle events into a transistor response. Co-assembly of several different ionophores in the device allowed us to regulate two key parameters that determine the device functionality: the proton accumulation and proton gradient relief rates. These results demonstrate that biological regulation mechanisms can be used to tune bioelectronic device performance. These results open up new opportunities for constructing bioelectronic devices. The incorporation of a robust proton pump capable of developing significant pH gradients is a major step towards integration of other biological processes powered by proton gradients to nanoelectronic circuits. Most significantly, the possibility to tune the device performance by using biological modifiers co-assembled in the membrane covering the nanowire gives researchers a much more extensive biological toolkit for bioelectronics applications.

Bibliography

[1] Aidley DJ, Stanfield PR. Ion Channels: Molecules in Action: Cambridge University Press; 1996.
[2] Groves J. Supported Lipid Bilayers as Mimics for Cell Surfaces and as Tools in Biotechnology. [Book] BioMEMS and Biomedical Nanotechnology. 2007;3:305-23.
[3] Langecker M, Arnaut V, Martin TG, List J, Renner S, Mayer M, et al. Synthetic Lipid Membrane Channels Formed by Designed DNA Nanostructures. Science. 2012;338:932-6.
[4] Siria A, Poncharal P, Biance AL, Fulcrand R, Blase X, Purcell ST, et al. Giant osmotic energy conversion measured in a single transmembrane boron nitride nanotube. Nature. 2013;494:455-8.
[5] Hall AR, Scott A, Rotem D, Mehta KK, Bayley H, Dekker C. Hybrid pore formation by directed insertion of alpha-haemolysin into solid-state nanopores. Nat Nanotechnol. 2010;5:874-7.
[6] Lee CY, Choi W, Han JH, Strano MS. Coherence Resonance in a Single-Walled Carbon Nanotube Ion Channel. Science. 2010;329:1320-4.
[7] Liu HT, He J, Tang JY, Liu H, Pang P, Cao D, et al. Translocation of Single-Stranded DNA Through Single-Walled Carbon Nanotubes. Science. 2010;327:64-7.
[8] Kalra A, Garde S, Hummer G. Osmotic water transport through carbon nanotube membranes. Proceedings of the National Academy of Sciences2003. p. 10175-80.
[9] Holt JK, Park HG, Wang YM, Stadermann M, Artyukhin AB, Grigoropoulos CP, et al. Fast mass transport through sub-2-nanometer carbon nanotubes. Science. 2006;312:1034-7.
[10] Lopez CF, Nielsen SO, Moore PB, Klein ML. Understanding nature's design for a nanosyringe. P Natl Acad Sci USA. 2004;101:4431-4.
[11] Artyukhin AB, Shestakov A, Harper J, Bakajin O, Stroeve P, Noy A. Functional one-dimensional lipid bilayers on carbon nanotube templates. J Am Chem Soc. 2005;127:7538-42.
[12] Noy A. Bionanoelectronics. Adv Mater: WILEY-VCH Verlag; 2011. p. 807-20.
[13] Misra N, Martinez JA, Huang SCJ, Wang YM, Stroeve P, Grigoropoulos CP, et al. Bioelectronic silicon nanowire devices using functional membrane proteins. P Natl Acad Sci USA. 2009;106:13780-4.
[14] Martinez JA, Misra N, Wang YM, Stroeve P, Grigoropoulos CP, Noy A. Highly Efficient Biocompatible Single Silicon Nanowire Electrodes with Functional Biological Pore Channels. Nano Letters. 2009;9:1121-6.
[15] Huang SCJ, Artyukhin AB, Misra N, Martinez JA, Stroeve PA, Grigoropoulos CP, et al. Carbon Nanotube Transistor Controlled by a Biological Ion Pump Gate. Nano Letters. 2010;10:1812-6.
[16] Huang SCJ, Artyukhin AB, Martinez JA, Sirbuly DJ, Wang Y, Ju JW, et al. Formation, stability, and mobility of one-dimensional lipid Bilayers on polysilicon nanowires. Nano Letters. 2007;7:3355-9.
[17] Doyle DA, Cabral JM, Pfuetzner RA, Kuo AL, Gulbis JM, Cohen SL, et al. The structure of the potassium channel: Molecular basis of K+ conduction and selectivity. Science. 1998;280:69-77.

[18] Dutzler R, Campbell EB, Cadene M, Chait BT, MacKinnon R. X-ray structure of a CIC chloride channel at 3.0 angstrom reveals the molecular basis of anion selectivity. Nature. 2002;415:287-94.
[19] Dutzler R, Campbell EB, MacKinnon R. Gating the selectivity filter in ClC chloride channels. Science. 2003;300:108-12.
[20] Sui H, Han B-G, Lee JK, Walian P, Jap BK. Structural basis of water-specific transport through the AQP1 water channel. Nature. 2001;414:872-8.
[21] Zhou Y, Morais-Cabral JH, Kaufman A, MacKinnon R. Chemistry of ion coordination and hydration revealed by a K+ channel-Fab complex at 2.0 A resolution. Nature. 2001;414:43-8.
[22] Hummer G. Water, proton, and ion transport: from nanotubes to proteins. Mol Phys. 2007;105:201 - 7.
[23] Holt JK, Park HG, Wang Y, Stadermann M, Artyukhin AB, Grigoropoulos CP, et al. Fast Mass Transport Through Sub-2-Nanometer Carbon Nanotubes. Science. 2006;312:1034-7.
[24] Hinds BJ, Chopra N, Rantell T, Andrews R, Gavalas V, Bachas LG. Aligned multiwalled carbon nanotube membranes. Science. 2004;303:62-5.
[25] Liu H, He J, Tang J, Liu H, Pang P, Cao D, et al. Translocation of Single-Stranded DNA Through Single-Walled Carbon Nanotubes. Science. 2010;327:64-7.
[26] Lee CY, Choi W, Han J-H, Strano MS. Coherence Resonance in a Single-Walled Carbon Nanotube Ion Channel. Science. 2010;329:1320-4.
[27] Majumder M, Chopra N, Andrews R, Hinds BJ. Nanoscale hydrodynamics: Enhanced flow in carbon nanotubes. Nature. 2005;438:44-.
[28] Lopez CF, Nielsen SO, Moore PB, Klein ML. Understanding nature's design for a nanosyringe. Proc Natl Acad Sci USA. 2004;101:4431-4.
[29] Zimmerli U, Koumoutsakos P. Simulations of Electrophoretic RNA Transport Through Transmembrane Carbon Nanotubes. Biophys J. 2008;94:2546-57.
[30] Jia ZJ, Wang ZY, Liang J, Wei BQ, Wu DH. Production of short multi-walled carbon nanotubes. Carbon. 1999;37:903-6.
[31] Smalley RE, Liu J, Rinzler AG, Dai HJ, Hafner JH, Bradley RK, et al. Fullerene pipes. Science. 1998;280:1253-6.
[32] Vazquez E, Rubio N, Fabbro C, Herrero MA, de la Hoz A, Meneghetti M, et al. Ball-Milling Modification of Single-Walled Carbon Nanotubes: Purification, Cutting, and Functionalization. Small. 2011;7:665-74.
[33] Krause B, Villmow T, Boldt R, Mende M, Petzold G, Poetschke P. Influence of dry grinding in a ball mill on the length of multiwalled carbon nanotubes and their dispersion and percolation behaviour in melt mixed polycarbonate composites. Compos Sci Technol. 2011;71:1145-53.
[34] Fonseca A, Reijerkerk S, Potreck J, Nijmeijer K, Mekhalif Z, Delhalle J. Very short functionalized carbon nanotubes for membrane applications. Desalination. 2010;250:1150-4.
[35] Pierard N, Fonseca A, Colomer JF, Bossuot C, Benoit JM, Van Tendeloo G, et al. Ball milling effect on the structure of single-wall carbon nanotubes. Carbon. 2004;42:1691-7.

[36] Liu F, Zhang XB, Cheng JP, Tu JP, Kong FZ, Huang WZ, et al. Preparation of short carbon nanotubes by mechanical ball milling and their hydrogen adsorption behavior. Carbon. 2003;41:2527-32.
[37] Konya Z, Vesselenyi I, Niesz K, Kukovecz A, Demortier A, Fonseca A, et al. Large scale production of short functionalized carbon nanotubes. Chem Phys Lett. 2002;360:429-35.
[38] Pierard N, Fonseca A, Konya Z, Willems I, Van Tendeloo G, Nagy JB. Production of short carbon nanotubes with open tips by ball milling. Chem Phys Lett. 2001;335:1-8.
[39] Bernier P, Stepanek I, Maurin G, Gavillet J, Loiseau A, Edwards R, et al. Nano-mechanical cutting and opening of single wall carbon nanotubes. Chem Phys Lett. 2000;331:125-31.
[40] Liu P, Wang TM. Ultrasonic-assisted chemical oxidative cutting of multiwalled carbon nanotubes with ammonium persulfate in neutral media. Appl Phys a-Mater. 2009;97:771-5.
[41] Dai H, Sun X, Zaric S, Daranciang D, Welsher K, Lu Y, et al. Optical properties of ultrashort semiconducting single-walled carbon nanotube capsules down to sub-10 nm. J Am Chem Soc. 2008;130:6551-5.
[42] Walker ARH, Fagan JA, Simpson JR, Bauer BJ, Lacerda SHD, Becker ML, et al. Length-dependent optical effects in single-wall carbon nanotubes. J Am Chem Soc. 2007;129:10607-12.
[43] Stevens JL, Huang AY, Peng HQ, Chiang LW, Khabashesku VN, Margrave JL. Sidewall amino-functionalization of single-walled carbon nanotubes through fluorination and subsequent reactions with terminal diamines. Nano Letters. 2003;3:331-6.
[44] Gu Z, Peng H, Hauge RH, Smalley RE, Margrave JL. Cutting single-wall carbon nanotubes through fluorination. Nano Letters. 2002;2:1009-13.
[45] Lustig SR, Boyes ED, French RH, Gierke TD, Harmer MA, Hietpas PB, et al. Lithographically cut single-walled carbon nanotubes: Controlling length distribution and introducing end-group functionality. Nano Letters. 2003;3:1007-12.
[46] Wang S, Liang Z, Wang B, Zhang C, Rahman Z. Precise cutting of single-walled carbon nanotubes. Nanotechnology. 2007;18.
[47] Sun X, Zaric S, Daranciang D, Welsher K, Lu Y, Li X, et al. Optical Properties of Ultrashort Semiconducting Single-Walled Carbon Nanotube Capsules Down to Sub-10 nm. J Am Chem Soc. 2008;130:6551-5.
[48] Richard C, Balavoine F, Schultz P, Ebbesen TW, Mioskowski C. Supramolecular self-assembly of lipid derivatives on carbon nanotubes. Science. 2003;300:775-8.
[49] Dresselhaus MS, Dresselhaus G, Saito R, Jorio A. Raman spectroscopy of carbon nanotubes. Phys Rep. 2005;409:47-99.
[50] Murata K, Mitsuoka K, Hirai T, Walz T, Agre P, Heymann JB, et al. Structural determinants of water permeation through aquaporin-1. Nature. 2000;407:599-605.
[51] Doyle DA, Cabral JM, Pfuetzner RA, Kuo A, Gulbis JM, Cohen SL, et al. The structure of the potassium channel: molecular basis of K+ conduction and selectivity. Science. 1998;280:69-77.
[52] Israelachvili J. *Intermolecular and Surface Forces*. New York: Academic Press; 1992.
[53] Morth JP, Pedersen BP, Toustrup-Jensen MS, Sorensen TLM, Petersen J, Andersen JP, et al. Crystal structure of the sodium-potassium pump. Nature. 2007;450:1043-9.

[54] Gu LQ, Braha O, Conlan S, Cheley S, Bayley H. Stochastic sensing of organic analytes by a pore-forming protein containing a molecular adapter. Nature. 1999;398:686-90.
[55] Murray C, Shabany H, Gokel G. The central relay unit in hydraphile channels as a model for the water-and-ion capsuleof channel proteins. Chemical Communications (Cambridge, United Kingdom). 2000;2000:2371-2.
[56] Matile S, Som A, Sorde N. Recent synthetic ion channels and pores. Tetrahedron. 2004;60:6405-35.
[57] Li J, Stein D, McMullan C, Branton D, Aziz MJ, Golovchenko JA. Ion-beam sculpting at nanometre length scales. Nature. 2001;412:166-9.
[58] Hall AR, Scott A, Rotem D, Mehta KK, Bayley H, Dekker C. Hybrid pore formation by directed insertion of [alpha]-haemolysin into solid-state nanopores. Nat Nanotechnol. 2010;5:874-7.
[59] Hurtley SM, Helenius A. Protein oligomerization in the endoplasmic reticulum. Annual review of cell biology. 1989;5:277-307.
[60] Sabın J, Prieto G, Ruso JM, Hidalgo-Álvarez R, Sarmiento F. Size and stability of liposomes: A possible role of hydration and osmotic forces. The European Physical Journal E2006. p. 401-8.
[61] Fornasiero F, Park HG, Holt JK, Stadermann M, Grigoropoulos CP, Noy A, et al. Ion exclusion by sub-2-nm carbon nanotube pores. Proceedings of the National Academy of Sciences: National Acad Sciences; 2008. p. 17250-5.
[62] Zambrano HA, Walther JH, Koumoutsakos P, Sbalzarini IF. Thermophoretic Motion of Water Nanodroplets Confined inside Carbon Nanotubes. Nano Letters: American Chemical Society; 2008. p. 66-71.
[63] Naguib N, Ye H, Gogotsi Y, Yazicioglu AG, Megaridis CM, Yoshimura M. Observation of Water Confined in Nanometer Channels of Closed Carbon Nanotubes. Nano Letters: American Chemical Society; 2004. p. 2237-43.
[64] Zhao Y, Song L, Deng K, Liu Z, Zhang Z, Yang Y, et al. Individual Water-Filled Single-Walled Carbon Nanotubes as Hydroelectric Power Converters. Adv Mater: WILEY-VCH Verlag; 2008. p. 1772-6.
[65] Wu J, Gerstandt K, Zhang H, Liu J, Hinds BJ. Electrophoretically induced aqueous flow through single-walled carbon nanotube membranes. Nat Nanotechnol: Nature Publishing Group; 2012. p. 133-9.
[66] Qin X, Yuan Q, Zhao Y, Xie S, Liu Z. Measurement of the Rate of Water Translocation through Carbon Nanotubes. Nano Letters: American Chemical Society; 2011. p. 2173-7.
[67] Paineau E, Albouy P-A, Rouzière S, Orecchini A, Rols S, Launois P. X-ray Scattering Determination of the Structure of Water during Carbon Nanotube Filling. Nano Letters2013. p. 1751-6.
[68] Kim K, Geng J, Zhang J, Noy A, Ajo-Franklin CM, Grigoropoulos CP, et al. Stochastic Transport and Gating in Carbon Nanotube Porins in Lipid Membranes. Manuscript in submission; 2013.
[69] Fornasiero F, Park H-G, Holt JK, Stadermann M, Grigoropoulos C, Noy A, et al. Ion Exclusion by sub 2-nm Carbon Nanotube Pores. Proc Natl Acad Sci USA. 2008;105:17250-5.

[70] Granath KA. Solution properties of branched dextrans. Journal of Colloid Science1958. p. 308-28.
[71] Walstra P. Food Science and Technology: CRC Press; 2002.
[72] Perkin S, Goldberg R, Chai L, Kampf N, Klein J. Dynamic properties of confined hydration layers. Faraday Discussions2008. p. 399.
[73] Walther JH, Ritos K, Cruz-Chu ER, Megaridis CM, Koumoutsakos P. Barriers to Superfast Water Transport in Carbon Nanotube Membranes. Nano Lett. 2013;13:1910-4.
[74] Braha O, Walker B, Cheley S, Kasianowicz JJ, Song L, Gouaux JE, et al. Designed protein pores as components for biosensors. Chem Biol. 1997;4:497-505.
[75] Song L, Hobaugh MR, Shustak C, Cheley S, Bayley H, Gouaux JE. Structure of staphylococcal α-hemolysin, a heptameric transmembrane pore. science. 1996;274:1859-65.
[76] Powell MR, Sullivan M, Vlassiouk I, Constantin D, Sudre O, Martens CC, et al. Nanoprecipitation-assisted ion current oscillations. Nat Nanotechnol. 2007;3:51-7.
[77] Powell MR, Cleary L, Davenport M, Shea KJ, Siwy ZS. Electric-field-induced wetting and dewetting in single hydrophobic nanopores. Nat Nanotechnol. 2011;6:798-802.
[78] Hummer G, Rasaiah JC, Noworyta JP. Water conduction through the hydrophobic channel of a carbon nanotube. Nature. 2001;414:188-90.
[79] Colquhoun D, Hawkes A. The Principles of the Stochastic Interpretation of Ion-Channel Mechanisms. In: Sakmann B, Neher E, editors. Single-Channel Recording: Springer US; 1995. p. 397-482.
[80] Buyukdagli S, Manghi M, Palmeri J. Ionic Capillary Evaporation in Weakly Charged Nanopores. Phys Rev Lett. 2010;105:158103.
[81] Shimizu S, Ellison M, Aziz K, Wang QH, Ulissi Z, Gunther Z, et al. Stochastic Pore Blocking and Gating in PDMS–Glass Nanopores from Vapor–Liquid Phase Transitions. The Journal of Physical Chemistry C. 2013;117:9641-51.
[82] Kasianowicz JJ, Brandin E, Branton D, Deamer DW. Characterization of individual polynucleotide molecules using a membrane channel. Proc Natl Acad Sci USA. 1996;93:13770-3.
[83] Alberts B, Bray D, Lewis J, Raff M, Roberts K, Watson JD. Molecular Biology of the Cell. 5 ed. New York: Garland Science; 2007.
[84] Noy A. Bionanoelectronics. Adv Mater (Weinheim, Ger). 2011;23:799-.
[85] He B, Morrow TJ, Keating CD. Nanowire sensors for multiplexed detection of biomolecules. Curr Opin Chem Biol. 2008;12:522-8.
[86] Gao A, Lu N, Wang Y, Dai P, Li T, Gao X, et al. Enhanced Sensing of Nucleic Acids with Silicon Nanowire Field Effect Transistor Biosensors. Nano Letters. 2012;12:5262-8.
[87] Lin S-P, Pan C-Y, Tseng K-C, Lin M-C, Chen C-D, Tsai C-C, et al. A reversible surface functionalized nanowire transistor to study protein–protein interactions. Nano Today. 2009;4:235-43.
[88] Duan X, Li Y, Rajan NK, Routenberg DA, Modis Y, Reed MA. Quantification of the affinities and kinetics of protein interactions using silicon nanowire biosensors. Nat Nano. 2012;7:401-7.

[89] Patolsky F, Timko BP, Yu G, Fang Y, Greytak AB, Zheng G, et al. Detection, Stimulation, and Inhibition of Neuronal Signals with High-Density Nanowire Transistor Arrays. Science. 2006;313:1100-4.
[90] Bozhi Tian, Jia Liu, Tal Dvir, Lihua Jin, Jonathan H. Tsui, Quan Qing, et al. Macroporous nanowire nanoelectronic scaffolds for synthetic tissues. Nat Mater. 2012;11:986–94.
[91] Misra N, Martinez JA, Huang S-C, Wang Y, Stroeve P, Grigoropoulos C, et al. Bioelectronic Silicon Nanowire Devices Utilizing Functional Membrane Proteins. Proc Natl Acad Sci USA. 2009;106:13780–4
[92] Huang S-C, Artyukhin A, Misra N, Martinez J, Stroeve P, Grigoropoulos C, et al. Carbon nanotube devices controlled by an ion pump. Nano Lett. 2010;10:1812–6.
[93] Cui Y, Wei QQ, Park HK, Lieber CM. Nanowire nanosensors for highly sensitive and selective detection of biological and chemical species. Science. 2001;293:1289-92.
[94] Huang Y, Duan X, Wei Q, Lieber CM. Directed Assembly of One-Dimensional Nanostructures into Functional Networks. Science. 2001;291:630-3.
[95] Royant A, Edman K, Ursby T, Pebay-Peyroula E, Landau EM, Neutze R. Helix deformation is coupled to vectorial proton transport in the photocycle of bacteriorhodopsin. Nature. 2000;406:645-8.
[96] Lozier RH, Bogomolni RA, Stoeckenius W. Bacteriorhodopsin: a light-driven proton pump in Halobacterium Halobium. Biophys J. 1975;15:955–62.
[97] Thavasi V, Lazarova T, Filipek S, Kolinski M, Querol E, Kumar A, et al. Study on the Feasibility of Bacteriorhodopsin as Bio-Photosensitizer in Excitonic Solar Cell: A First Report. Journal of Nanoscience and Nanotechnology. 2009;9:1679-87.
[98] Quan R, Ya-Pu Z, Li H, Hui-Bin Z. A nanomechanical device based on light-driven proton pumps. Nanotechnology. 2006;17:1778.
[99] Kim K-HK, Kihyun; Jeong, Dong-Young; Min, Byungdon; Cho, Kyoungah; Kim, Hyunsuk; Moon, Byung-Moo; Noh, Taeyong; Park, Jucheol; Suh, Minchul; Kim, Sangsig Photocurrent of Undoped, n- and p-Type Si Nanowires Synthesized by Thermal Chemical Vapor Deposition. Jpn J Appl Phys. 2006;45:4265-9.
[100] Cui Y, Wei Q, Park H, Lieber CM. Nanowire Nanosensors for Highly Sensitive and Selective Detection of Biological and Chemical Species. Science. 2001;293:1289-92.
[101] Joshi MK, Bose S, Hendler RW. Regulation of the Bacteriorhodopsin Photocycle and Proton Pumping in Whole Cells of Halobacterium salinarium. Biochemistry. 1999;38:8786-93.
[102] Sherman WV, Caplan SR. Arrhenius parameters of phototransients in Halobacterium halobium in physiological conditions. Nature. 1975;258:766-8.
[103] S L Helgerson MKM, D B Bivin, P K Wolber, E Heinz, and W Stoeckenius. Coupling between the bacteriorhodopsin photocycle and the protonmotive force in Halobacterium halobium cell envelope vesicles. III. Time-resolved increase in the transmembrane electric potential and modeling of the associated ion fluxes. Biophys J. 1985 48:709–19.
[104] Garlid KD, Paucek P. Mitochondrial potassium transport: the K+ cycle. Biochimica et Biophysica Acta (BBA) - Bioenergetics. 2003;1606:23-41.
[105] Johnson SM, Bangham AD. Potassium permeability of single compartment liposomes with and without valinomycin. Biochimica et Biophysica Acta (BBA) - Biomembranes. 1969;193:82-91.

[106] Rigaud JL, Bluzat A, Buschlen S. Incorporation of bacteriorhodopsin into large unilamellar liposomes by reverse phase evaporation. Biochem Bioph Res Co. 1983;111:373-82.
[107] Hellingwerf KJ, Arents JC, Scholte BJ, Westerhoff HV. Bacteriorhodopsin in liposomes. II. Experimental evidence in support of a theoretical model. Biochimica et Biophysica Acta (BBA) - Bioenergetics. 1979;547:561-82.
[108] Kelkar DA, Chattopadhyay A. The gramicidin ion channel: A model membrane protein. Biochimica et Biophysica Acta (BBA) - Biomembranes. 2007;1768:2011-25.
[109] Clement NR, Gould JM. Kinetics for the development of gramicidin-induced ion permeability in unilamellar phospholipid vesicles. Biochemistry. 1981;20:1544-8.
[110] Prabhananda BS, Kombrabail MH. Two mechanisms of H+/OH- transport across phospholipid vesicular membrane facilitated by gramicidin A. Biophysical Journal. 1996;71:3091-7.